THESIS

TOWARDS AUTOMATED MANUFACTURING OF COMPOSITES VIA THERMALLY ASSISTED FRONTAL POLYMERIZATION

Submitted by

Walter Patrick Jordan

Department of Mechanical Engineering

In partial fulfillment of the requirements

For the Degree of Master of Science

Colorado State University

Fort Collins, Colorado

Summer 2024

Master's Committee:

Advisor: Mostafa Yourdkhani

Jianguo Zhao
Steve Simske

ABSTRACT

TOWARDS AUTOMATED MANUFACTURING OF COMPOSITES VIA THERMALLY ASSISTED FRONTAL POLYMERIZATION

Current methods for the manufacturing and repair of fiber-reinforced thermoset composites are energy-intensive, slow, and costly due to extensive processing steps and expensive equipment required to achieve complete cure. This is especially true for large, complex geometries that require autoclaves and prolonged cure times. As a result, there is a need to develop faster, cost-effective, energy-efficient processes. With the implementation of rapid curing thermoset resins, the cure cycle can be reduced from hours to minutes. This research focuses on the development, implementation, and testing of these resin systems in the established fields of mobile additive manufacturing and filament winding to demonstrate unprecedented, rapid manufacturing of composite parts.

Additive manufacturing of fiber-reinforced thermoset composites is desirable due to its inherent ability to produce custom, complex parts quickly, with minimal required tooling. By printing and simultaneously curing the composite as it is deposited, freeform unsupported structures with high mechanical properties can be created. One limitation of current additive manufacturing methods is the print volume associated with traditional gantry style additive manufacturing systems. By combining the highly desirable properties of additive manufacturing using rapid, thermally curable resin systems with the mobility of a mobile additive manufacturing system, large, mechanically sound structures with virtually no limitations on print volume can be created. Moreover, rapid curing thermoset resin systems have the potential to revolutionize traditional composite manufacturing processes. Due to its wide range of applications and its ubiquitous nature, filament winding serves as a natural starting point to do so. Traditional filament winding is typically a two-step manufacturing process, where the composite part is first wound on a rotating mandrel and then cured using autoclaves or ovens. By combining these processes on the winding machine, the labor involved in manufacturing, the energy required for curing, and the overall production time are significantly reduced.

In this research, a mobile additive manufacturing robot is designed, validated, and optimized for accurate locomotion and fast, dimensionally accurate printing of composite structures with high fiber alignment and degree of cure. The capabilities of this system are exhibited throughout several demonstrations that involve printing unsupported structures upside-down, the manufacturing of a bridge strong enough for the robot to pass over, and bridging the material across a 60 cm gap. Additionally, a pre-existing filament winding machine is optimized for the manufacturing of large, geometrically unconstrained composite structures. Improvements in fiber volume fraction are achieved through processing changes and a thermal profile for dry fibers is established to facilitate identification of frontal polymerization.

ACKNOWLEDGMENTS

I am immensely grateful to my advisor Dr. Mostafa Yourdkhani and my co-advisor Dr. Jianguo Zhao, for their unwavering guidance, encouragement, and support. Through both technical expertise and creativity, their mentorship has been invaluable in navigating the highs and lows of my research journey. Together, they have contributed to my development both as a researcher and as a person.

I would like to express my appreciation to my colleagues from the Multifunctional Polymers and Composites Lab and the Adaptive Robotics Lab. A special thanks to Carter Dojan for his scientific insights and assistance with experimentation, as well as to Eli Lerner for his assistance with programming and robotics. I would especially like to express my gratitude towards Samuel Radosevich, Clint Middlemist, and Bryce Jones for the camaraderie and collaboration throughout the course of each of our respective research efforts.

Finally, I would like to extend my heartfelt gratitude to my wonderful family for their encouragement, love, and support throughout. A special thank you to my dad for his continual encouragement to follow my dreams and to my mom for her unwavering support and indispensable advice along the way.

TABLE OF CONTENTS

LIST OF TABLES

LIST OF FIGURES

Chapter 1. INTRODUCTION AND BACKGROUND

1.1 Project Outline

The following thesis focuses on research performed on two separate projects. Both projects involve the application of thermally curable thermoset resin to previously established manufacturing processes. The first process outlined in chapter 1 is mobile additive manufacturing (MAM). The second process outlined in chapter 2 is filament winding (FW). While the fields themselves are not new, the novelty lies in the application of this new resin system to these fields as discussed in this chapter.

1.2 Introduction to Composites and Related Manufacturing Processes

1.2.1 Composite Materials

A fiber-reinforced composite material is an anisotropic and inhomogeneous combination of two or more physically distinct constituent materials. These constituent materials typically consist of a matrix material and at least one reinforcement material. Matrix materials bind the reinforcement material(s) together, help to distribute loads, and provide structure to capture the geometry of the desired part. A wide variety of matrix materials can be used depending on the application; Table 1-1 shows the most commonly used matrix materials and their associated applications.

Table 1-1: Frequently used matrix materials and their applications [1]

Matrix Material	**Applications**
Thermoplastic Polymers	Applications that require high impact strength and fatigue resistance, unlimited shelf life, and postformability.
Thermoset Polymers	Applications requiring low viscosity matrix during manufacturing, high thermal stability, high chemical resistance, low creep, and low stress relaxation.
Metals	Applications requiring long term resistance to severe environments and high temperature.

Ceramics	Applications requiring high temperature stability, high thermal shock resistance, high hardness, high corrosion resistance, and low density.
Carbon	Applications requiring low density, high modulus and strength, low coefficient of thermal expansion, and high thermal shock resistance.

The focus of this research is on thermoset-matrix composites. In a thermoset polymer, precursors are joined by cross-links, forming a rigid, three-dimensional structure that cannot be reformed by heating [1]. Prior to crosslinking, thermoset polymeric materials typically exhibit a low viscosity, which enhances processability by facilitating fiber wet-out and increasing interaction between the reinforcement and matrix [1].

By contrast, reinforcement materials typically carry loads within a composite structure and are usually stronger, lighter, and stiffer than the matrix material. Depending on the design intent, different reinforcement materials can be used to optimize material functionality. Table 1-2 summarizes the most commonly used reinforcement materials that can be seen in polymer-matrix composites.

Table 1-2: Frequently used reinforcement materials in polymer-matrix composites and their applications[1].

Reinforcement Material	Applications
Carbon Fiber	Applications that require exceptional tensile-strength-weight ratios, low coefficient of thermal expansion, high fatigue strengths, and high thermal conductivity.
Glass Fiber	Applications requiring low expense, high tensile strength, high chemical resistance, and excellent insulating properties.
Aramid Fiber	Applications requiring low density, high tensile strength-to-weight ratio, and high impact resistance.
Natural Fiber	Applications requiring environmentally friendly material, low density, and acoustic damping.

The focus of this research is on carbon fiber-reinforcement materials. Carbon fibers typically offer the highest mechanical properties and are exceptionally thermally conductive, which lends them well to use in thermally reactive thermoset composites. Depending on the manufacturing process and product requirements, either continuous fibers or discontinuous fibers can be used. Better mechanical properties can be achieved using continuous fibers, but discontinuous fibers offer easier processing.

Common manufacturing methods of polymer-matrix composites are shown in Table 1-3.

Table 1-3: Common composite manufacturing processes [2–5].

Manufacturing Processes	**Overview**
Pultrusion	Resin-swelled fibers are pulled through a heated shaping die, which initiates cure in the thermosetting resin and forms the shape of the continuous length of the pultruded product.
Filament Winding	Continuous filaments in the form of roving are saturated with resin and machine wound onto mandrels having the shape of the finished part. Once winding is complete, the whole assembly is placed in an oven for curing.
Manual Layup	Additional layers of reinforcement and matrix are laid on top of each other until the desired thickness is achieved. The layered structure can be vacuum bagged or allowed to cure in an oven for better properties.
Liquid Composite Molding	This process includes injection molding, RTM, and RFI. Typically, dry, continuous fiber is impregnated with matrix material through infusion or injection, or discontinuous fiber is injected into a mold.
Additive Manufacturing	Most commonly, discontinuous fiber, either in the form of filament or a high viscosity slurry, is deposited on a print bed layer-by-layer via an extrusion-based process. Processing can also be adapted to SLA, SLS, and continuous fiber applications.

The ideal manufacturing process varies based on the desired product geometry, cost, and materials systems. When matrix and reinforcement materials are combined through these processes, a unique set of properties can be observed that cannot be achieved with either of the constituents alone [1]. As a result of the unique combination of materials, composite materials often exhibit extremely tailorable properties, high strength-to-weight ratio, and high thermal stability. This offers an advantage over traditional engineering materials. Because of the many advantages, composite materials, especially carbon fiber-reinforced thermoset polymers, are widely used in a variety of industries. These composite materials are commonly seen everywhere from the sporting goods industry to the aerospace industry.

Despite all the advantages of composite materials, the traditional manufacturing processes can be complex and expensive due to high labor, energy, and time demands [6]. Traditional manufacturing processes typically require the use of complex tooling to produce desired geometries. This tooling can take months to produce and can account for more than 30% of the final product cost [7]. The requirement of tooling inherently produces limitations in part geometry that can be produced. The traditional methods of composite processing typically require bulk heating of the material and tooling for hours until the matrix thermoset resin is cured [8]. This process is typically carried out in an autoclave, where pressure, vacuum, and heat is applied to consolidate and densify composite parts [1]. While this process is energy- and time-intensive for all geometries, it becomes especially cost-prohibitive when used in large, industrial settings as seen in Figure 1-1.

Figure 1-1: Industrial autoclave used to manufacture airplane wings for Boeing [9].

To address these issues, several approaches have been developed to rapidly cure the thermosetting matrix resin. Photocurable resins have been proposed as an alternative and work by using ultraviolet (UV) or visible light to cure thermosetting resins. This approach is best suited for use with additive manufacturing, but unfortunately these resin systems cannot be used with opaque or highly filled inks and typically result in polymers with poor mechanical properties [10]. Frontal polymerization (FP) is an alternative curing approach where a self-sustaining exothermic reaction wave converts liquid monomers into fully cured polymers [11]. This technology not only accelerates the composite manufacturing process significantly, but it also offers enhanced energy absorption and fatigue resistance compared to other high-performance composites [11]. This FP technology is applicable to molding, imprinting, 3D printing, and resin-infusion techniques [11].

In FP technology, a solution containing monomers and a latent initiator is heated locally until the initiator is activated for polymerization of the monomer [11]. This reaction produces heat which drives the exothermic reaction chain [11]. The requirement of FP, is that the polymeric resin should have a high energy density and reactivity in order for the reaction to occur [11]. Many of the materials utilized in FP, including functionally graded polymers, nanocomposites, hydrogels, sensory materials, and fiber-reinforced polymer composites, are not suitable for high-performance applications [11].

The solution to this limitation is found in the work done by I. D. Robertson et. al. [11]. The incorporation of frontal ring-opening of dicyclopentadiene (DCPD) using a thermally activated ruthenium allows for the formation of polydicyclopentadiene (pDCPD) as seen in Figure 1-2 [11]. pDCPD is a cross-linked thermoset polymer that has high fracture toughness, impact resistance, stiffness, and chemical resistance. When pDCPD polymer is used as a matrix material in composite manufacturing, excellent mechanical properties can be obtained.

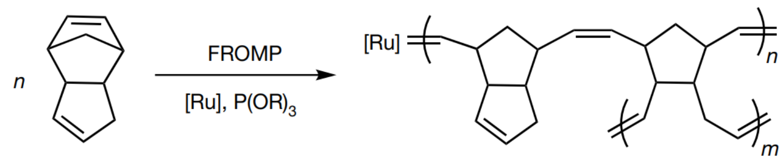

Figure 1-2: Scheme for the FROMP of DCPD using a ruthenium catalyst (2nd generation Grubbs' Catalyst) [11].

While frontal polymerization offers a solution to most of the issues encountered in traditional composite manufacturing, it is still limited by low front velocities, reaction quenching, and difficulties in maintaining high front velocities when using a high concentration of fillers or reinforcements [8,10,12–14]. A few methods can be used to speed up this process. Applicable to a wide variety of materials, electromagnetic radiation energy can be continuously provided to accelerate the FP reaction and further increase composite manufacturing rates [8]. At this time, this has been shown in the form of laser-assisted heating [8] and infrared heating [15]. While this concept can be applied to most forms of composite manufacturing, the focus of this research is on additive manufacturing and filament winding.

1.2.2 Additive Manufacturing

Additive manufacturing (AM), or 3D printing, is a bottom-up manufacturing approach which involves repeatedly depositing and solidifying materials in layers to build 3D objects [16]. This method of manufacturing provides unparalleled design freedom for complex geometries and is applicable to a wide range of materials [16]. A brief overview of the most common additive manufacturing technologies and their basic characteristics are shown in Table 1-4.

Table 1-4: Standard terminology for additive manufacturing technologies [17].

Additive Manufacturing Process	Basic Overview
Binder Jetting	Liquid bonding agent is selectively deposited to join powder materials.
Directed Energy Deposition	Focused thermal energy is used to fuse materials by melting them as they are being deposited.
Material Extrusion	Material is selectively dispensed through a nozzle or orifice.

Material Jetting	Droplets of build material are selectively deposited.
Powder Bed Fusion	Thermal energy selectively fuses regions of a powder bed.
Sheet Lamination	Sheets of material are bonded to form an object.
Vat Photopolymerization	Liquid photopolymer in a vat is selectively cured by light-activated polymerization.

Each one of these additive manufacturing processes has its own advantages and disadvantages. The focus of this research lies in the material extrusion realm, more specifically called Direct Ink Writing (DIW).

DIW is a method of 3D printing that uses a computer-controlled, ink-deposition nozzle to create materials with controlled architecture and composition [18]. A variety of materials can be printed using DIW, but the most common are resins, colloidal inks, polyelectrolyte inks, and sol-gel inks [19]. Upon deposition, these inks solidify due to evaporation, gelation, solvent-driven reactions, or thermal energy [19]. It is important to tune the rheological properties of the inks being printed in order to form a predictable and stable 3D structure [19].

When DIW is used with thermosetting resins and reinforcement fibers, various processing conditions can be used. Continuous fiber additive manufacturing can lead to higher mechanical properties but is more difficult to capture certain geometries and involves more complex printing setups. Discontinuous carbon fiber printing is easier to process but can lead to lower mechanical properties. Depending on the length and alignment of the discontinuous carbon fibers within the ink, properties can vary drastically. Many resin systems exhibit shear thinning properties, which allow for high fiber alignment and tunable material properties. When shear stresses are induced during extrusion, viscosity of the ink decreases, and as a result discontinuous fibers are aligned along the flow direction [20].

In order to successfully print using DIW, a nozzle dispensing process is required. Dispensing is typically done in the form of either pneumatic dispensing or pump-driven dispensing. Pneumatic dispensing uses air pressure to extrude the ink. This is commonly seen among gantry-style 3D printing systems but requires careful control over air pressure during the printing process and can result in uneven print diameters. The alternative, pump-driven dispensing, often uses a motor to print based on linear motion (speed) as opposed to using pressure. The advantage of this method is the ability to accurately start and stop deposition consistently. This becomes especially advantageous during printing where the viscosity of the ink does not remain constant during the printing process. One example is in inks where the resin gels over the course of its pot life. Assuming the motor has enough power to continue extrusion, the deposition is much more consistent.

While DIW can be used to print complex geometries, it often requires the use of support materials. The use of support materials requires post-processing to remove the support and can lead to material waste. In addition, the support material constrains part orientation and part quality. Due to the inherent disadvantages of using support materials, it is advantageous to seek alternative, freeform manufacturing methods that do not require them.

Without using support materials, most printing processes are limited to 2.5D or simple 3D geometries. A 2.5D object is simply the extrusion of a 2D profile, with no variation in the XY geometry with respect to height [21] as seen in Figure 1-3. Without support materials, some 3D geometries can be created effectively, but this can be influenced by the material properties, as well as the printing process and the amount of overhang required.

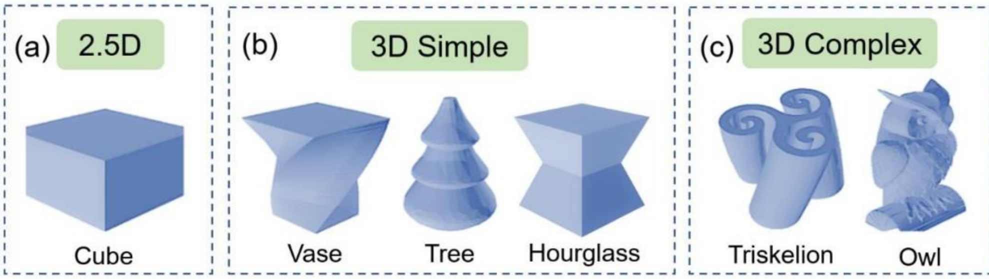

Figure 1-3: Different levels of 3D printing part complexity [21].

1.2.3 Frontal Polymerization in Additive Manufacturing

One promising solution to the issue of geometry constraints is the incorporation of FP curing strategy to the additive manufacturing process. AM using frontal polymerization is very effective at producing freeform geometries but is limited by low front velocities, front quenching due to heat losses, and low front reactivity in the presence of a high concentration of fillers and reinforcements [8]. To overcome these challenges, work has been done to combine the thermoresponsive thermoset resin used in frontal polymerization, with localized, photothermal heating to speed up the process, decreasing the effect of thermal boundary conditions, and to increase the amount of additives that can be used in the resin [8]. By using this AM technique, support materials are essentially eliminated, and overhang of any geometry can be accurately printed as seen in Figure 1-4.

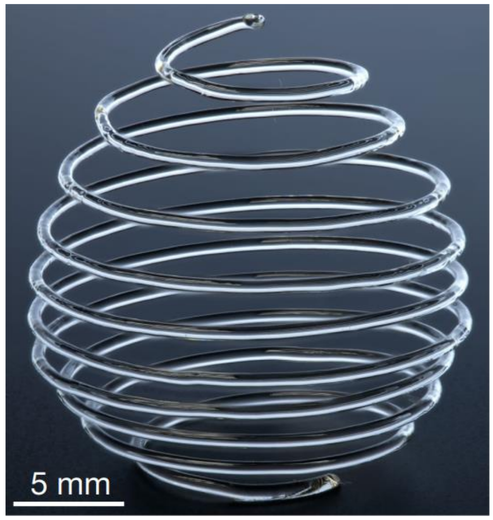

Figure 1-4: Complex, free-form 3D printed structure manufactured using frontal polymerization [11].

While this approach solves the issue of geometry constraints, there still lies the issue of scalability, meaning the design is strictly constrained by chamber volume of 3D printers [22]. Generally, 3D printing technologies use a gantry system [22], which can be difficult to scale due to large printhead inertias. Robotic-arm based systems have been used for AM, but the print size is still limited to the reach of the robotic arm [22]. A common workaround to this problem is to print smaller pieces, then assemble them [22]. This significantly increases the complexity of the system and creates potential weaknesses at the assembly interface [22]. This is where the concept of mobile additive manufacturing really shines as it allows for unlimited planar range and therefore increased build volume [23].

1.2.4 Mobile Additive Manufacturing

Mobile additive manufacturing (MAM) is an alternative and promising strategy of AM that increases part size capabilities, removes power source constraints associated with traditional AM, and allows for the application of manufacturing and repair in remote and potentially hazardous areas. MAM is a form of AM where the printer is completely mobile during the printing process [24]. This technology allows for AM at a larger scale with higher speeds than traditional AM systems [25]. Not only does MAM allow for virtually unlimited build volumes, but it also opens doors for cooperative additive manufacturing (CAM) where multiple mobile 3D printing robots can be assigned sections of a large part and print in parallel with each other to increase part throughput [25–27] .

The focus of this work relies on a singular, low-budget, wheeled platform. This wheeled platform allows for unlimited planar range, and therefore, increased build volume compared with traditional AM processes [23]. The platform used utilizes mecanum wheels for maximum movement degrees of freedom. These mecanum wheels can create force vectors in both the X- and Y-directions by varying the individual wheel speed and direction, allowing the robot to move omnidirectionally on the X-Y plane as seen in Figure 1-5 [28]. These systems also typically contain a Z-stage consisting of a vertical, motor-controlled deposition system to enable part dimensionality. This research aims to combine the mechanical advantages of thermoset resin matrix composites with the freedom of MAM to achieve large parts with desirable properties. This research has applications for high-strength, in-situ repairs in remote, hard-to-access, and potentially extraterrestrial locations.

Figure 1-5: Low-budget, wheeled platforms [29].

1.2.5 Current Research Literature on Mobile Additive Manufacturing

Over the past few years, there have been many demonstrations of mobile additive manufacturing. Several different approaches have been taken with regards to material being extruded, mobile platform locomotion, mobile platform control, and geometrical features of printed parts.

The most commonly used materials in MAM are traditional building materials such as concrete. Zhang et al. [22] developed a multi-robot system that utilizes 6-axis robotic manipulators to deposit a cementitious material that was rheologically optimized for printing via the viscous extrusion printing technique. This multi-robot system was the first demonstration of a large-scale, concurrent 3D print of a concrete structure by multiple mobile robots. This work involved complex motion planning to ensure that the platforms printed accurately without collision. The final structure was 1.86 m x 0.46 m x 0.13 m and helped to showcase the advantages of MAM, specifically when considering print efficiency and scalability.

While these materials would prove to be beneficial for large-scale construction, the printing process and parameters differ from polymeric materials. MAM systems have been adapted for melt extrusion printing as well. Marques et al. [29] developed a low cost MAM system which was capable of printing with standard thermoplastic filaments such as ABS. This system was more limited in terms of material manipulation as it included only a z-stage in conjunction with omnidirectional motion. As a result, this system proves to be considerably less expensive than systems utilizing 6-axis robotic manipulators. This work proved the feasibility of MAM using polymeric materials.

To the best of the author's knowledge, only one instance of thermoset polymeric material has been demonstrated in the field of MAM. Kayser et al. [30] developed a biomimetic mobile platform (Fiberbot) capable of printing continuous fiber composites. While the work done is technically additive manufacturing, it more closely mimics filament winding as continuous fiberglass roving was impregnated with UV curable resin and wound around an inflatable mandrel to cure. With these mobile platforms, a structure was manufactured that stood 4.5 m tall. This structure, as seen in Figure 1-6, withstood damage from weather including rain, strong winds, and heavy snow for a period of 7 months. This demonstration helps to highlight the importance of high-strength materials in the field of MAM, and more specifically, fiber reinforced thermoset composites.

Figure 1-6: Large fiberglass reinforced structure created by Fiberbots [30].

In addition to manufacturing high-strength materials, Fiberbots were developed to deposit the material by mimicking the biological tendencies of ants, bees, and termites where they crawl on their own structures to expand work volume as seen in Figure 1-7. This is a relatively unique form of locomotion in the field of MAM, but it opens the doors for a variety of possibilities.

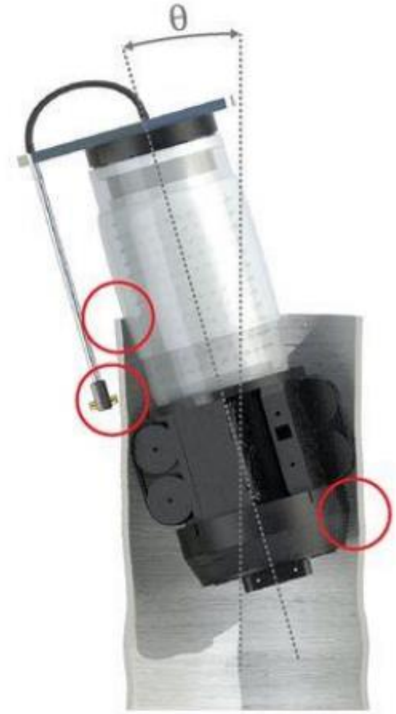

Figure 1-7: Biomimetic mobile platform that crawls on its own structure [30].

While the biomimetic mobile platform allows for unique geometries, it is relatively constrained in its locomotion. As a result work has been done to adapt MAM systems for use with aerial platforms as seen in Figure 1-8. Zhang et al. [31] developed a printing and scanning system for aerial robots to increase access and scalability. By incorporating a team of small mobile robots, greater flexibility can be achieved to build geometries larger in size than individual robots themselves. A 2.05 m tall, cylindrical print demonstrated the capabilities of the system and its ability to print with a relatively high precision.

Figure 1-8: Cementitious, cylindrical print demonstrating the capabilities of aerial additive manufacturing [31].

While aerial additive manufacturing opens up possibilities for remote and large-scale manufacturing, the aerial robots are limited in payload, battery life, and the print accuracy is susceptible to any variations in wind conditions. A similar alternative can be seen in the work done by Barnett et al. [32], where a cable-suspended 6-DOF robotic platform is used as a mobile printer. Researchers constructed a 2.16 m tall statue using this method, but it had to be assembled in pieces due to workspace limitations. While this technique solves the issue of payload and battery life that is seen with drones, it is much more limited in terms of remote and large-scale manufacturing, as there is required infrastructure setup prior to printing.

Perhaps the most commonly seen form of locomotion amongst MAM systems are wheeled platforms. There have been several instances of research efforts in this field, but most notable to this research is the platform designed and manufactured by Marques et al. [29] as mentioned above. Most notably, this system is low-cost and untethered, allowing for easy scaling and cooperative printing. This system consists of omnidirectional wheels to allow for motion in any direction on the x-y plane as well as a z-stage to add dimensionality to prints as seen in Figure 1-9.

Figure 1-9: Simple. low cost robotic platform for MAM [29].

Because of the flexibility of this system in terms of size, payload, and cost, modifications are easy, allowing for easy adaptation to fit process specific needs. Similar work has been done by Sustarevas et al. [33] to overcome rough terrain with disturbance rejection and a modified, four legged design as seen in Figure 1-10.

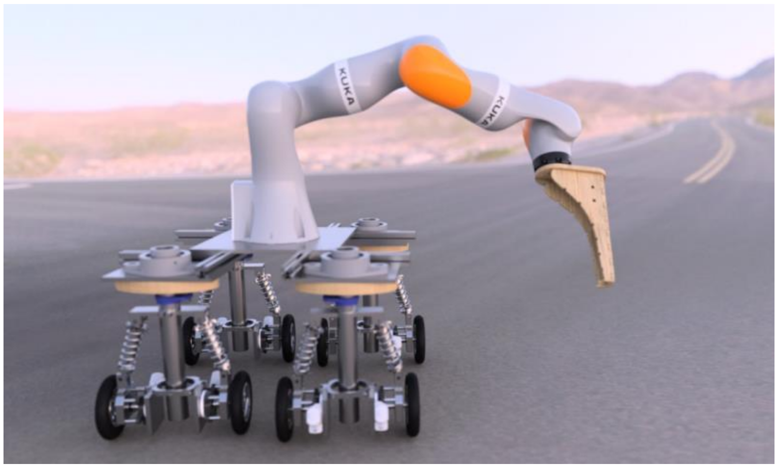

Figure 1-10: Modified, highly agile mobile platform for on-site construction [33].

In similar work by Lachmayer et al. [34], the issue of uneven print surfaces was addressed by scanning ground contours using a high-precision 2D line laser and adapting robot motion accordingly. This work transitions into a significant segment of the activity in the MAM field, which primarily involves algorithm-based tasks related to part programming and motion planning. Sustarevas et al. [23] developed a Task Consistent Path Planning algorithm that complements a model predictive controller to allow for motion planning for a given print task and robotic kinematic model. When taking multiple, autonomous robots into consideration, a need arises for planning. While print speed significantly increases with more robotic platforms, control difficulty significantly increases as well. A chunk-based printing strategy to enable cooperative 3D printing based on simple heuristics has been developed by Poudel et al. [27].

Despite the growing research effort in the field of MAM, there lies a gap as all previous MAM systems are ill-suited for printing overhang geometries and incapable of printing freeform geometries. To the best of the author's knowledge, the funicular geometries seen in Figure 1-11, produced by Lakhal et al. [35], are the most complex part that has been produced with a MAM system.

Figure 1-11: Funicular architectural geometry manufacturing using a holonomic platform [35].

In addition, the fiberglass-reinforced architectural structures created by Fiberbots are the only application of advanced materials in the field of MAM. There lies a need for the application of complex geometries with high mechanical properties to best fit the needs of the remote, hazardous manufacturing that MAM is best suited for. This is where the application of printing thermally curable thermosetting composites comes into play to help revolutionize the field of MAM.

1.2.6 Filament Winding

In a slightly different vein of research, the manufacturing process of filament winding is one of the most efficient and least costly automated methods of processing polymer composites [36]. In this process, continuous strands of fiber are wound around a supporting form or mandrel. Filament winding is particularly effective at producing tube and pipe shaped objects, but can be adapted for more complex geometries as well [37].

Many forms of filament winding machines have been developed and used in industry. These machines can be separated into two different categories based on the method by which fibers are wound on the mandrel. The first is called wet winding and is based on passing dry fibers through a resin bath and then winding them around a mandrel as seen in Figure 1-12. The second is prepreg winding, where preimpregnated fiber tows are placed on the rotating mandrel [38]. The primary focus of this research is wet winding.

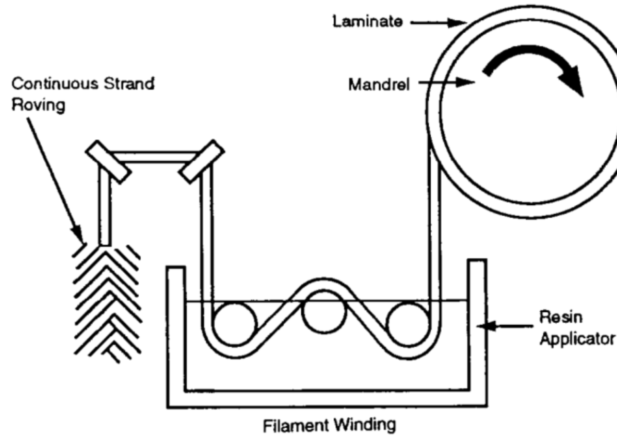

Figure 1-12: Schematic illustrating continuous dry fibers being pulled through a resin bath to impregnate the fibers with resin [37].

During the wet winding process, fibers under tension are typically pulled through a resin bath with rollers to impregnate the dry fibers with resin. Fibers are then wound around a mandrel in varying angles, depending on what material properties are desired. In the hoop winding, the fibers are wound perpendicular to the cylindrical axis [38]. This is effective for pressure vessel applications where there is a focus on hoop stress. In a helical winding, fibers are wound at an angle with respect to the cylindrical axis as seen in Figure 13. Depending on the desired mechanical properties, the winding angle can be varied to match the application. In a polar winding, fibers are wrapped pole-to-pole on a rotating, domed-end mandrel [38]. This is especially useful for producing composite pressure vessels. Figure 1-13 demonstrates examples of each winding angle.

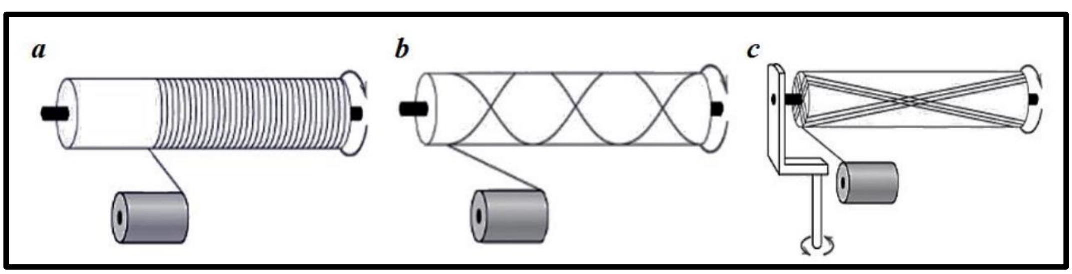

Figure 1-13: Different winding angles; a) hoop winding; b) helical winding; c) polar winding [39].

The complexity of the geometry that can be produced by filament winding relies on the complexity of the machine. The simplest and most affordable filament winding machine is a two-axis winding machine. The first axis is for rotating the mandrel on which fibers are placed and the second axis is for the translating motion of the resin bath. This simple machine is best suited for the manufacturing of simple geometry such as cylinders and tubes. Figure 1-14 shows a simple two-axis filament winding machine similar to the one used in this research.

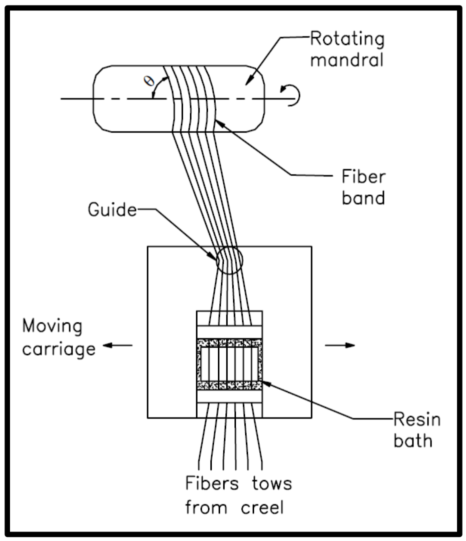

Figure 1-14: Simple, two-axis filament winding system [38].

For more complex geometries, the machine setup can be scaled accordingly. Commonly used systems are based on six-axis robotic arms. These systems allow for unparalleled control over the winding process, leading to the creation of complex, high-quality parts. Oftentimes, these robotic arms are coupled with a one-axis headstock or two-axis turntable to allow for even more degrees of freedom in the design. The setup seen in Figure 15 consists of a six-axis robotic arm paired with a two-axis turntable.

Figure 1-15: Researchers at the University of Stuttgart using a complex filament winding machine for winding of structural, fiber-reinforced composite parts [40].

As seen in Figure 1-15, mandrels are not limited to only cylindrical shapes. There are two main categories of mandrel, namely core and coreless. Core mandrels are typically solid and can either be removed during post-processing, or in the case of most pressure vessels, can be left inside after the composite manufacturing process is completed. To remove a cored mandrel, high pressure hydraulic presses are frequently used, although dissolvable mandrels can be used as well. Dissolvable mandrels are typically made of sand, plaster, eutectic salt, foam, or a low-melting-point alloy [37]. Coreless mandrels are typically comprised of a series of pins or nodal points around which impregnated roving is wrapped. Coreless mandrels allow for facile manufacturing of rigid, frame-like products with easy control over fiber orientation [41].

Following the winding process, it is necessary to initiate the curing of the composite. The most commonly used approach is the process of curing using a batch oven or autoclave. Care must be taken to control important process variables such as temperature and the degree of cure [42]. The thicker the composite part, the more difficult it is to control these process variables as there is a temperature gradient within the composite part and a temperature overshoot can result in the degradation of the matrix material. More uniform temperature distribution across thickness results in a more uniform degree of cure within the part [42]. In composite manufacturing, typically a consolidation pressure is required during the cure cycle for obtaining a high volume fraction of fibers and uniform resin distribution. This is generally not required for filament wound parts as the surface curvature of the mandrel and the roving pretension produce sufficiently high compression radially [43]. Occasionally, shrink tapes are used to apply radial-compression forces on wound fibers, but this is mostly to increase the outside surface quality of the part and not to provide consolidation pressure [41].

The focus of this work is on a simple, two-axis filament winding machine and improving the filament winding process by introducing a thermally curable, thermosetting resin. This new process allows for significantly reduced manufacturing times and reduced energy inputs.

1.2.7 Current Research Literature on Filament Winding

Filament winding is a well-researched field, as it has been proven to be a cost-effective and easy way to produce automated composite parts. Substantial research effort has been directed towards optimizing process parameters, simulating winding cycles, and developing low-cost systems.

Because of its inherent complexity, a number of factors directly affect the quality of filament wound parts. The most important factors are fiber tension, viscosity of resin, and degree of cure. Cohen [44] experimentally developed a relationship between winding tension and fiber volume, where it was shown that increasing the winding tension results in an increased fiber volume. Additionally, it was demonstrated that the lower the viscosity of the resin, the more fiber compaction, ultimately resulting in higher fiber volume fraction. On a similar note, Lee et al. [45] developed a model that directly evaluates the effects of cure on the strengths and moduli of composites after manufacturing as seen in Figure 1-16. Conclusions about the performance of the composite part can be drawn based on the degree of cure, considering the properties of the resin and fiber.

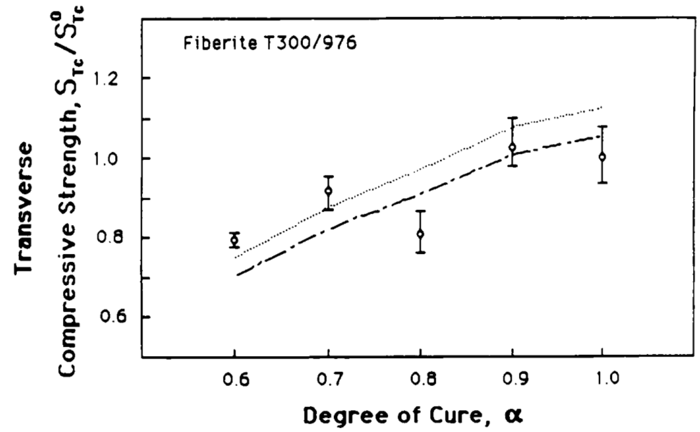

Figure 1-16: Transverse compressive strength as a function of degree of cure as developed by Lee et al. [45]

In addition to the research done for understanding the effects of basic processing parameters, significant research has been undergone to optimize programming and control of the filament winding process as well as the simulation of this manufacturing process. Mazumdar et al. [46] were among the first to analyze the kinematics involved in capturing the desired geometries using filament winding manufacturing methods. Their studies helped to pave the way into understanding key programming parameters such as wind angle, fiber positioning, and delivery point movement. Zhang et al. [47] developed a finite element model of the wet filament winding process to calculate fiber volume under various processing conditions using a combination of a fiber consolidation/ compaction model, thermomechanical model, and thermochemical model.

In recent years, considerable research efforts have been conducted to establish low cost filament winding machines. Most recently, Andrianov et al. [48] developed a low-cost, four-axis filament winding machine using off-the-shelf components, an obsolete computer, and an affordable control system as seen in Figure 1-17. They used analytical equations for delivery-eye trajectory capable of laying fibers straight along a geodesic trajectory. A multitude of other work has been performed in the area to make filament winding technology as affordable and accessible as possible.

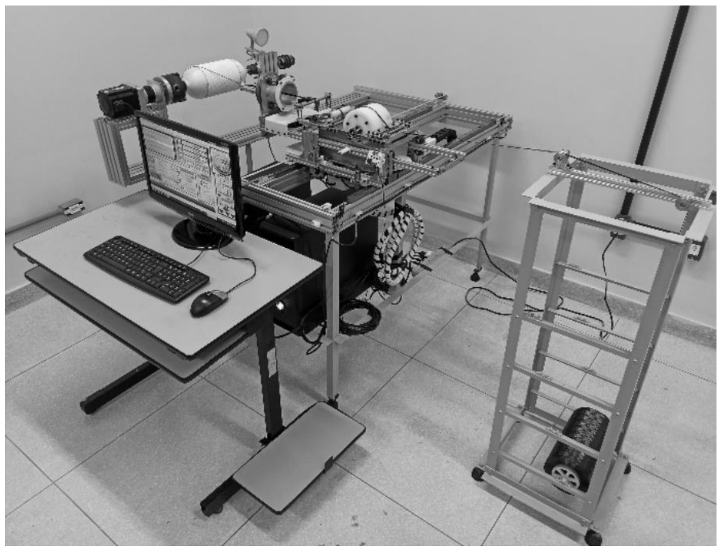

Figure 1-17: Four-axes filament winding machine developed by A. Andrianov et al. [48].

Little research has, however, been performed on the optimization and improvement of the curing cycle. Traditional filament winding relies on conventional curing of filament wound parts using autoclaves and ovens. While this method of manufacturing is mature, it can be expensive, labor- and power-intensive, and difficult for manufacturing large parts. When dealing with especially thick composites, this traditional approach can lead to large thermal stresses due to non-homogenous curing and unavoidable temperature gradients [49].

To address these manufacturing burdens, several alternative curing methods have been explored. Burwasser et al. [50] studied a novel method of curing composite cylinders via electrothermal heating by applying a voltage across the fibers of the filament wound part, both during and after the wind, to act as a large resistive heater. It was determined that doing so helped minimize temperature gradients inside the material. However, large voltage requirements and unresolved details make practical applications of this concept quite challenging.

To increase part throughput during manufacturing, Kim et al. [51] proposed a novel curing technique called continuous curing. This technique was engineered for creating extremely thick composite parts made from thermosetting polymer matrix composites. During this process, layers of uncured material are added to a heated mandrel. This mandrel initiates an exothermic chain reaction that can be matched to the wind speed to produce a continuously curing part with no thermal spikes throughout the wind [42]. This process allows for rapid manufacturing of composite parts when compared to traditional autoclave processes. Similarly, Tabuchi et al. developed a similar method with the exception that heated air was used on the interior surface of the mandrel to initiate this thermal front. While these curing techniques help to increase part throughput, they are fairly complex in application and require heated tooling to function properly.

These limitations motivate the need for a simpler approach for thermal curing of thermosetting matrix composites in filament winding systems. Infrared radiation (IR) heating is an alternative, non-contact method of heat generation where electromagnetic energy is converted to heat by the vibration resonance of molecules. It is especially important to control the radiation intensity applied during this process to prevent material degradation. Kumar et al. studied the feasibility of infrared curing of glass fiber-reinforced composites by varying the distance of IR source from the composite laminate, curing schedule, and volume of composite to determine important processing parameters. Under optimal conditions, no strength losses were reported, and curing time was reduced considerably. Further work has been performed by Nakouzi et al.

[52] to simulate IR heating for composite curing and aimed to predict heat distribution throughout the composite as well as the degree of cure as a function of time.

Despite the research done thus far in the field of filament winding, there still remains a need to reduce manufacturing time and reduce power consumption during the process. By combining the ideas of frontally curable thermosetting resin systems with IR heating, high part throughput can be achieved using low-cost systems to produce parts with a variety of geometries.

1.3 Thesis Objectives

The overall objective of this thesis is to apply the benefits of thermally curable thermoset resins to various composite manufacturing methods to address challenges with developments of composite structures. The specific objectives of this research work are as follows.

1.3.1 Mobile Additive Manufacturing

- Design, manufacture, and assemble mobile robotic platform for additive manufacturing.
- Identify and quantify parameters related to print quality.
- Evaluate physical quality of printed structures.
- Demonstrate unique capabilities of the mobile robotic platform.

1.3.2 Filament Winding

- Improve pre-existing filament winding system for repeatable composite structure manufacturing.
- Identify and quantify parameters related to composite structure quality.
- Evaluate physical quality of manufactured structures.

- Optimize curing strategy for rapid, energy efficient manufacturing of filament wound composite structures.

Chapter 2. MOBILE ADDITIVE MANUFACTURING

2.1 Introduction

This chapter focuses on the design and manufacturing of a mobile additive manufacturing system developed to print discontinuous carbon fiber-reinforced composites using thermally assisted frontal polymerization. This entire system was developed from scratch with a tight budget. Throughout the research, five design iterations were performed to create the most robust and reliable platform possible. The five design iterations are outlined briefly in Table 2-1.

Table 2-1: Design Iteration Outline

Design Iteration Outline	
Design Iteration One	Initial design and evaluation of a simple mobile robotic platform.
Design Iteration Two	Updates to circuitry for more reliable platform operation.
Design Iteration Three	Incorporation of thermal stimulus for printing using frontal polymerization.
Design Iteration Four	Incorporation of linear actuator extrusion system, laser rotation, and untethered operation.
Design Iteration Five	Incorporation of modular print head design and XY coordinate programming.

The following sections are chronologically organized so that the experiments performed have the proper context in terms of design iteration.

2.2 Design Iteration One: Simple Platform Design

2.2.1 Design Work

This is the first iteration of design for this mobile robotic platform. In this iteration, the basic platform for additive manufacturing is designed. Initially, the design intent of the MAM system was to retrofit a pre-existing robotic platform for additive manufacturing. After considerable market research, it was determined that there was not a suitable platform on the market for retrofitting. The main variables taken into consideration for this were platform control, platform load capacity, platform size, platform motors, and cost. Table 2-2 shows a comprehensive list of all of the platforms that were considered for retrofitting.

Table 2-2: Comprehensive list of robotic platforms on the market.

Omnidirectional Robot Platforms									
BRAND	Price	Spec Sheet Link	Buy Link	Code	Plaftorm Size (in^2)	Program Platform	In Stock?	# of Motors	Review (x/5)
OSOYOO	$129.97	N/A	https://www	C++	49	Arduino Workaround	Y	4	4.3
MYAGV	$849.00	https://download-e	https://shop	Python	114	Raspbery Pi	Y	4	5
NEXUS	$276.00	http://www.nexusrc	https://www	C++	45	Arduino	Y	4	N/A
SEEED	$91.24	https://media.digik	https://www	C++	16	Arduino	Y	3	N/A
TURTLEBOT	$648.30	https://emanual.rob	https://www	Python	31	Raspberry Pi	N	2	5
MOEBIUS	$149.99	N/A	https://www	C++	93	Arduino	Y	4	3.8
NEXUS	$648.00	https://www.robots	https://www	C++	49	Arduino	Y	3	4
NEXUS	$121.00	N/A	https://ozro	C++	31	Arduino	Y	3	N/A
HIWONDER	$239.99	N/A	https://www	Python	46	Raspberry Pi	Y	4	N/A
YAHBOOM	$130.89	https://cdn.robotsh	https://www	C	20	Serial Communication	Y	4	N/A
MYAGV	$699.00	N/A	https://ozro	Python	95	Raspebery Pi	Y	4	N/A
NEXUS	$121.00	N/A	https://ozro	C++	11	Arduino	Y	3	N/A
NEXUS	$599.00	N/A	https://ozro	C++	39	Arduino	Y	3	N/A
LYNXMOTION	$895.95	https://www.robots	https://www	C++	216	BotBoarduino	N	4	N/A
LYNXMOTION	$695.95	https://www.robots	https://www	C++	216	Arduino	N	4	N/A
DFROBOT	$35.99	https://www.robots	https://www	C++	35	Arduino	Y	2	5
NEXUS	$770.00	https://www.robots	https://www	C++	223	Arduino	N	4	N/A
KING KONG	$1,500.00	N/A	https://www	C++	190	Arduino	N	4	N/A
HIWONDER	$199.99	N/A	https://www	C++	92	Arduino	Y	4	N/A
NEXUS	$624.00	https://www.robots	https://www	C++	133	Arduino	N	4	3.1

Based on this analysis, it was determined that it would be more cost-effective to create a custom platform as opposed to retrofitting one. To start with, an aluminum chassis was sourced from a previous project. This chassis provided a large platform to house all the necessary components. After the chassis was sourced, the mecanum wheels were sourced. When determining which mecanum wheels to use, the wheel diameter, part availability, and price were considered. Smaller diameter wheels are desirable in this application to reduce the amount of torque required to rotate the wheels. Four-inch mecanum wheels are generally the smallest commercially available wheels, so they were selected.

From here, it was necessary to source the electrical components. This included the research and procurement of the necessary stepper motors, stepper motor drivers, microcontrollers, and miscellaneous circuit components. To determine which stepper motor would work best for use with the mecanum wheels, the chassis size constraint as well as motor torque were considered. The largest motors compatible with the chassis were frame size NEMA 17, which can produce 3.2 kg of torque at 1.2 A [53]. To determine if this was enough torque, Equation 1, applied in Figure 2-1, was used to determine the friction force between the wheel and the floor.

$$F = \frac{\mu m g}{4} \tag{1}$$

Next, the torque at the estimated mobile robotic platform (MRP) mass was calculated using Equation 2 and as applied in Figure 2-1.

$$T = Fr \tag{2}$$

The results of these calculations are shown below in Figure 2-1 with the assumption that the mass is distributed evenly on the platform. The coefficient of friction was calculated using linear interpolation from research done by Sonawane et al. [54].

Known Variables			
Variable	Definition	Value	Units
r	Wheel radius	50	mm
μ	Coefficient of friction	0.31	-
m	Estimated mass of the MRP	5.0	kg
g	Acceleration due to gravity	9.8	(m/s^2)
T_{MAX}	Stepper motor torque at 1.2 A	3.2	kg-cm

Variables Being Solved For		
Variable	Definition	Units
F	Friction force between the wheel and floor	N
T	Torque required for each stepper motor	kg-cm
m_{MAX}	Load capacity before torque issues	kg

Calculations		
Variable Solved For	Calculated Value	Units
F	3.80	N
T	1.94	kg-cm
m_{MAX}	8.26	kg

Figure 2-1: Determined viability of NEMA 17 stepper motors using torque requirements.

Once motors were selected and specifications were verified, compatible motor drivers were researched and selected. These motors were initially controlled with an Arduino Uno microcontroller due to user familiarity as well as microcontroller availability. Later, the microcontroller was updated to an Arduino Mega so that more digital pins could be utilized.

With the components initially sourced, design work began to integrate everything. Typically, these mecanum wheels are used with DC motors, so it was necessary to design and manufacture custom wheel hubs so that they could be used with stepper motors. To do so, the wheel hub seen in Figure 2-2 was machined out of 6061 aluminum on a lathe and CNC milling machine.

Figure 2-2: Custom machined wheel hubs to adapt stepper motors to mecanum wheels.

Next, components were designed and 3D printed to mount the stepper motors to the chassis. At this point, the mobile platform consisted of just four mecanum wheels, four stepper motors, and an aluminum chassis. The z-stage of the mobile platform was designed and assembled by integrating linear motion shafts, linear ball bearings, external retaining rings, and clamping shaft collars (all sourced from McMaster Carr) using the 3D printed components as seen in Figure 2-3.

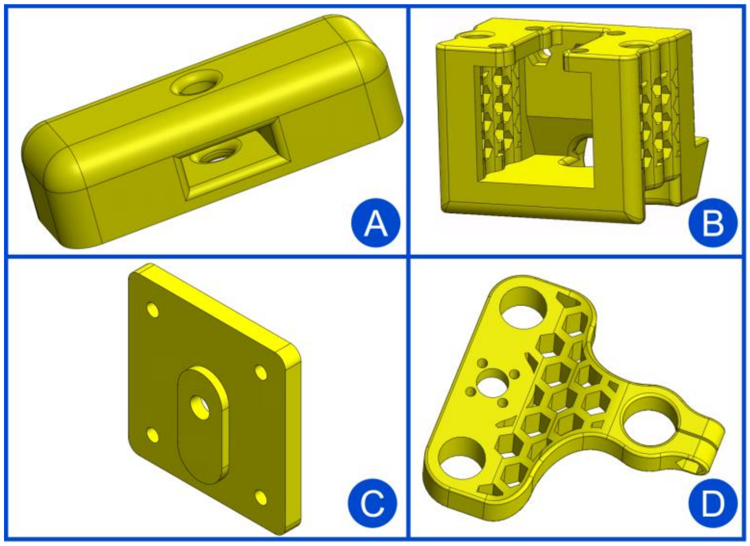

Figure 2-3: SolidWorks models of 3D printed parts currently on MRP. a) Top of the z-stage system that houses a ball bearing and two linear motion shafts. b) Stepper motor housing with cooling vents, wiring channels, secure nut/bolt attachment system, and linear motion shaft containment. c) Stepper motor adaptors to easily mount the stepper motors to the chassis. d) Syringe holder carriage that encases the linear ball bearings and travel nut on the stepper motor lead screw.

At this point, the first iteration of the mobile platform was created as seen below in Figure 2-4. Initially, the capabilities of this platform were limited. It could move in any direction in the x-y plane, move the syringe and printing nozzle in the z-direction, and print using pneumatic pressure, but had no capabilities to cure resin by means of a thermal stimulus.

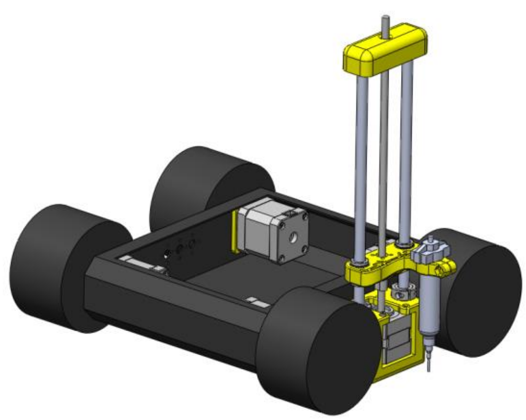

Figure 2-4: SolidWorks assembly highlighting the design of the mobile platform and how 3D printed parts interface with sourced components.

With a basic platform completed, the circuit was built using a plastic breadboard and the necessary electrical components as seen below in Figure 2-5.

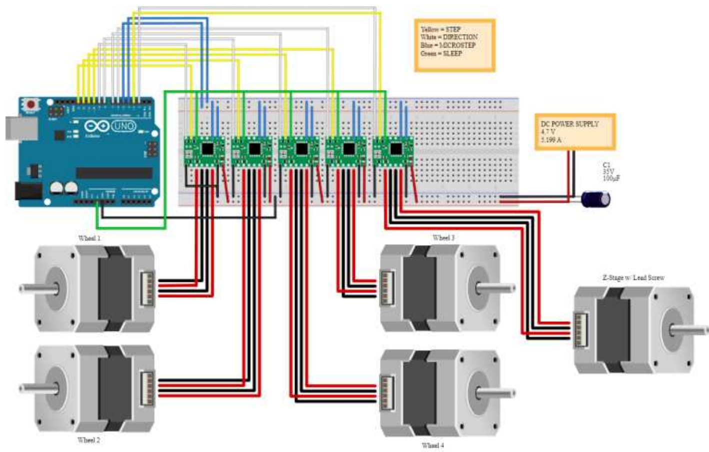

Figure 2-5: Comprehensive wiring diagram for mobile platform at this stage.

The end result of this design iteration can be seen below in Figure 2-6.

Figure 2-6: Final assembled platform for design iteration one.

2.2.2 Formal Experimentation

With the first iteration of the mobile platform assembled, some validation experiments were run to determine baselines for motion and whether or not a redesign was warranted. The first experiment focused on establishing a worst-case, straight-line baseline.

Initial Platform Validation

To initially validate the platform, a square of 3,000 x 3,000 steps (approximately 350 x 350 mm) was programmed. There was no rotation involved in this square, just simple forward, backward, and strafing motions. The square was programmed so that each segment could be analyzed for deviation from a straight-line path to find the worst-case scenario. Figure 2-7 shows the movement of the robotic platform throughout the square program.

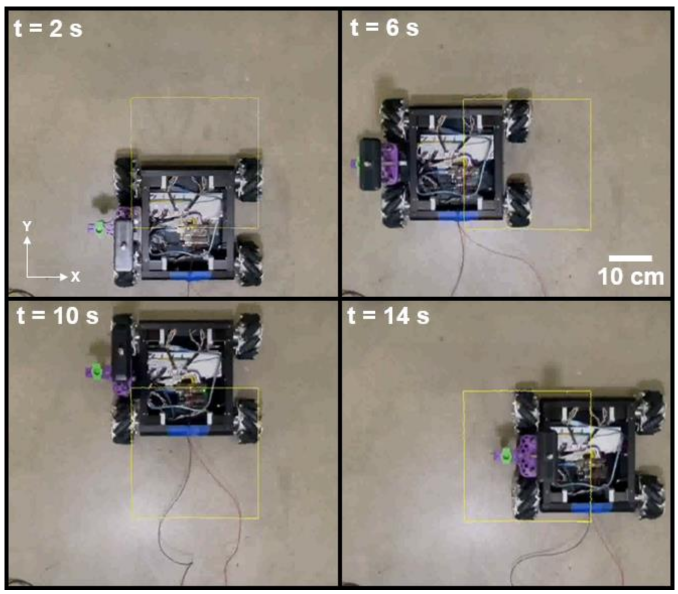

Figure 2-7: Square program broken into time steps for clarity.

It was important for this program to demonstrate motion in different directions to see which direction provided the worst case in terms of locomotion. The individual segments of the print path shown visually above are tabulated in Table 2-3:

Table 2-3: Robot motion as it relates to a Cartesian coordinate system.

Program Segment	
Segment	Motion
Segment One	-X Strafing Motion
Segment Two	+Y Forward Motion
Segment Three	+X Strafing Motion
Segment Four	-Y Backwards Motion

At this point, the programming was simplistic and used for loops to step each motor one after another in a rapid pattern. The important programming parameters for this experiment can be seen in Table 2-4.

Table 2-4: Important Programming Parameters

Program Parameters		
Variable	Value	Units
Print Speed	200	steps.s^{-1}
	77	mm.s^{-1}
Micro Stepping Resolution	1	step.revolution
Segment Length	3000	steps
	350	mm

This analysis was performed using Tracker video analysis software and an iPhone 12. A tripod was set up to position the iPhone 12 directly above the programmed square motion. The yellow LED on the Arduino UNO was traced throughout the motion of the programmed square. The following graph in Figure 2-8 shows each segment plotted on a cartesian coordinate system as well as the deviation from a straight line associated with each segment.

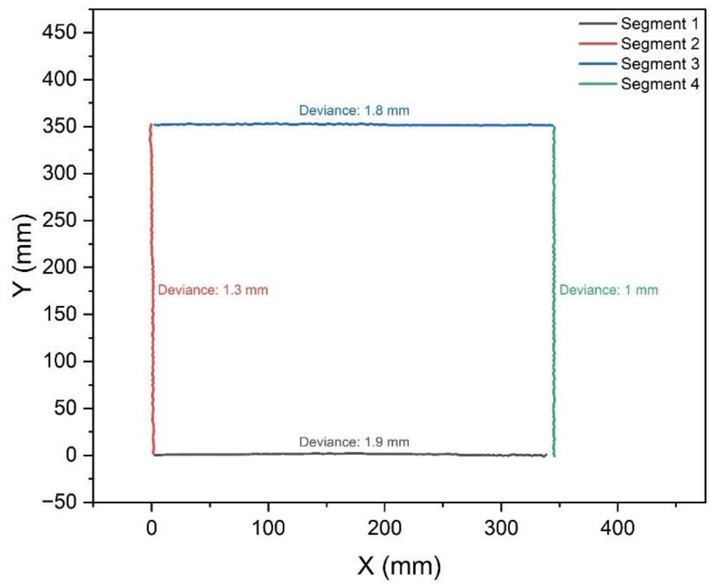

Figure 2-8: Deviation of robot motion from straight line at each line segment.

This test was the first time motion was demonstrated by the MRP and it aimed to set a baseline for motion analysis. The XY points from the traced LED were exported and analyzed. It was determined that the platform was accurate down to ± 1.8 mm during strafing motion and ± 1 mm during forward/ backward motion. It should be noted that there is a large amount of uncertainty in this experiment that could have an impact on the tolerance range listed above. There are potential uncertainties associated with the resolution, lens distortion, point tracking, and calibration scale. More robust methods were implemented in later experiments, but this helped to initially validate that this platform was capable of basic 3D printing.

2.2.3 Informal, Exploratory Testing

Visual Observations of Printed Structures

With the basic motion of the platform observed and validated, experiments were conducted to assess the effectiveness of the platform when used for additive manufacturing. At this point in the design, peanut butter was used to test printing systems because of its similar rheological properties to printable composite ink. In this experiment, a 300 mm long, two-layer line was programmed as seen in Figure 2-9.

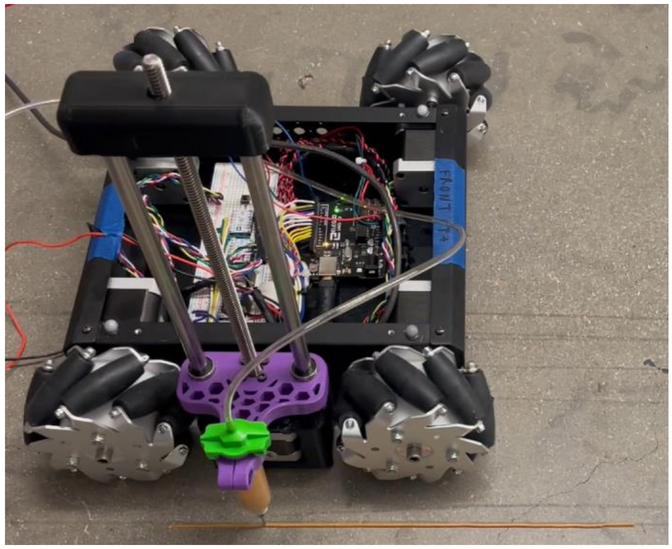

Figure 2-9: First demonstration of 3D printing with mobile platform using peanut butter.

The programming parameters were set as seen in Table 2-5.

Table 2-5: Programming parameters for first printing demonstration.

Program Parameters		
Variable	Value	Units
Print Speed	100	$steps.s^{-1}$
	38	$mm.s^{-1}$
Micro Stepping Resolution	1	step.revolution
Layer Length	3000	steps
	350	mm

Printing this structure helped to highlight several issues with the platform. First off, there were issues with inconsistency in motion and layer mismatch could be observed due to one of the stepper motors acting irregularly. This layer mismatch can be seen in Figure 2-10.

Upon further inspection, it appeared that some of the circuit components melted over time and were causing issues with robot locomotion. As a result, a second design iteration was proposed to fix these issues.

Figure 2-10: Close up of peanut butter print that showcases the layer mismatch from melted circuitry.

2.3 Design Iteration Two: Improving Circuitry for Durability

2.3.1 Design Work

Based on electrical issues encountered in the first design iteration, this second design iteration focuses on improving the quality and durability of the circuitry of the mobile platform. Initially, a plastic, breadboard circuit was used due to frequent circuit modifications and tuning. This plastic circuit was by no means robust but provided an initial stepping stone to the final circuit. To increase the quality of the circuitry, a soldered circuit was proposed. Not only does this circuit have superior electrical connections, but it greatly reduces the footprint of the electronics as seen in Figure 2-11.

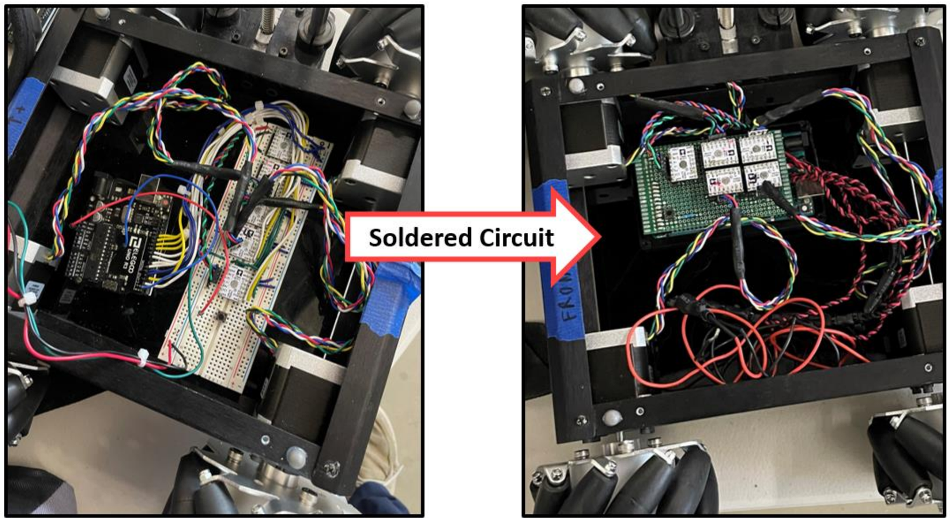

Figure 2-11: Reconstruction of circuit to alleviate issues stemming from melted components.

At this point, no major changes were made to the fundamentals of the circuit developed in design iteration one. Everything is the same, as there are still just five stepper motors and their associated drivers. A few minor changes were made such as the incorporation of an Arduino Mega instead of an Arduino Uno and the incorporation of a start button. The change in the microcontroller was based on the foresight that more digital pins would be required as the complexity of the robotic platform increased.

2.3.2 Experimentation

With the second design iteration of the mobile platform assembled, some validation experiments were run to determine if the updated circuitry performed better than the original. Methods for validation were improved at this point as well. Due to inconsistencies and potential inaccuracies in using Tracker software for motion analysis, a more robust experiment was designed using a three-camera, Opti-Track motion analysis system. This system operates by tracking reflective markers placed on the robot, which is accurate down to ± 0.2 mm.

Platform Validation

Instead of performing an analysis of a straight-line motion like the last validation experiment, this experiment focused on the ability of the mobile platform to print a 300 mm square. The printing speed and micro step resolution remained the same as the previous validation experiment. Nominal and experimental values were compared, and deviation from nominal was calculated. A more accurate baseline of the platform motion is shown in Figure 2-12.

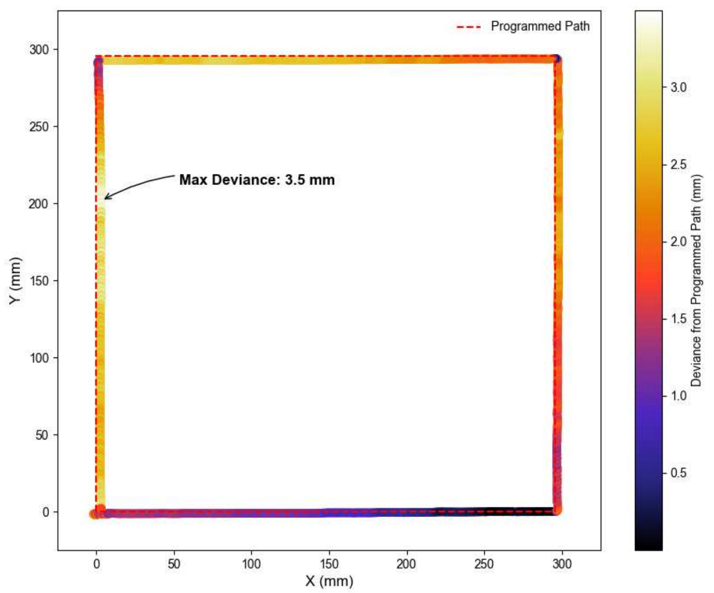

Figure 2-12: Motion analysis with full step resolution, using Opti-Track motion analysis system.

Effect of Micro Stepping on Path Trajectory

With a more accurate measurement system in mind and a baseline, further experiments were conducted to analyze the effect of micro-stepping resolution on the platform motion. It was predicted there would be a sweet spot between torque and accuracy. Very fine micro step resolution would not generate enough torque for accurate locomotion, whereas a course micro step resolution would cause the surface quality of the printed parts to be subpar due to the choppy motion of the platform. It should be noted that as the resolution of each step increases, the torque decreases.

To test this hypothesis and determine the optimum micro step resolution setting, the same 300 mm square was programmed, and the only variable that changed throughout the experiment was the micro step resolution. The chosen stepper motor drivers are capable of producing a micro-step resolution down to 1/32 step. This means that instead of having 200 steps per revolution of the platform wheel, there are now 6400 steps per revolution. Such fine micro stepping this fine provides much smoother rotation of the wheel as well.

The motion of the robot throughout the experiment was tracked and plotted against a nominal square as depicted in Figure 2-13.

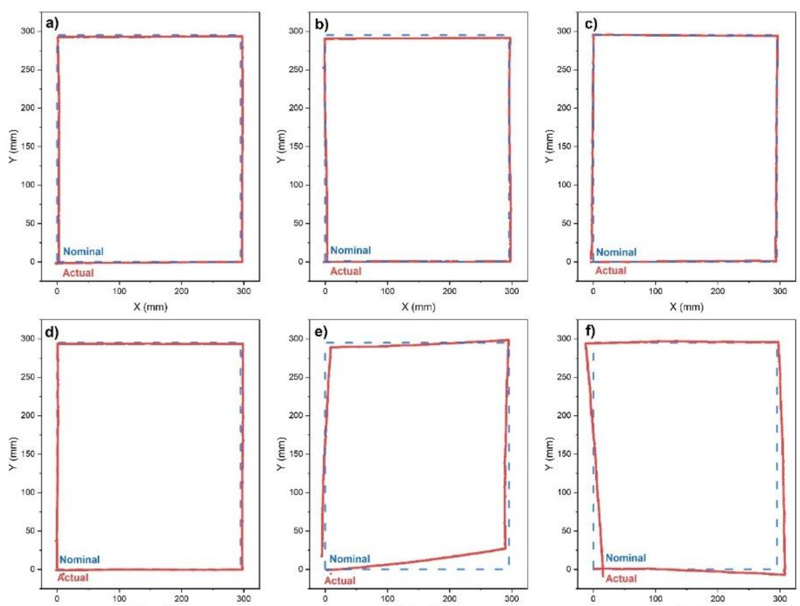

Figure 2-13: Graphs comparing nominal versus actual platform motion for a) full-step, b) half-step, c) 1/4 step, d) 1/8 step, e) 1/16 step, f) 1/32 step resolution.

At 1/16 step and 1/32 step, the robot demonstrates irregular movement as there is not enough torque to complete the square program in an accurate fashion (Figure 2-13). Visually, full-step, half-step, ¼ step, and 1/8 step appear similar, but the data was analyzed and compared to the nominal square. The best case ended up being the ¼ step resolution as seen in Figure 2-14.

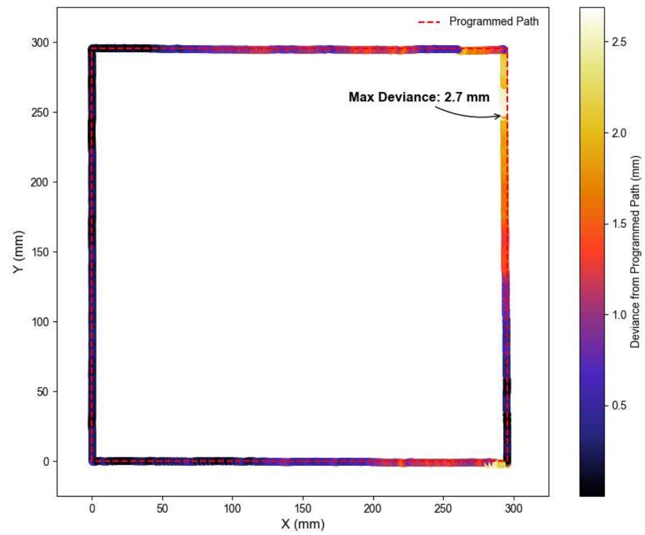

Figure 2-14: Best case scenario using 1/4 micro stepping.

The max deviation from the programmed path throughout the program was 2.7 mm from nominal. For smaller, fine prints this may not be precise enough, but for large, geometrically unconstrained prints, this max deviation value is acceptable. The 1/16 micro step resolution deviation analysis for best case and worst case comparisons can be seen in Figure 2-15.

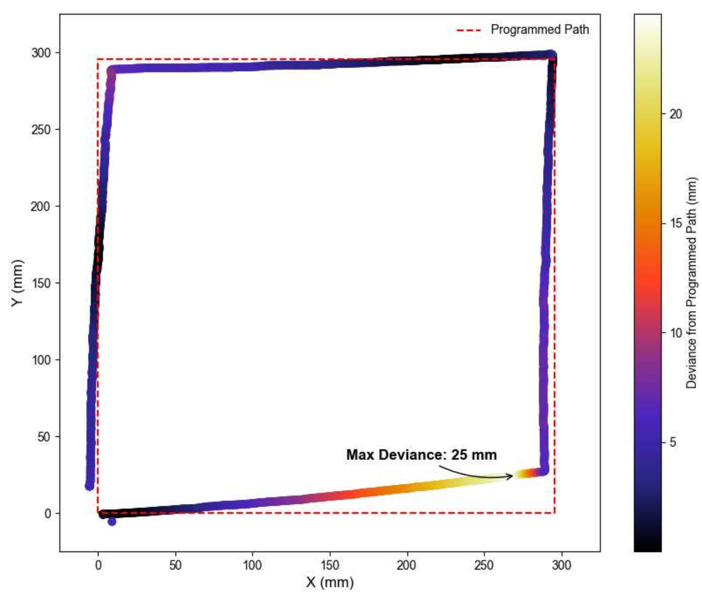

Figure 2-15: Worst case scenario using 1/16 micro stepping.

It can be seen in Figure 2-15, that the actual square was 25 mm out from nominal and the path did not close over the course of the print. This proves to be a problem, especially when considering multi-layered prints. Based on the results of this data analysis, ¼ stepping is the default processing parameter from this point forward. Additionally, this platform validation helped to showcase the durability of the soldered circuit as there were no melted components over the course of the experiments.

2.3.3 Exploratory Testing

Visual Observations of Printed Structures

With the platform motion evaluated and validated, another attempt at printing a peanut butter structure was performed. The same two-layer, 300 mm long print was programmed as before with no issues in stepper motors acting erratically. As a result, the layer count was modified in an attempt to magnify any faults in the robot locomotion. A three-layer, 300 mm long print was programmed using the same parameters as before, except now with ¼ micro step resolution. No erratic motion was observed over the duration of this more complex print as seen below in Figure 2-16.

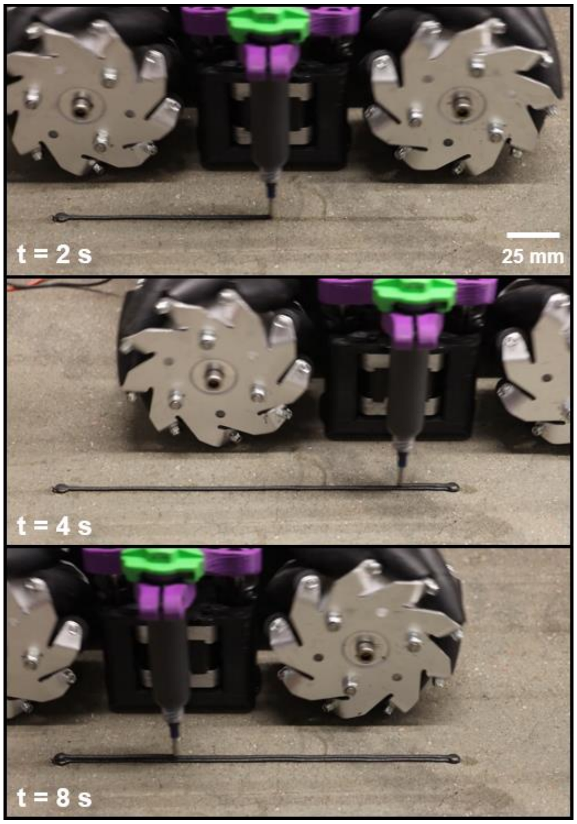

Figure 2-16: Three-layer, peanut butter printed structure to showcase platform improvements. Carbon black was added to the peanut butter to improve the color.

To further magnify any imperfections in the printing process, the print length was increased from 300 mm to one meter. Similar results in terms of layer stacking were observed throughout the print (Figure 2-17).

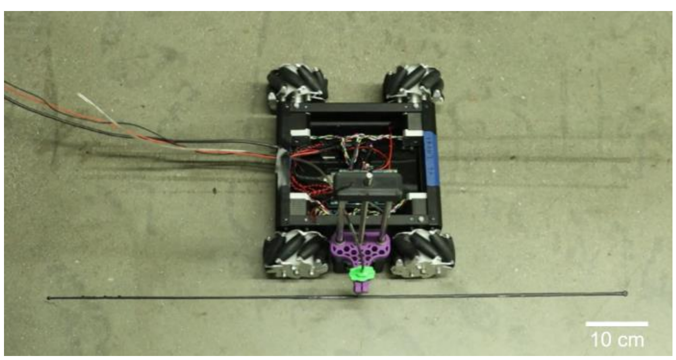

Figure 2-17: One-meter long, three-layer peanut butter print to evaluate system functionality.

While these tests did prove that the platform was capable of printing multiple layers with accuracy, they did help to highlight some of the issues with the system. First, the width of the print was not very consistent throughout the course of the print. The less peanut butter in the syringe, the wider the road width. In addition, the beginning and end of the prints were inconsistent in terms of road width. The beginning and end of the roads are wider and out of shape compared to the rest of the road. This stems from the use of pneumatic printing where it is much more difficult to control the flow rate of the material.

2.4 Design Iteration Three: Thermal Stimulus Incorporation

2.4.1 Design Work: Laser Incorporation

With the mobile platform at a point where additive manufacturing was repeatable, it was deemed necessary to begin the design work to incorporate a thermal stimulus for frontal polymerization. At this point in the design, there was no need for complex printing, so a simple one-directional heating system would prove adequate. In order to meet the size and weight limitations of the platform, an inexpensive, low-power red laser diode (200-250 mW, 650 nm) was chosen (Figure 2-18). At this point, only blue lasers had been used to initiate a front, so it was uncertain whether or not a red laser would have enough power to do so.

Figure 2-18: A low-power, 650 nm laser diode is used to initiate front for frontal polymerization [55].

In order to proceed with testing, a simple mount was designed to attach the laser to the mobile platform. The following, easily adjustable mount was designed and attached to the mobile platform (Figure 2-19).

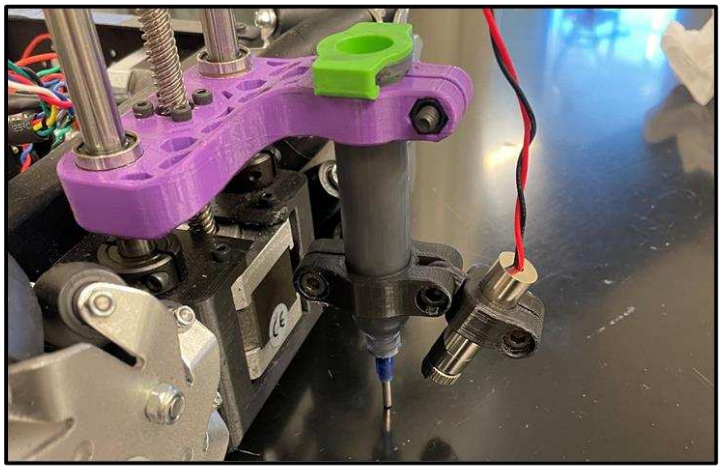

Figure 2-19: Simple, easily adjustable laser mount.

2.4.2 Experimentation

Basic Ink Formulation

In order to test front initiation using a red laser, a baseline resin system had to be created. This was done based on the work done by Ziaee et al. [10]. The following procedure and equations were used for a mixture of resin, carbon black, and fumed silica:

Table 2-6: Basic components used in resin system.

Ink Formulation		
Component	*Measurement*	*wt%*
Materia Proxima® HPR 2102 Polydicyclopentadiene (pDCPD) resin	18.28 g	89.1
Grubbs second generation catalyst (GC2)	11.72 mg	
Phenyl cyclohexane (PCH) solvent	1.0 mg	
Tributyl phosphite (TBP) inhibitor	7.2 µL	
TS-530 fumed silica (FS)	2.15 g	10.4
Carbon Black (CB)	0.093 g	0.4

The resin system seen in Table 2-6 was prepared according to the following procedure in Table 2-7, which remains consistent for all resin mixing unless otherwise specified.

Table 2-7: Baseline mixing formula for all resin.

Standard Resin Mixing Procedure	
1	Weigh out GC2 in mg using small plastic vial.
2	Pipette PCH solvent into a different plastic vial.
3	Micro syringe pipette TBP inhibitor into PCH.
4	Tap PCH/ TBP plastic vial for 1 minute.
5	Pipette PCH/ TBP into GC2 vial.
6	Sonicate PCH/ TBP plastic vial for 10-20 minutes.
7	Weigh out additives.
8	Weigh out pDCPD.
9	Mix additives into resin by hand until mostly homogenous.
10	Centrifuge mix resin mixture for 1 minute.
11	Pipette GC2/ PCH/ TBP solution into resin mixture.
12	Centrifuge mix everything for 1 minute.

To determine how much of each constituent is needed for the mixture, the following equations derived from the work done by Ziaee et al. [10] can be used where W_{GC2} is the weight of GC2 in mg, W_{DCPD} is the weight of the pDCPD resin in g, V_{TBP_MOLAR} is the volume of TBP needed for 1 molar equivalent with respect to GC2 in µL, and V_{PCH} is the volume of PCH in µL:

$$W_{GC2} = 0.642 * W_{DCPD} \tag{3}$$

$$V_{TBP\_MOLAR} = 0.309 * W_{GC2} \tag{4}$$

$$V_{PCH} = 85.324 * W_{GC2} \tag{5}$$

This baseline resin system is mixed up as described, and then transferred to a glass slide. The laser spot size was adjusted using calipers so that it was 2.3 mm in diameter, the same size as the intended road width of the printed parts. The laser was aimed onto the ink, and a front was successfully initiated. This was mostly due to the presence of the thermally conductive carbon black in the ink. The carbon black helped to convert the laser energy to heat and conduct it to the surrounding material to kick off the exothermic reaction of frontal polymerization. While simple, this experiment validated that the resin system could be cured using a low-power, red laser.

The last step before attempting to print with the resin system was to tune the resin viscosity. Without additives or gelling, the resin system was not viscous enough for printing. The two options to increase resin viscosity were to use additives, such as fumed silica, or to use an oven to partially cure and gel the resin. For this project, additives were used to simplify the ink preparation process. In order to determine how much fumed silica was necessary, trial and error experimentation was performed to establish the correct viscosity for printing. If the resin had a low viscosity, the printed structure did not hold its form well enough prior to cure for high-fidelity printing. If the resin was too viscous, the print surface quality suffered, and the mixture was difficult to print with.

Laser Quantification and Analysis

Once the basic rheologic properties and curing feasibility were established, the laser power density needed to be quantified for consistency. A Thorlabs PM100 Power and Energy Meter was used to measure the average power of the laser as shown in Figure 2-20.

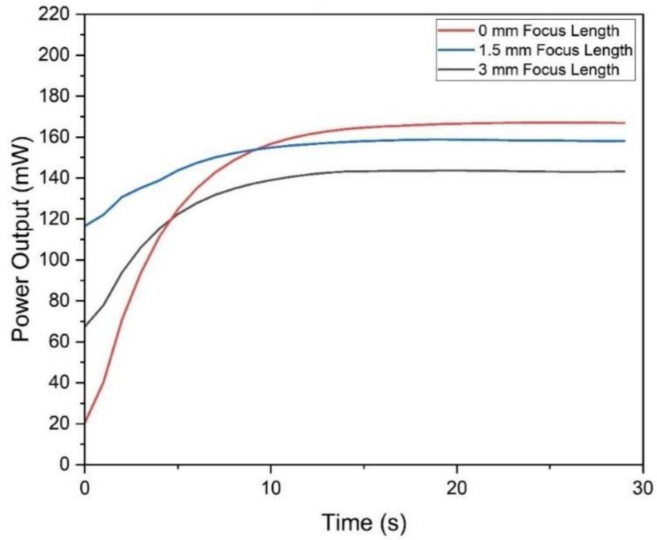

Figure 2-20: Average laser power of the low-power, red laser plotted with respect to time.

The different focus lengths are related to this specific laser where focus length, D_F, is the setting of the adjustable focus dial present on this laser model. It can be determined that while the average power varies slightly depending on the focus of the laser, it is within the range of approximately 140 – 160 mW with an average value of 156 mW. This average value is used from this point forward to establish the laser power density.

After determining the average power, power density was calculated based off on the distance from the substrate, focus length, and the spot size. Measurements of spot size (mm) and caliper focus length (mm) were taken at various distances from the substrate, including 400 mm, 200 mm, 100 mm, 50 mm, and 25.9 mm. The distance of 25.9 mm was the closest that the laser could be to the substrate and still produce a focused spot size. The spot sizes and focus length were measured using calipers. Linear regression was performed at each distance to approximate a linear relationship between the spot size and the caliper focus length. Next, the caliper focus length was fixed and the relationship between the distance from substrate and laser spot size was determined. Due to the nature of the data, three different spot sizes were chosen for consideration. The first, 0.3 mm, was chosen as this is the spot size when the laser is completely focused. Next, a spot size of 2.3 mm was chosen as this is the road width of the printed parts using a 12 gauge Fisnar blunt end dispensing tip (ID = 2.3 mm). Finally, the spot size of 0.8 was chosen as is 1/3 of the diameter of 2.3 mm and represents a scenario where there are three lasers shining on the printed road at the same time with no overlap.

One additional important consideration with the laser positioning is the angle of the laser with respect to the substrate. Due to the nature of the setup, it was impossible to position the laser completely vertical. To account for this limitation in the power density calculations, Equation 6 was derived where C_A is the cross sectional area of the laser beam, S is the spot size in mm, and θ is the angle with respect to vertical as schematically shown in Figure 2-21.

$$C_A = \frac{\pi S^2 \sec(\theta)}{4} \tag{6}$$

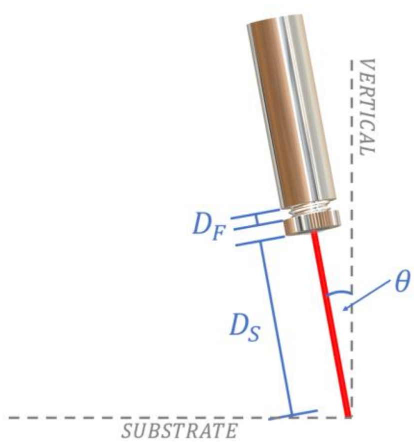

Figure 2-21: Schematic representation of variables that influence laser power density.

Using this equation, the cross sectional area of the laser beam can be calculated and used to quantify the power density of the laser beam depending on its distance from the substrate and the as seen in Figure 2-22.

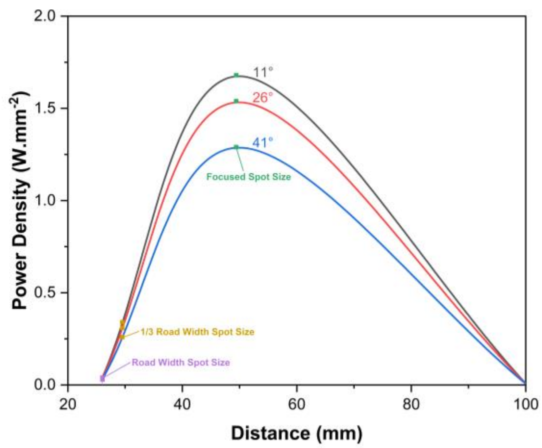

Figure 2-22: Relationship of the power density of the laser as a function of the distance from the substrate.

2.4.3 Exploratory Testing

<u>Freeform Print Demonstration</u>

A basic freeform print was demonstrated using the low-power red laser by continuously heating the printed material at the laser spot (Figure 2-23). This was the first demonstration of completely freeform printing using this MAM platform. Through trial and error, this printing demonstration helped to quantify important printing parameters such as print speed while curing.

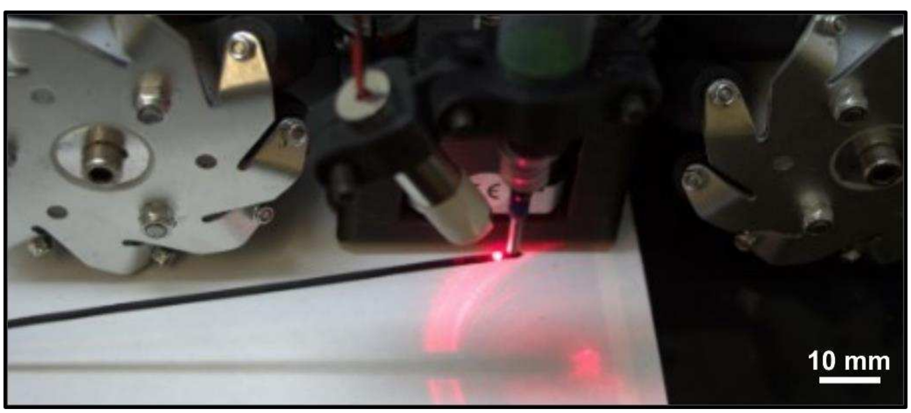

Figure 2-23: First demonstration of freeform printing using a low-power, red laser to cure the resin system.

While this print represents a large step forward in the research effort, it did help to highlight some limitations of the system. Primarily, the current laser apparatus only allows for printing in one direction. This severely limits the motion of the platform and defeats the purpose of the omnidirectional platform's capabilities. As a result, a new design iteration was proposed to eliminate this unnecessary constraint.

2.5 Design Iteration Four: Linear Actuator and Laser Rotation

Based on issues encountered when printing with pneumatics, a desire to operate untethered to power, and a desire to print in multiple directions, a new design iteration was proposed. This design iteration included the addition of a motor-drive extrusion system as well as a laser rotation system.

2.5.1 Design Work: Linear Actuator

As seen in Figure 2-24, this system uses the lead screw of a non-captive, NEMA 17 stepper motor as a piston to extrude the ink. Separate linear rod and linear bearing are used to inhibit rotation of the lead screw, allowing for smooth linear motion while extruding. This system prints based on speed, not force, so consistent extrusion can be achieved throughout the course of the print, despite viscosity change. This system allows for compact, reliable extrusion that can be easily controlled using an Arduino microcontroller.

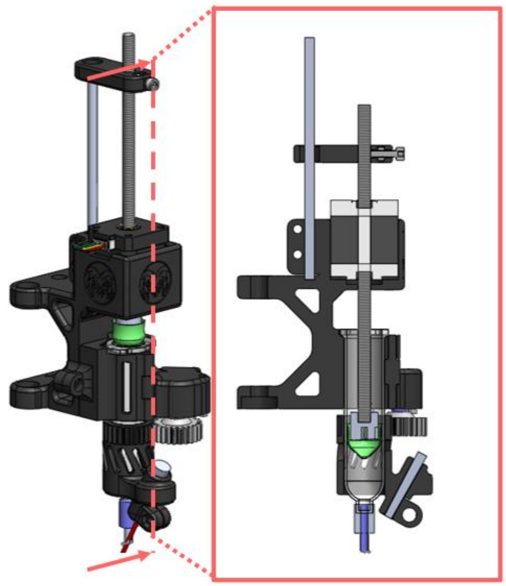

Figure 2-24: Cross sectional view of the linear actuator extrusions system.

In addition to improved print control, this extrusion system represents another step towards the goal of completely untethered platform operation. Previously, the mobile platform was tethered to the pneumatic dispensing unit, which significantly constrained the platform's motion significantly.

2.5.2 Design Work: Laser Rotation

Up to this point, a fixed, one directional laser proved to be enough for simple prints. To be able to print in any direction, it was necessary to incorporate a more robust system. In the first design iteration, this included a laser rotation system. The laser mounted similarly, but instead of being fixed, a gear was implemented to rotate the laser. Depending on direction of the robot motion, the laser would rotate to line up and always stay on the printed path. As there were no limit switches or home positions, it was necessary to manually align the laser at the beginning of each print. The laser rotation assembly can be seen in action in Figure 2-25.

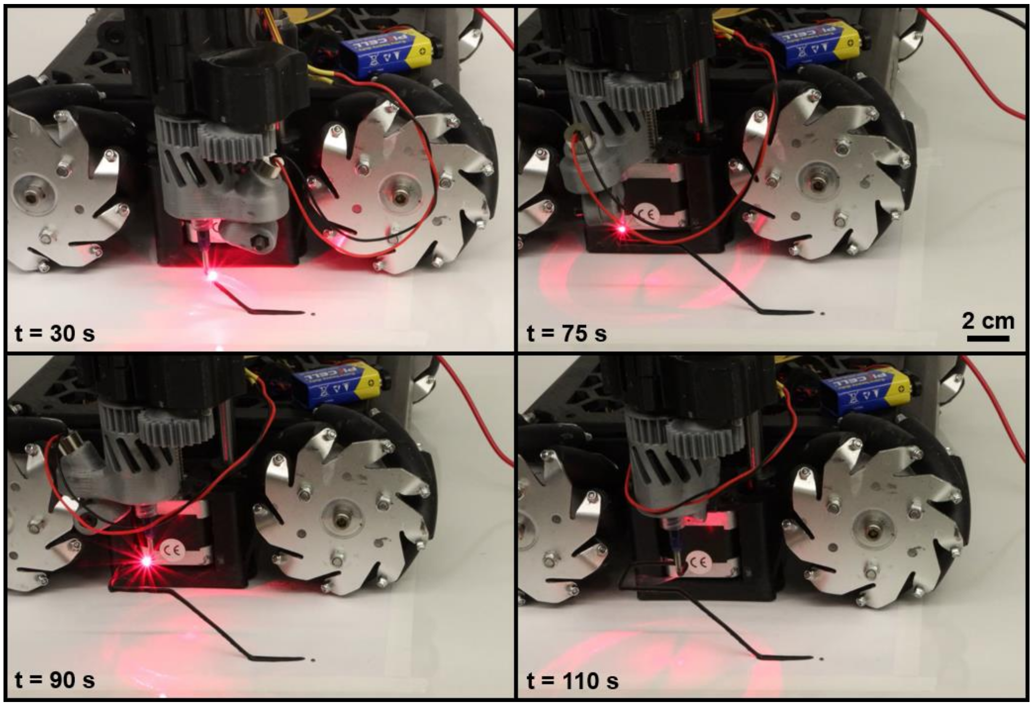

Figure 2-25: Free form print showcasing laser rotation to allow for omnidirectional printing.

This laser rotation system allowed for printing more complex geometries, such as the square bracket in Figure 2-25 and the zig-zag brackets in Figure 2-26.

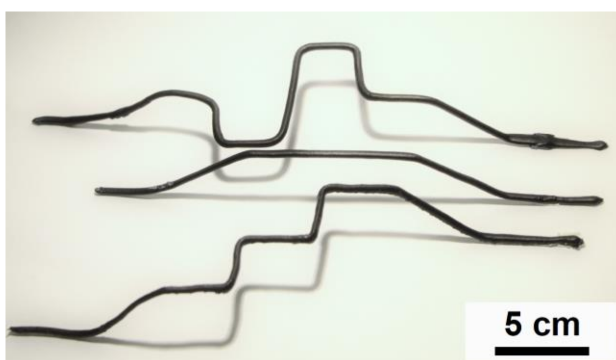

Figure 2-26: Freeform brackets printed using laser rotation system.

Despite the newly found geometrical freedom, issues were still present with this laser rotation system. Due to the lack of a homing mechanism, the laser had to be lined up perfectly before every print. This was especially difficult due to the presence of backlash within the rotational gear system. Additionally, in order to power the laser, wires needed to be run from the mobile platform to the laser. When the laser rotated, the wires were in danger of getting caught in the rotating gear system. To address this, a slip ring concept was introduced, however, commercially available slip rings were expensive and did not fit within the geometrical design envelope required by the system. The rotational laser system worked, but another design iteration was necessary to improve the overall quality and geometrical freedom of the system.

2.5.3 Design Work: XY Coordinate Programming

In order to get the full advantage of omnidirectional printing with the laser rotation, it was necessary to change the way the platform is coded. Up to this point, the platform was hard coded with forward, backwards, sideways, etc. functions. This was inefficient from a coding standpoint and did not allow for much flexibility in terms of printing ability. As a result, the platform was recoded to a custom g-code configuration. This custom g-code operates off of cylindrical coordinates to allow for the laser to rotate properly. When the user inputs a set of XY coordinates into the program, the radial distance and azimuthal angle between the points is calculated. The robot adjusts the speed of each wheel accordingly to produce a force vector in that direction and the laser rotates to line up directly behind the needle as it moves in that direction. This coding change allowed for more freedom in part complexity and represented a significant step forward in platform capability.

2.5.4 Design Work: Battery Incorporation

Another major update at this time was the addition of a battery for untethered platform operation. Up to this point, a power supply was used to provide the necessary power for printing. This required the platform to be tied to a power source, which was a disadvantage in terms of part size capabilities. It was challenging to find a cheap and reliable battery that was small enough to not affect the motion of the platform. Additionally, at full operation, the seven different stepper motors require about 20 volts and 6 amps.

It was important to find an inexpensive, reliable battery that could print for over 30 minutes without needing to be swapped. Several lithium-ion polymer batteries were tested, but none could fit easily on the platform and had enough battery capacity to print for over 30 minutes. As a result, a DeWalt 5 Ah, 20V drill battery was sourced for about $70. A custom 3D printed bracket allows for the battery to slide into place easily and two modified spade connections tap into the positive and negative lugs of the battery. This battery allows for printing of up to 45 minutes, which is longer than the pot life of the resin. Once the battery has been used, it can be easily swapped and charged for an extended print time.

The addition of this battery allows for unlimited part size in the XY plane and increased print complexity accordingly. At this point in the design stage, the mobile platform appeared as seen in Figure 2-27. An example of untethered operation in a demo programmed for showcasing the robot at Engineering Days 2023 can be seen in Figure 2-27 as well.

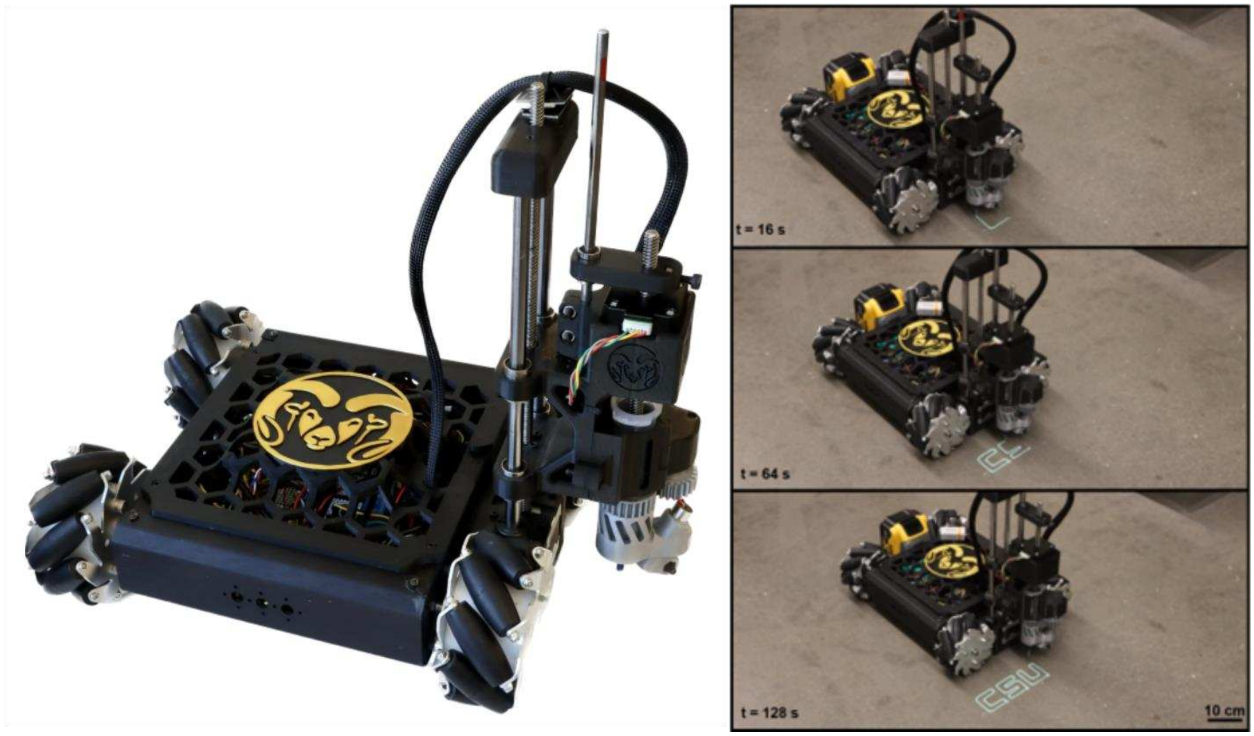

Figure 2-27: The assembled mobile platform at this stage in the research (left) and an example of untethered printing using toothpaste as a demo (right).

2.5.5 Experimentation

This platform was at a point where it could repeatably print using the thermally responsive resin system developed previously. In order to test the effectiveness of printing, a series of experiments were considered.

Measurement of Degree of Cure

While the resin appeared to be fully cured, differential scanning calorimetry (DSC) experiments were performed to further quantify the degree of cure of printed parts. Samples were printed on a glass slide and cut into specimens containing 5-10 mg of resin. The results of representative DSC experiments are shown in Figure 2-28 and Figure 2-29.

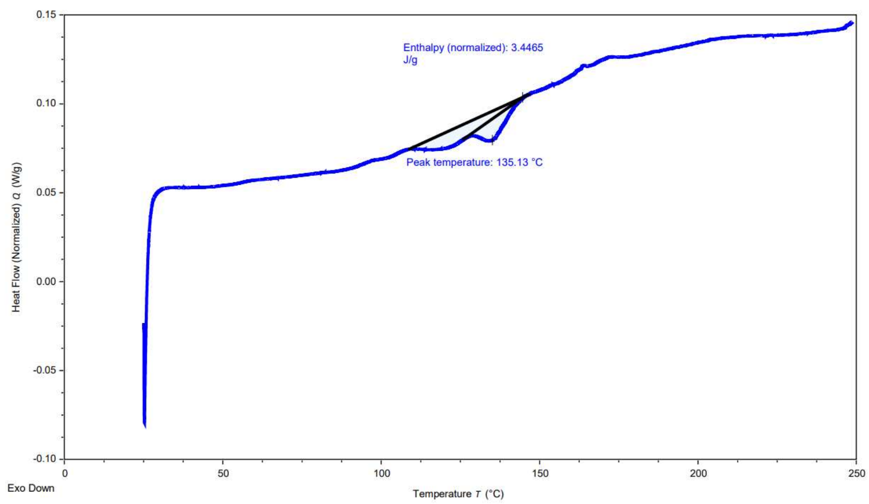

Figure 2-28: DSC profile on a printed specimen for measuring the residual heat of reaction, H_R.

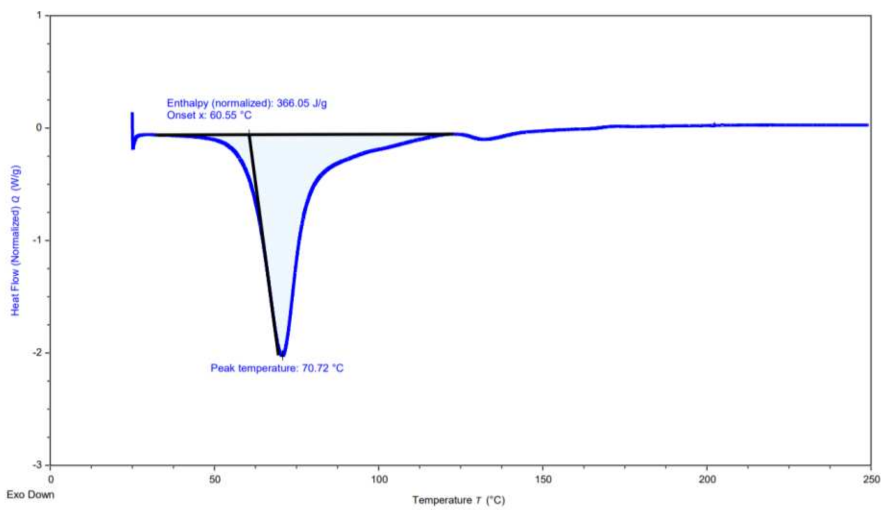

Figure 2-29: DSC profile on uncured ink for determining the total heat of reaction, H_T.

The degree of cure, α, is calculated using Equation 7, where H_T is the total heat of reaction, and H_R is the residual heat of reaction.

$$\alpha = 1 - \frac{H_R}{H_T} \tag{7}$$

Using this equation, the degree of cure of the printed part can be estimated to be 99.1%.

Microscopy

Digital microscopy was used to determine the void content and fidelity of the printed parts. Microscopy samples were prepared by cutting and polishing freeform, printed samples. The cross sectional micrograph in Figure 2-30 shows the circular print geometry as well as low void content in the printed part.

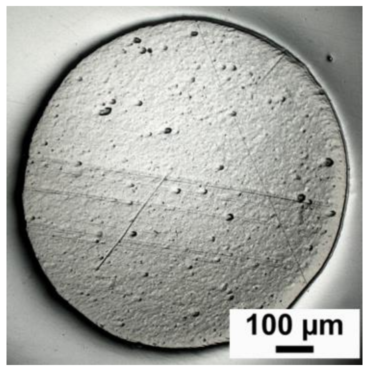

Figure 2-30: Cross-sectional micrograph of the printed part showcasing highly circular geometry.

Using color filtering techniques on the digital microscope, a low void content was calculated. The void content was calculated to be 1.9%, but there is some inherent uncertainty associated with this calculation, it is directly related to the algorithm used within the digital microscope software. Regardless, there are no large voids within the print and void content can be classified as being relatively low.

Low-Warpage Ink Formulation

During some of the high-aspect ratio prints on cold surfaces, warpage was observed, likely due to a large thermal gradient between the ink and the cold surface. To mitigate the effect of warpage, milled carbon fibers were introduced to the ink mixture to provide more rigidity. The fibers listed in Table 2-8 were tested for their printability and warpage mitigation.

Table 2-8: Outline of fiber lengths tested for optimal printing [56].

Fiber Type	Fiber Length (µm)
Asbury 95MF0400	400
Asbury 95MF0200	200
Asbury 95MF0800	800

To assess the printability and warpage reduction, a 5 layer, 15 cm long straight print geometry was printed 20°C concrete at 20 °C. This print geometry was chosen to exaggerate the warpage as most mixtures did not warp with just a single layer.

Table 2-9: Fiber mixtures sorted from best case to worst case in terms of printability and warpage optimization.

Printability	**Fiber Length (µm)**	**wt% Milled Fiber**	**Observations**
Best Case	200	7.1	Minimal warp, good print quality.
	200	4.4	Minimal warp, good print quality.
	400	7.1	Minimal warp, poor print quality.
	800	1.7	Poor print quality, extrusion issues.
	400	10.9	Bad warpage.
	800	4.4	Clogged needle.
Worst Case	800	14.0	Clogged needle.

The best case fiber mixture in Table 2-9 was chosen and implemented from this point forward. It was noted that all prints had some warp, regardless of fiber content. It was concluded that if the fiber content was too high, clogs in the printing nozzle were frequent and front propagation was inconsistent. It was also observed throughout the process that increasing fiber content resulted in an increase in print speed.

For other measures taken to reduce warpage, it was observed that there were no noticeable differences in warpage when printing directly on a heated bed. It also appeared that there was no noticeable difference in warpage between no laser heating, pulsed laser heating, and constant laser heating. Additionally, it was observed that printing on polypropylene film and PLA helped to reduce warpage simply due to better surface adhesion than concrete with no adhesive. At this point, it should be acknowledged that there may have been some error introduced due to the viscosity differences of the mixtures. Fumed silica was used to tune the viscosity to a printable value but amounts differed depending on the print due to the way the different length fibers interacted with the resin mixture. The author acknowledges that the resin system could be further tuned with better practices for warpage optimization. Additionally, due to fiber availability later in the research, Zoltek PX35 fibers of length 150 μm were substituted instead of the 200 μm fibers. The new fibers printed the same, but this may influence the resulting warpage with this fiber system.

After the addition of milled fiber to the ink, further DSC tests were run to ensure proper degree of cure with the new materials. The results were comparable with an average degree of cure of 99.5%.

Rheological Profile

With the addition of milled fiber, a new rheological profile for the ink was established. A shear sweep test was run to quantify the shear thinning behavior of the ink. As seen in the plot A of Figure 2-31, the viscosity decreases when the shear rate increases, meaning that this ink exhibits shear thinning properties. As seen in the plots B and C of Figure 2-31, the complex viscosity, storage modulus, and loss modulus increase with time.

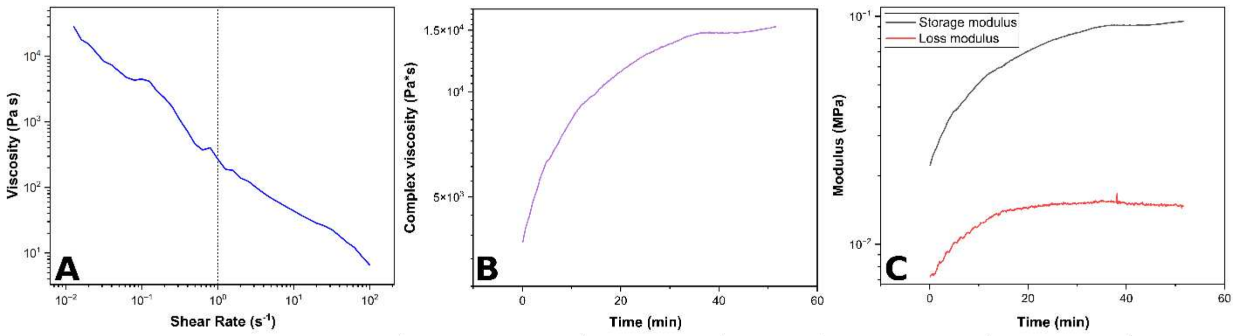

Figure 2-31: Rheological profile of the ink system used for printing where A) is the viscosity of the ink as a function of shear rate, B) is the complex viscosity as a function of time, and C) is both the storage modulus and the loss modulus as a function of time.

<u>Microscopy of Printed Samples Containing Fibers</u>

With the new fiber-reinforced resin system implemented, microscopy was conducted to ensure proper fiber alignment within printed specimens. As seen in Figure 2-32, high fiber alignment can be observed in addition to geometric fidelity. The darker grey is the matrix material and the lighter gray/white is the reinforcement material.

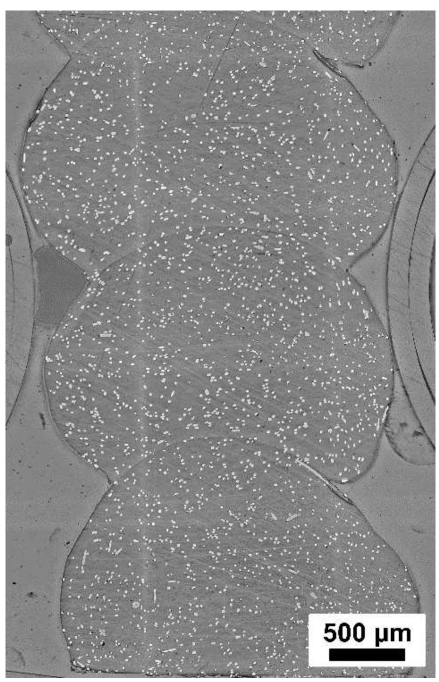

Figure 2-32: Cross-sectional micrograph of a multi-layer structure showcasing high fiber alignment.

2.6 Design Iteration Five: Modular Design

While the fourth design iteration addressed many of the issues present with the platform, a fifth design iteration was proposed to eliminate issues with the laser rotation system as well as to introduce more complexity in terms of sensor/ attachments to the system.

2.6.1 Design Work: Modular End Effector Capability

The rotating gear system worked well enough for simple prints, but lining the laser up properly was difficult, especially when considering increasing backlash over time due to the soft, 3D printed gears. As a result, the first change was the redesign of the rotational laser system. Instead of using one laser that rotates around the axis of the printing syringe, a new multi-laser system was proposed. While it may seem more complex to add multiple lasers to the system, the multiple laser approach was more repeatable. Instead of having to rotate a laser, an 8-channel relay was used to turn on and off lasers at specified angles. This allows for at least one laser to be in contact with the print at all times. To implement this, a modular design was proposed where the laser attachment system could be swapped in or out depending on the application. Over the course of this design iteration, five different designs were implemented to demonstrate the versatility of the platform.

<u>Simple Two-Laser Mount:</u>

The first implementation was a simple, two-laser mount for simple forward and backward prints. As seen in Figure 2-33, only two lasers are mounted which allows for a small end effector profile. Despite this space saving design, the platform is still fully capable of printing side-by-side prints as shown in Figure 2-33.

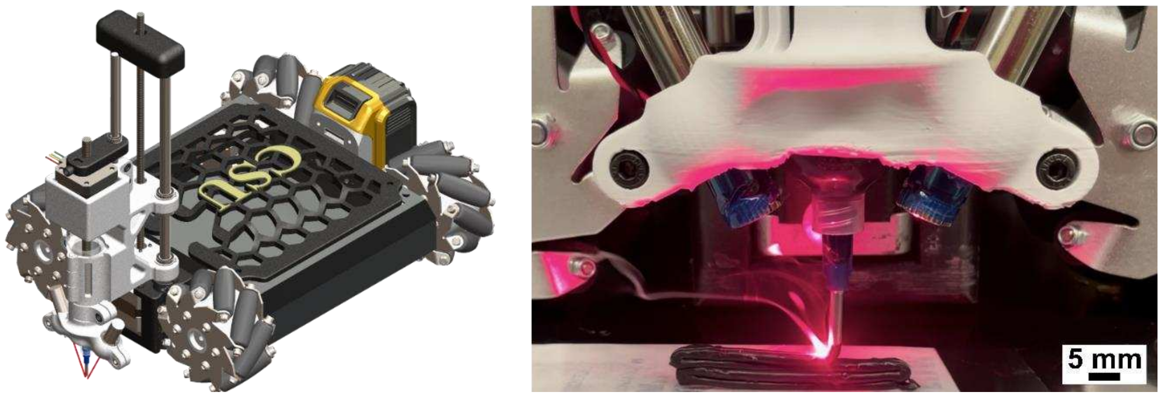

Figure 2-33: Rendered view of two laser system on the left, and on the right side is a shot of the system in action.

Eight-Laser Mount

The next design that was implemented was the eight-laser, omni-directional curing system. This design is a scaled up iteration of the two laser design. Depending on user input, one, two, or three lasers can be in contact with the deposited ink at all times to allow for increased print speed in all directions (Figure 2-34).

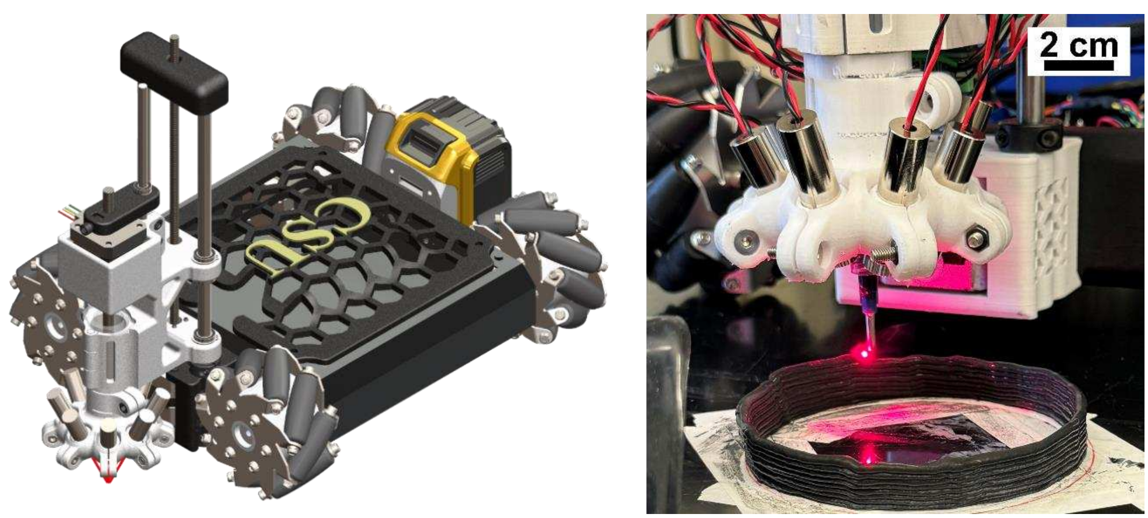

Figure 2-34: Rendered view of the eight laser system on the left, and on the right side the system being used for a multi-layer print

Distance Sensor Mount

In addition to the eight-laser mount, a distance sensor mount was designed to mount the end effector to incorporate a closed loop control system to control the end effector height. This implementation is especially useful in areas where the print surface is uneven, such as remote or hazardous areas. This implementation can be seen in Figure 2-35.

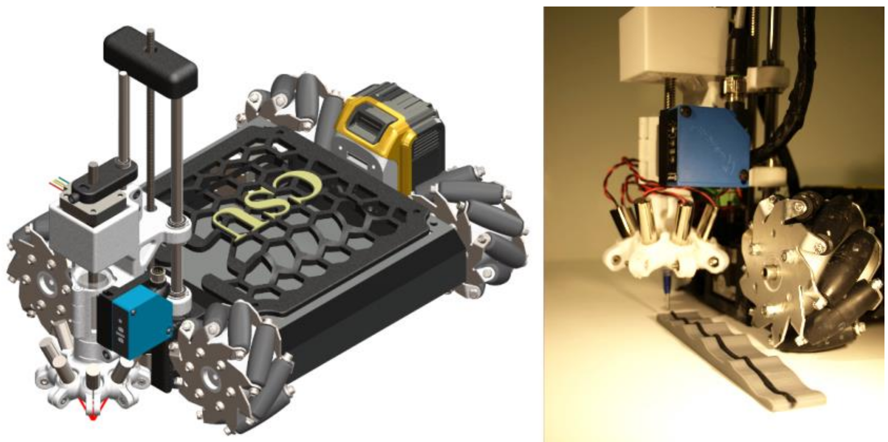

Figure 2-35: Rendered view of distance sensor attachment on the left side, and on the right side is an image showing the application of the sensor.

The distance sensor used in this application is a Wenglor OPT 2006 photoelectric with a resolution of less than 80 µm. An attempt was made to incorporate a less expensive distance sensor, but failed due to an inherent lack of precision. To program this distance sensor, the approach in Figure 2-36 was taken.

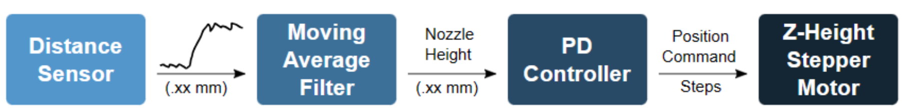

Figure 2-36: Diagram schematically representing the implementation of PID control.

The addition of this closed loop control led to a more robust system that was not limited to printing on perfectly flat surfaces. As seen in Figure 2-37, the mobile platform was capable at this point of keeping a consistent road height on uneven surfaces.

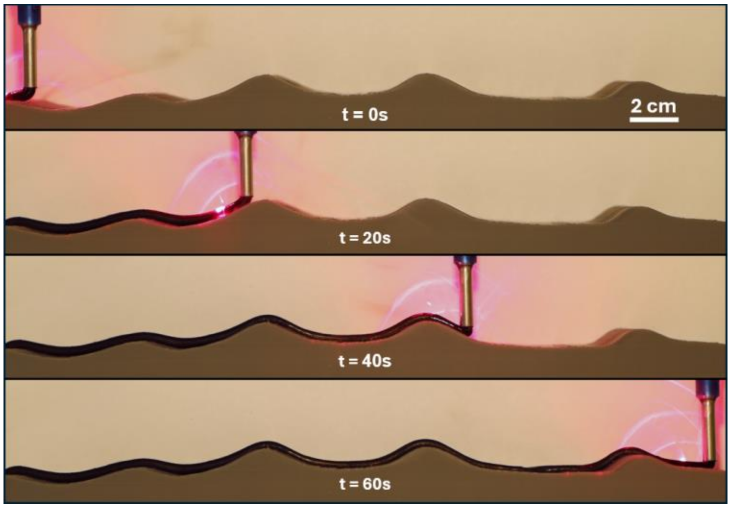

Figure 2-37: Frame by frame view of an empirical test of the distance sensor system.

<u>Upside Down Printing</u>

To further increase printing freedom, the print head of the robot can be flipped 180° to allow for upside down printing capabilities. Due to the unique nature of the resin system used, no support materials are required and upside down printing can be demonstrated (Figure 2-38).

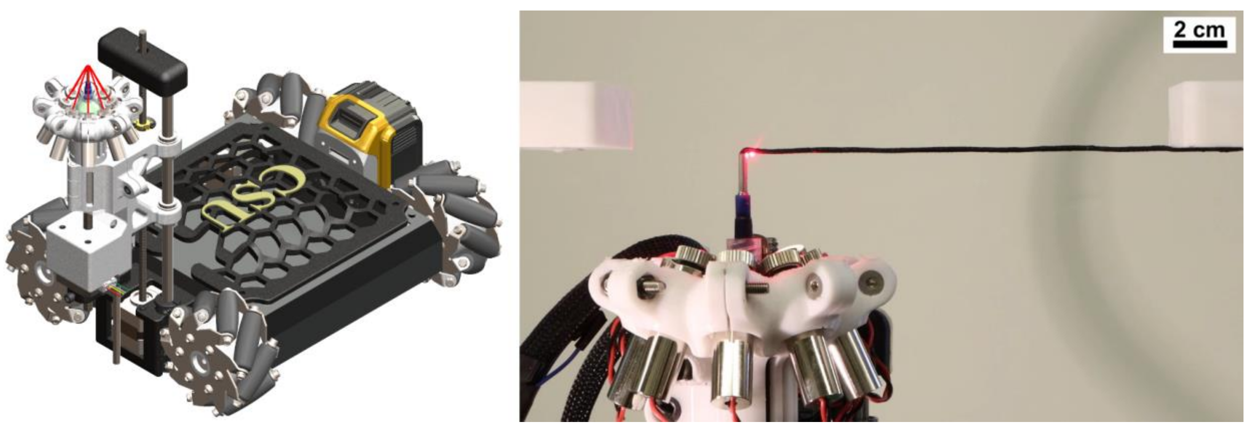

Figure 2-38: Rendered view of the upside down printing apparatus on the left side and a demonstration of the system on the right side..

Macro Camera Mount

The last modular design component that was demonstrated was the attachment of a camera to the system. This design still incorporated the use of a laser to cure the resin. As seen in Figure 2-39, the attachment of a camera allows for high-quality imaging of the print.

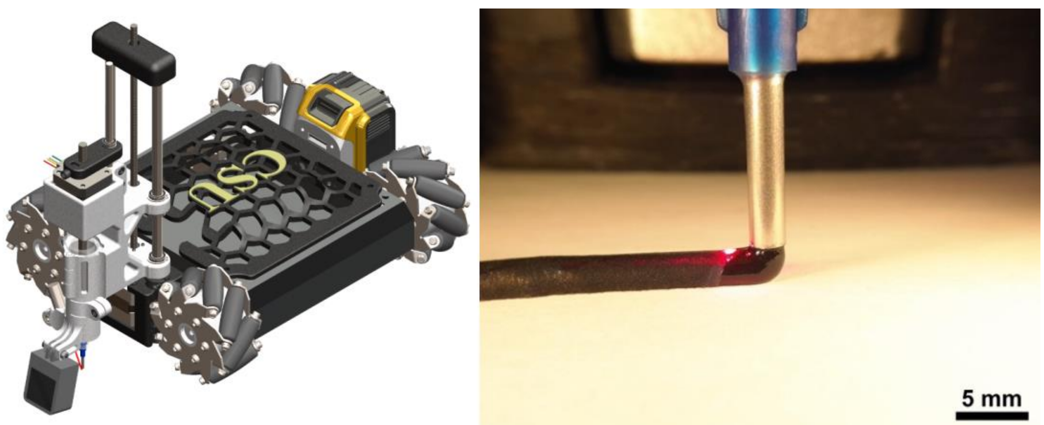

Figure 2-39: Rendered view of the camera attachment on the left, and on the right side is an image taken using the camera.

While this camera attachment is purely demonstrational in this research, there is potential for speed control using machine learning algorithms.

Final Platform Assembly

At this point in the research, the platform was fully developed and capable of untethered printing in multiple orientations with closed loop control. The current state of the circuitry can be seen in Figure 2-40.

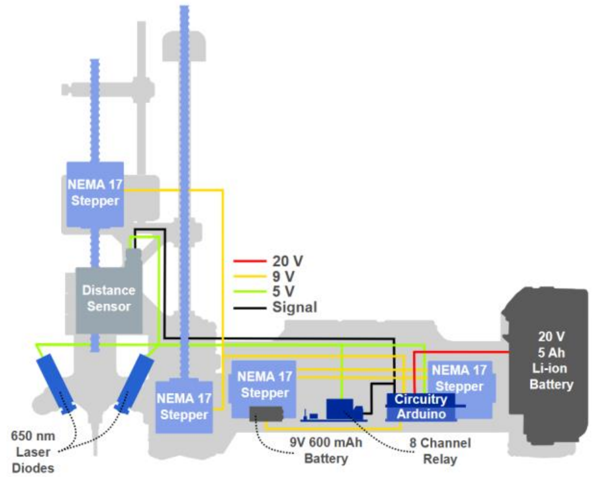

Figure 2-40: Schematic view of final state of the platform circuitry.

Figure 2-41 shows a demonstration of the final mobile platform assembly and the related components for the additive manufacturing of thermally responsive thermoset resins.

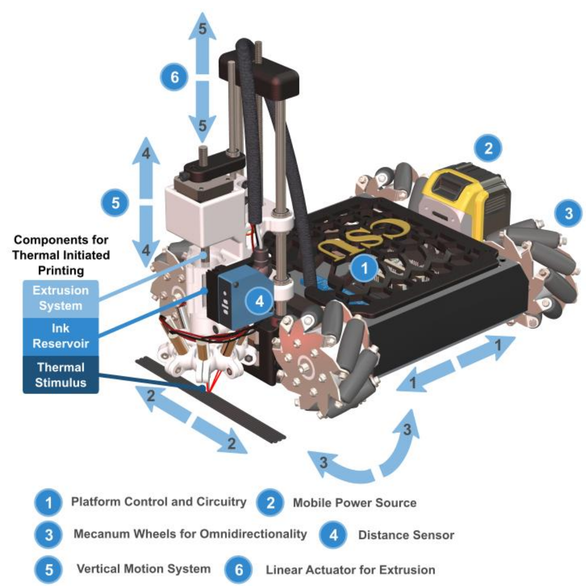

Figure 2-41: Rendering of the final platform state with annotations highlighting each system.

This platform is capable of printing geometries with any degree of overhang and with a footprint larger than the robot itself as shown in Figure 2-42 and Figure 2-43.

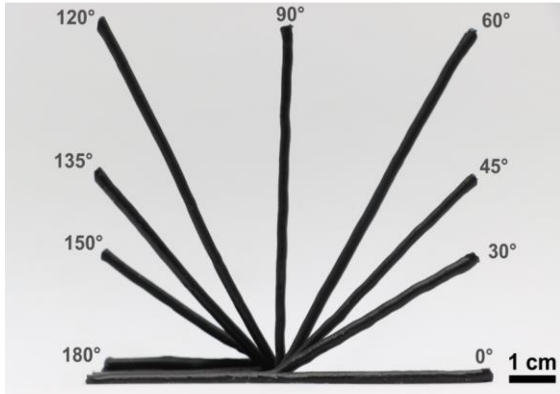

Figure 2-42: Side view of prints with various overhang angles.

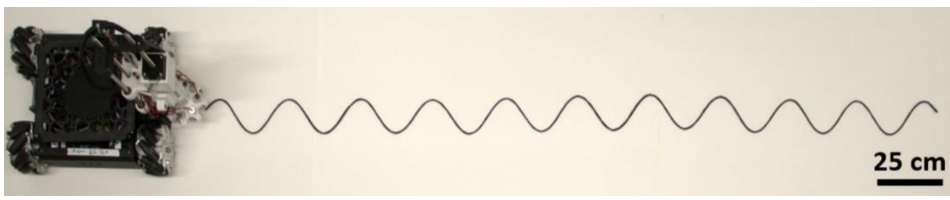

Figure 2-43: Top down view of a large, 2.5 m long print in the shape of a sin-wave.

The cost of the final platform with all of the necessary components comes out to approximately $650. This price does not include the distance sensor or the micro camera.

2.6.2 Experimentation

The fully functional platform was used to perform further experimentation to better understand the related printing parameters.

<u>Platform Validation</u>

Similar to prior experiments, platform validation was performed to ensure that the platform was robust and repeatable. For this experiment, a 15 layer, 100 mm circle was programmed to analyze the robot locomotion over the course of the printing process. A cylindrical object was chosen because it requires robot motion in all directions on the XY plane. This print was programmed at the print speed of 1.5 mm/s. The deviation from nominal was analyzed using the Opti Track motion tracking system. Three experiments were conducted, and the data was averaged and plotted as seen in Figure 2-44.

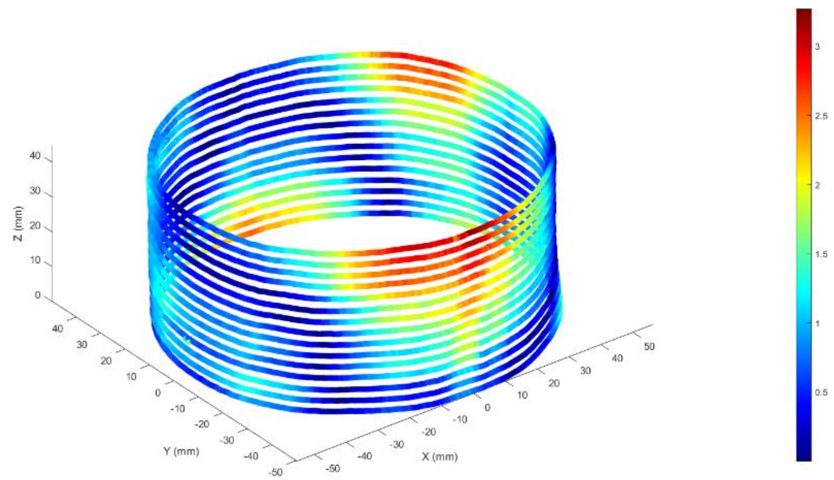

Figure 2-44: Average radial deviation of the platform movement over the course of a 15 layer print.

After data analysis, it was determined that the max deviation from nominal was just over 3 mm. The layer-by-layer deviations with respect to coordinate directions is shown in Figure 2-45.

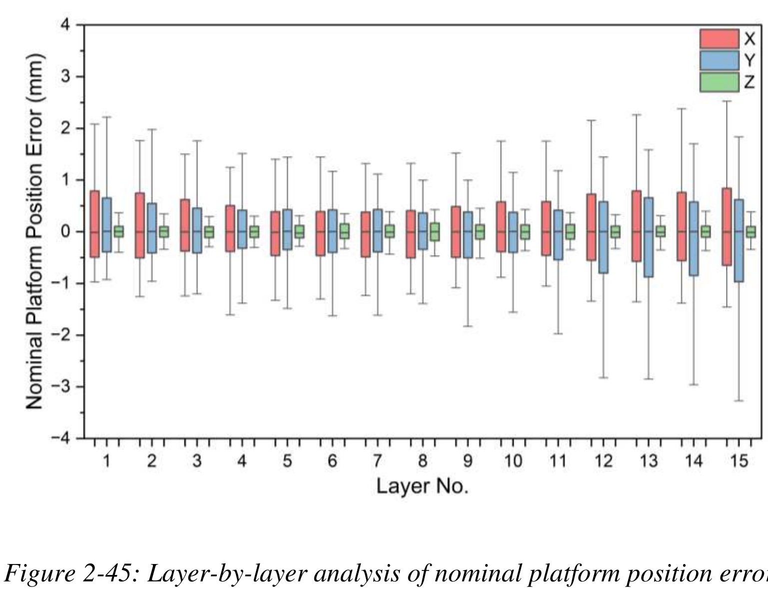

Figure 2-45: Layer-by-layer analysis of nominal platform position error.

For further demonstration, the same cylindrical geometry was printed. The printed part used the same program but only consisted of 10 layers (Figure 2-46).

Figure 2-46: A 100-mm diameter circle printed to better visualize the Opti Track experiment.

Due to the complexity of the program, this was the most extensive platform validation study performed over the course of the research. This experiment showed a maximum deviation of about 3 mm during the 15^{th} layer of printing. The z-deviation remained very consistent throughout the course of printing, and the x- and y-deviations remained very similar to each other representing no significant error when the platform is strafing. This experiment demonstrated the capabilities of the system in conducting prints with a large number of layers.

Effect of Micro Step Process Parameters on Path Trajectory

Because the platform weight distribution changed significantly throughout the project, it was necessary to retest the optimum micro stepping resolution to achieve the most accurate prints. To conduct this experiment, a 200 mm x 200 mm square was programmed at the print speed (1.5 mm/s). The only variable that changed throughout the course of the experiment was the micro-stepping resolution. Three trials per micro-step resolution were performed and averaged into representative datasets for each micro-step resolution. When the experiment was performed, full step and half step trials resulted in large amounts of error as seen in the overlay of Figure 2-47 and were excluded from the analysis. The average absolute deviation from a nominal square was calculated for each path. As seen in Figure 2-47, the optimum micro step resolution was 1/32 step.

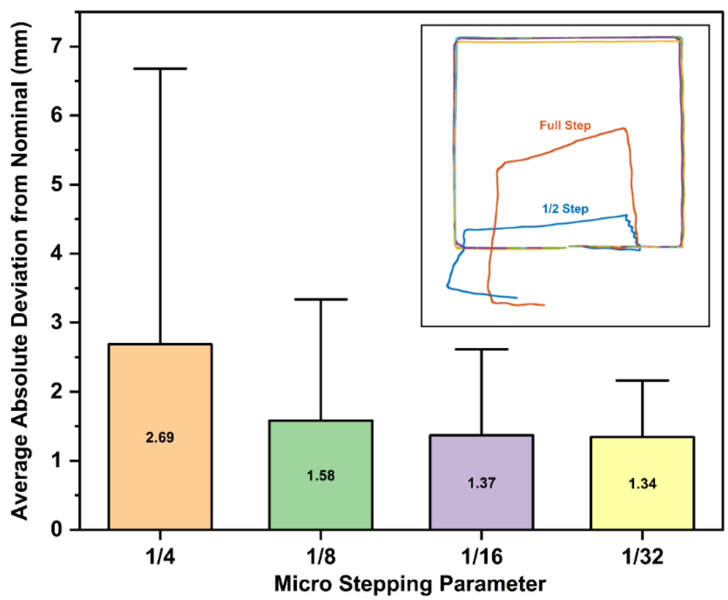

Figure 2-47: Plot of average deviation with respect to changing micro step resolution. Overlayed is a top down view of the averaged print trajectories.

When compared to the previous micro-step resolution studies peformed in the early stages of the research, it can be noted that the results were exactly opposite of each other. The main difference between the two sets of experiments was the speed at which they were conducted. The first experiment was conducted at a much faster speed (77 $mm.s^{-1}$) than the second experiment (1.5 $mm.s^{-1}$). When the first experiments were conducted, it was unclear what printing speed would be required and therefore the results proved to be inaccurate.

Effect of Bridge Gap on Max Deflection

In addition to quantifying repeatability and accuracy of the mobile platform, it was necessary to understand the parameters related to the printing process. A study was conducted to analyze the deflection of printed parts as bridges were printed to span various distances. To examine this, an empirical test was performed to determine the max overhang possible with this material. After several trials, it was determined that the largest gap that could be spanned was approximately 60 cm before the weight of the printed part counteracted the viscoelastic properties of the ink being extruded (Figure 2-48). The averaged values of this 60 cm print can be seen in Figure 2-49.a

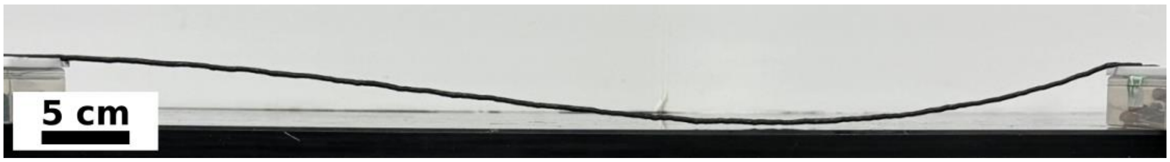

Figure 2-48: Side view of 60 cm bridge demonstration.

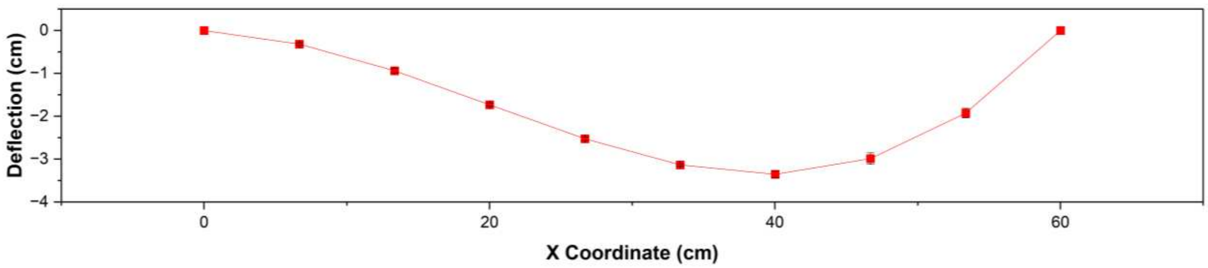

Figure 2-49: Averaged deflection of the printed material with respect to the x-coordinate over the course of a 60 cm overhang test.

With the maximum span determined, bridge gaps in 10 cm intervals down to 10 cm were printed and analyzed using SolidWorks to measure deflection (Figure 2-50). The bridging prints spanned between two blocks of PLA material. Due to the heat of the exothermic curing reaction, the PLA slightly melted upon material deposition, and this resulted in a strong mechanical bond between the cured ink and the PLA blocks. It is interesting to note the irregular curve of the plotted points as the distance between blocks increased. This is likely due to the changing distributed load on the cantilevered samples and the abrupt transition back to the final print surface.

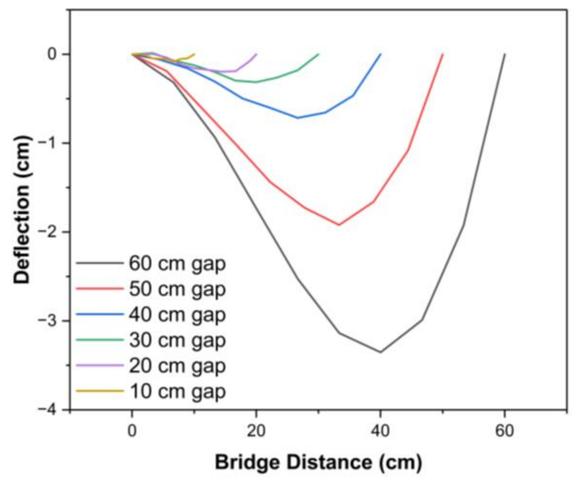

Figure 2-50: The effect of bridge gap on the deflection of printed overhang beams.

When looking at the max deflection of the printed samples in Figure 2-51, it is easy to see the relationship between the distance spanned and the deflection of the printed parts. In the worst case, a deviation of approximately 3.5 cm occurs. While this deflection seems significant, it should also be noted that this is at a distance that is approximately twice the max print size of a standard, commercially-available Prusa FDM printer [57]. This max bridging distance can also likely be increased if the system were to be scaled to a larger diameter print nozzle.

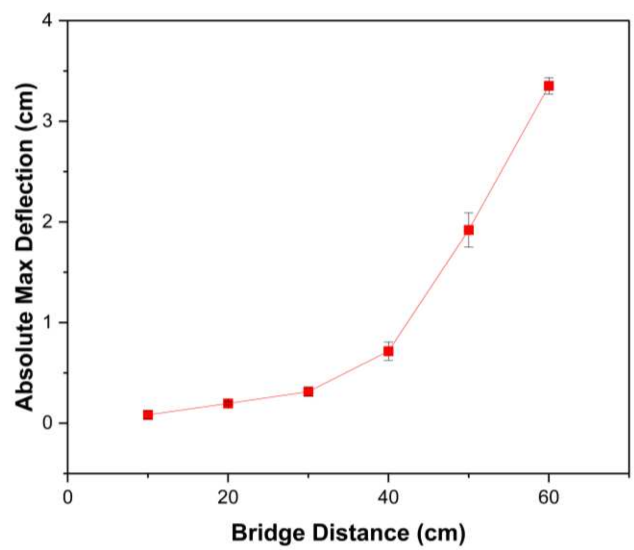

Figure 2-51: The effect of bridge gap on the max deflection of printed samples.

Effect of Laser Quantity on Print Speed

The majority of the prints performed were at a print speed of approximately 1.5 mm/s due to the ease of control and the ability to print geometries with just one laser focused on the printed ink. It was hypothesized that increasing the power of the lasers used to cure the ink would increase the print speed. To test this hypothesis, several different quantities of lasers at a fixed power density were used to cure the material. Cantilevered beams were printed off a PLA block to ensure that the induced front speed was sufficient enough to print freeform geometries. Frame-by-frame camera measurements were used to measure the speed of the robot in mm/s.

The first step was to establish a baseline print speed with front initiation, but no constant laser interaction. To do so, a singular laser was turned on for one second and then turned off to initiate cure of the material. Once the front began to propagate, a cantilevered beam was printed at an average print speed of 0.83 mm/s. In the following experiments, one laser was turned on and the printing speed of the platform was increased until it was not possible to print freeform geometries. This was repeated with up to three lasers, where each of the lasers do not overlap with each other and are at a fixed power density of approximately 0.3 W/mm^2. The results of this study can be seen in Figure 2-52.

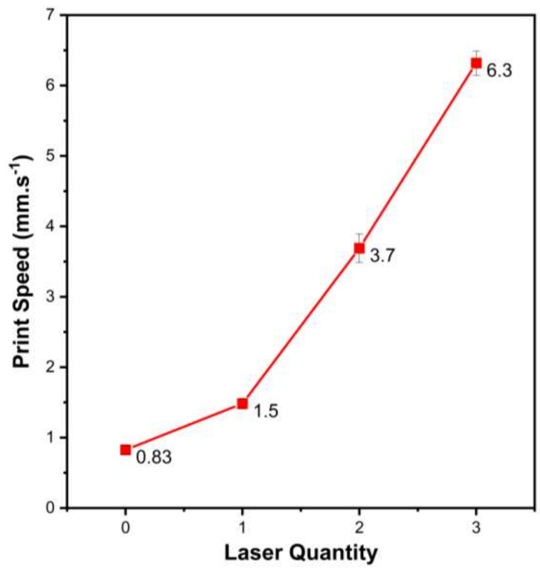

Figure 2-52: The effect of laser quantity on max print speed of freeform geometries.

This study confirmed that the print speed can be increased by increasing the laser power, equivalent to the number of lasers used in the process. When considering scaling this system, this approach proves to be a useful metric, facilitating rapid part manufacturing. This study also shows the versatility of the resin system and the ability of curing using an exothermic chain reaction, despite the addition of thermally insulating additives such as fumed silica. Additionally, the print speed was observed to further increase with the addition of more thermally conductive additives, i.e., carbon black and carbon fiber.

2.6.3 Demonstration of Platform Capabilities

While several of these demonstrations below were briefly mentioned in previous sections, the following section goes more in depth on demonstrations performed throughout the course of the research. These demonstrations were performed using the final mobile platform assembly detailed in design iteration five. All demonstrations were performed using the milled fiber ink formulation.

Long Sin Wave Print

To demonstrate platform capabilities of printing large parts and the ability to cure material omnidirectionally, a 2.5 m long sin wave was printed (Figure 2-53). This sin wave was printed using the 8 laser end effector and was printed directly on a concrete floor. Minimal warpage and high print fidelity were observed after part printing was complete.

Figure 2-53: 2.5 m long sin wave printed on concrete floor to demonstrate part size capabilities.

Outdoor Printing

To demonstrate the ability of the mobile platform to print on a variety of surfaces, an 80-mm OD cylinder was printed on a rough, concrete sidewalk (Figure 2-54). This was on a cloudy day at a temperature of 70 °F. While the surface quality of the printed structure was worse than that seen in indoor applications, this demonstration helped to highlight the capability of the platform to print successfully in a variety of environments.

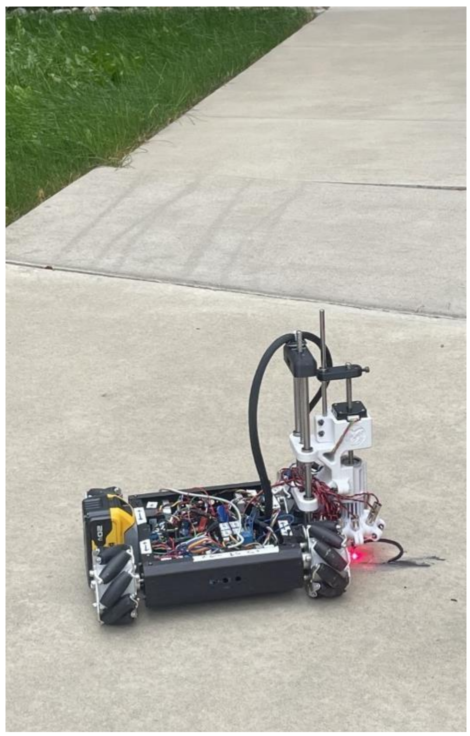

Figure 2-54: Mobile platform printing on an uneven, rough concrete sidewalk to demonstrate print surface flexibility.

Five Layer, Large Rectangle Print

To demonstrate the print fidelity and the ability to print multiple layers, a 300 mm by 25 mm rectangle was printed (Figure 2-55). This rectangle is larger than the print size of common, gantry style 3D printers. The part consisted of five layers and showcased consistent extrusion and path trajectory as shown in the close-up, view in Figure 2-56.

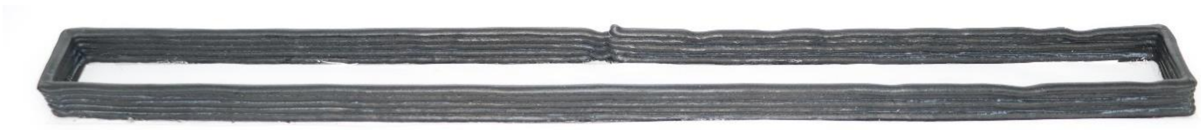

Figure 2-55: Final printed part showcasing high print fidelity.

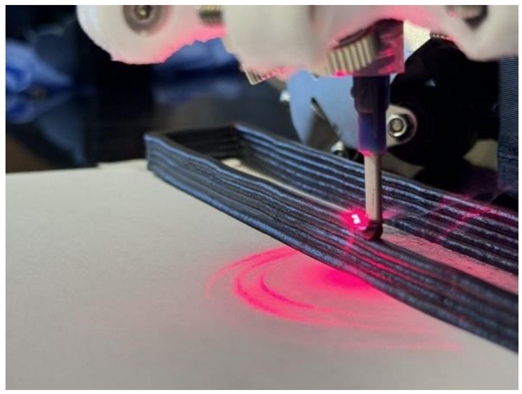

Figure 2-56: Printing process of a large, 5-layer rectangle.

Upside Down Printing

To demonstrate the platform's ability to print with a variety of nozzle orientations, several upside down prints were performed. The first was a single-line bridge between two PLA blocks as shown in Figure 2-57.

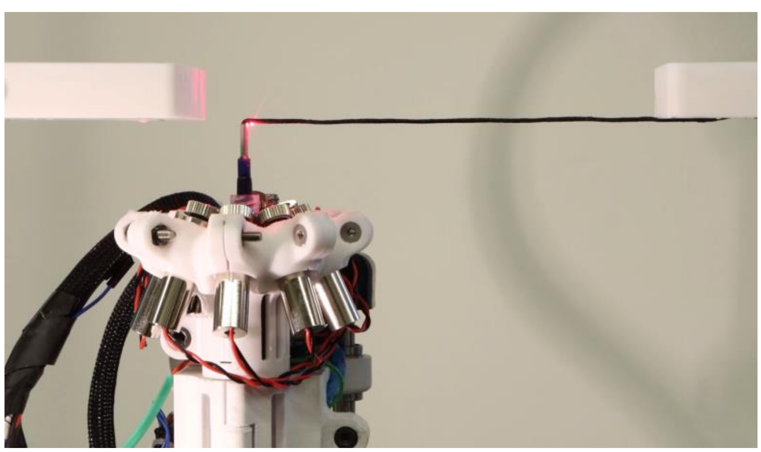

Figure 2-57: Upside down, single-line bridge print between two PLA blocks.

This print was scaled to a multiple road bridge as seen in Figure 2-58.

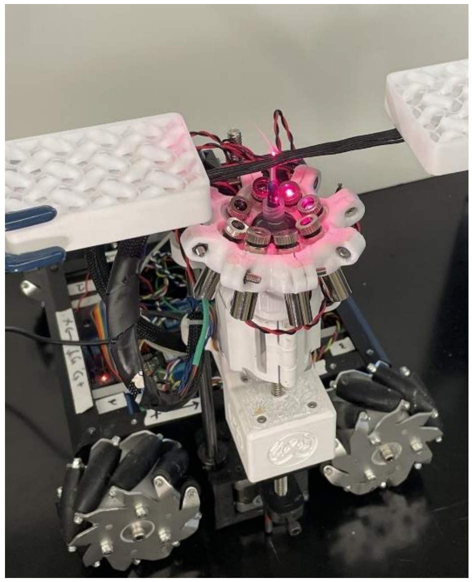

Figure 2-58: Multi-road upside down 3D print demonstrating an overhang of approximately 150 mm.

Not only is the printing capability increased with the use of free form printing, but more freedom is allowed in robot locomotion as there is no issue with part/robot collisions as there is with conventional mobile additive manufacturing.

<u>Bridge Printing</u>

To demonstrate high-strength, geometrically unconstrained printing, the mobile platform printed itself a bridge to perform a task. Initially, a gap too large to cross (150 mm) prevented the robot from performing a task (turning on LEDs). To solve this problem, the mobile platform printed two bridges and crossed them to turn on the LEDs.

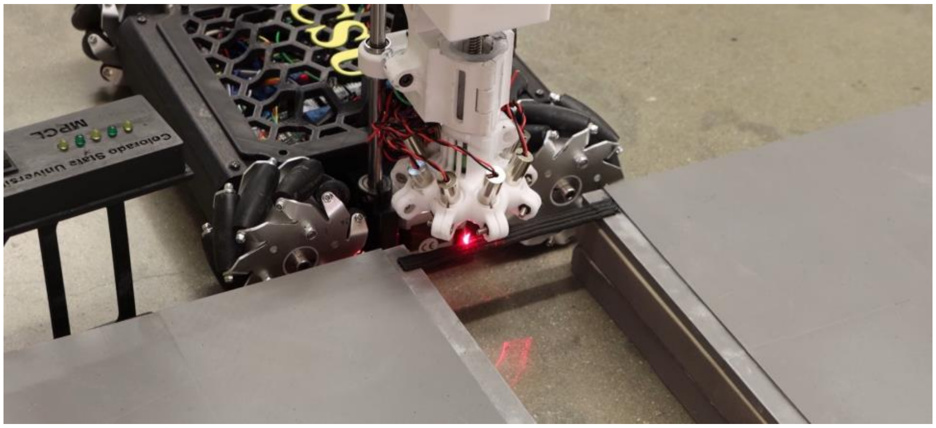

Figure 2-59: Robot printing a 10 road, 150 mm bridge to cross.

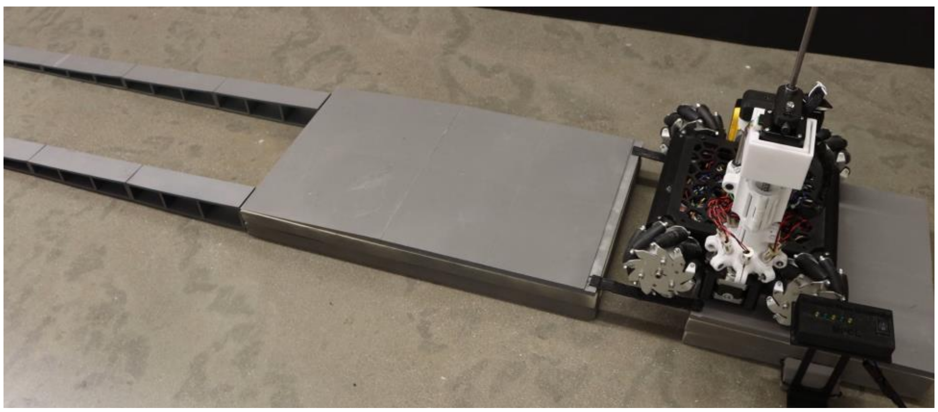

Figure 2-60: Robot successfully crossed the self-manufactured bridges to complete a task.

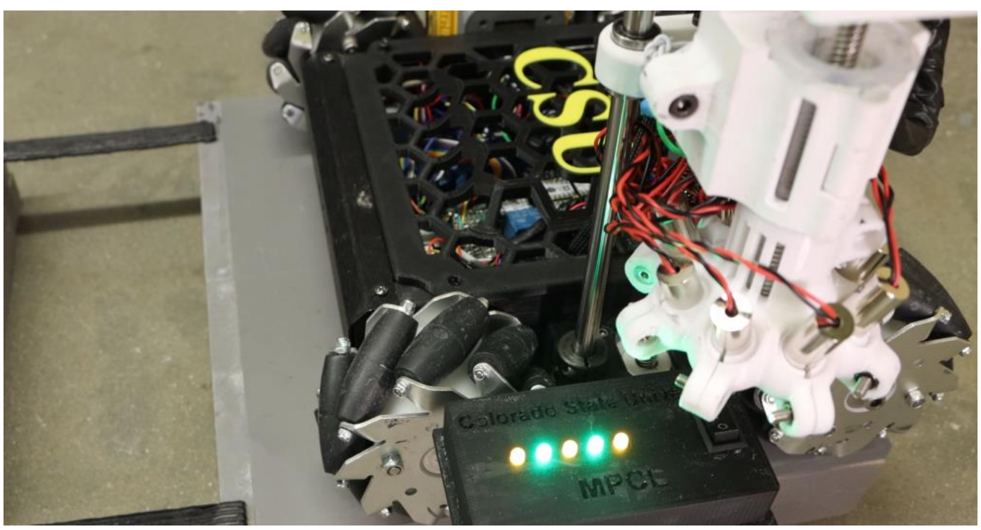

Figure 2-61: Robot demonstrated successful task completion by turning on a series of LED lights that could not be switched on without crossing the gap.

Chapter 3. FILAMENT WINDING

3.1 Introduction

This chapter focuses on rapid manufacturing of continuous carbon fiber composite structures via integration of thermally curable resin systems in filament winding processing technique. The first part of the research effort was focused on the improvement of an extant filament winding machine including mechanical upgrades, circuitry upgrades, and programming improvements. Once a reliable filament winding system was established, experiments were performed to improve the system and to characterize the processing parameters associated with composite fabrication using the novel, thermally curable resin system.

3.2 Platform Improvement

To begin this work, an extant filament winding machine was updated to better fit the requirements of manufacturing large parts quickly. This machine was a simple, two-axis, headstock style machine that was initially developed as a senior design project. During the senior design project, several small filament-wound parts were manufactured. While this setup was sufficient for the development of small-scale, low-volume parts, it required upgrades to be able to repeatably produce large parts. Based on initial testing of the old system, inconsistencies arose from part-to-part and the overall winding process was time consuming and difficult.

3.2.1 Increased Rigidity

During initial testing it was found that the machine was not capable of handling substantial amounts of torque from high fiber tension. Originally, tensioning the fiber tow was difficult as the machine consisted of two separate frames: the headstock and resin bath were mounted on one frame and the continuous fiber tow was mounted on the other frame. To address these issues, the machine was consolidated into one large frame. As a result, the overall machine frame was shortened, and the continuous fiber tow was now able to be tensioned properly. To add tension to the tow, a simple, turnbuckle-style tensioning system was added beneath the spool of continuous fiber. This allowed for winding tension to be set consistently and repeatably.

After consolidating the frame and installing the tensioning system, the system was checked for loose hardware and unstable connections. While the extruded aluminum frame allows for design flexibility and ease of modification, it also provides weak points in terms of rigidity. This was improved by adding braces and gusset-style supports. This was especially critical around the mandrel area as initially the stepper motor flexed the whole frame during high-tension winding. At this point, the frame was significantly more robust and allowed more control over important processing parameters. The next step in improving the system was to improve circuitry for ease of communication/programming and to allow for the incorporation of more devices into the system.

3.2.2 Circuit Overhaul and Programming Updates

Originally, the system utilized two Arduinos, one to control the rotation of the headstock, and one to move the resin bath. This made it difficult to communicate back and forth between the two, making the coordinated motion challenging. With the pre-existing programming, the headstock and resin bath were stuck in constant motion with no capabilities of repeatable part programming. An attempt was made to use serial communication as a means of coordinated motion, but this led to delays in communication as well as the inconvenience of unplugging the communication pins any time the code was required to be updated. As a result, the circuitry was completely redesigned and replaced with a singular Arduino. A custom-made protoboard circuit was developed to replace the initial breadboard/Dupont wire connections. In addition to consolidating the motors to one board, a limit switch was added so that the resin bath could be homed and consistently start from the same point. This made it possible to program consistent parts on a mandrel. In addition, a series of buttons were added to allow for a more user-friendly interface. A homing button for the resin bath was added as well as a start and stop button that allowed the operator to pause or end the winding program at any time. At this point, part programs could be created for specific parts based on the parameters described in Table 3-1.

Table 3-1: Important programming parameters to create repeatable parts along with minimum and maximum values seen throughout.

Important Programming Parameters	
Part Length	61.2 – 250 mm
Resin Bath Linear Speed	1.2 – 30.6 mm/s
Distance Resin Bath moves after Contacting Limit Switch	245 – 270 mm
Distance Resin Bath moves after Completing Wind	40 – 80 mm
Number of Layers	3 – 11
Headstock Rotational Speed during Wind	4.9 – 19 RPM
Headstock Rotational Speed during Cure	0.5 – 19 RPM

3.2.3 Mandrel Improvements

With a more user-friendly programming approach in place, the next step was to create part programs. In order to do so, it was necessary to establish a mandrel system that allowed for easy removal of parts and enough heat resistance to withstand radiation from the IR heat source.

Mandrel Attachment System

The extant machine utilized a four-jaw, chuck-mounting system that attached the mandrel to the headstock as seen in Figure 3-1. While this mounting system allowed for mandrels of different sizes to be attached to the headstock, it was time-consuming and difficult to ensure the mandrel was centered and properly supported on all surfaces. Additionally, it was difficult to incorporate an IR bulb to act as a thermal stimulus due to the large diameter of the chuck plates. As a result, this system was swapped out for a simple Jacobs chuck mounting system. The new mandrel mounting system allowed for quick and easy mandrel removal as well as a more robust connection to the headstock. In addition to creating a more robust mandrel mounting system, the original stepper motor was swapped out for a stepper motor with a 4:1 gear ratio to increase fiber tension capabilities.

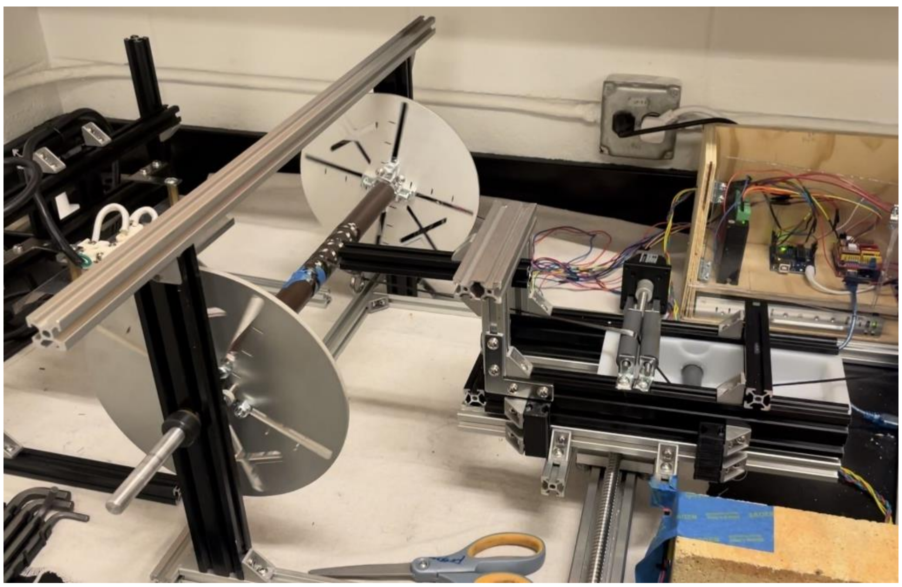

Figure 3-1: Filament winding machine with the original chuck mounting system on the left and the original, multiple Arduino communication on the right side of the image.

With this new mandrel mounting system, a variety of mandrels could be used to wind parts of different sizes and shapes. The following is a brief overview of mandrels used throughout the course of the project in chronological order.

<u>Soft Mandrel</u>

The first mandrel that was considered was a two-piece, soft mandrel. This design consisted of a steel core that was encased with a soft temperature-resistant silicone sleeve. The idea was to design the mandrel with a certain level of flexibility so that the outer, flexible sleeve could be removed post-winding, and the part would be easy to remove from the flexible sleeve. While this idea seemed feasible on paper, its implementation was less than desirable. The tension from the winding and the part shrinkage after winding made the removal of the flexible sleeve from the mandrel difficult, and parts were trapped as a result.

Small Diameter Aluminum Mandrel

The first rigid mandrel used was a small diameter (OD = 30 mm), aluminum mandrel. This system worked well enough to produce several small-diameter parts, but part removal after cure proved to be difficult. In order to remove parts, the wound part and mandrel were frozen to induce contraction of the mandrel. While this worked to remove parts, it should be avoided as it can potentially lead to material property degradation. Additionally, at this point in the research, it was desirable to move towards larger diameter mandrels to test the capability of the machine as well as to facilitate the manufacturing of mechanical testing samples in the future.

Large Diameter ABS Mandrel

Before the addition of a more powerful stepper motor, weight was an important consideration for mandrels. As a result, a high-temperature, large-diameter (OD = 90 mm) ABS mandrel was implemented. The mandrel was wrapped in receipt paper and aluminum foil tape in an attempt to facilitate part removal. While the ABS itself held up well and did not melt under IR power, part removal was still difficult. Thermal contraction of the ABS mandrel was not as significant and more effort was required to remove the part from the mandrel after curing.

Large Diameter Aluminum Mandrels

After the addition of a more powerful stepper motor, mandrel weight was not a constraint. This facilitated the use of large diameter aluminum mandrels, ranging in outer diameter from 100 to 115 mm. Both unpolished and polished mandrels were evaluated. Even with the use of mold release, unpolished mandrels still presented challenges in part removal. It was determined that polished mandrels represented the best case solution for facile part removal. When mold release is used, part removal is straightforward and allows for a significantly higher manufacturing rate.

Large Mechanical Sample Test Mandrel

In order to create composite structures that could easily be used for mechanical testing, a custom paddle-shaped mandrel was designed and manufactured out of aluminum. This mandrel enabled the manufacturing of 140-mm long, unidirectional fiber samples for flexure, compression, tensile, and fatigue testing samples. As seen in Figure 3-2, the paddle shaped mandrel rotated around a central axis driven by the headstock of the machine.

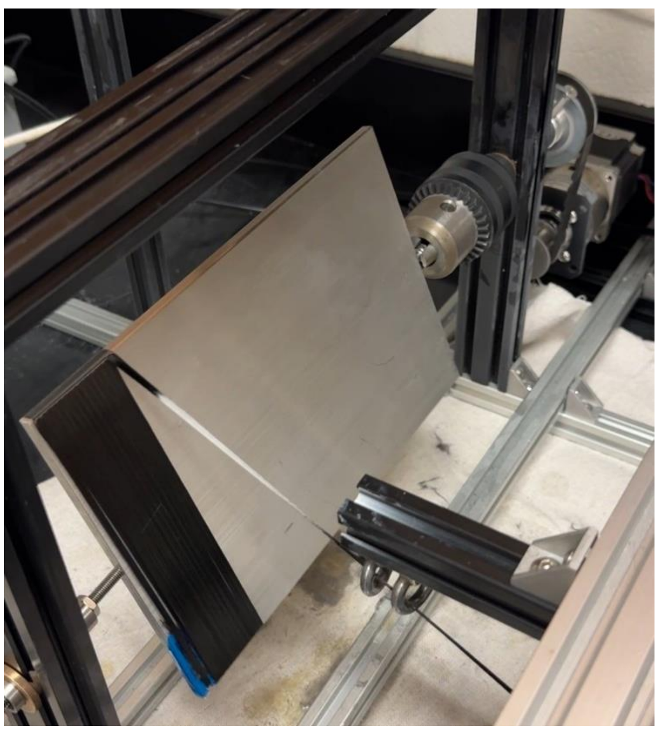

Figure 3-2: Paddle shaped mandrel for mechanical testing samples.

3.2.4 IR Heat Source Addition

The next step in platform improvement was to incorporate a thermal stimulus to initiate rapid curing of the resin. Two different IR heat sources were used throughout the research depending on specific part requirements. A low-power, small-profile IR bulb (Casso Solar, Unitube) was used to initiate cure for the majority of the parts. The small profile of the bulb allowed for easy manipulation of processing parameters. Depending on the part, the power input ranged from 500 watts to 2000 watts. Input power was controlled using a PID control within CCI Control Panel software. A second, much larger IR heat source (Casso Solar, V-Series) was used for the paddle shaped mandrel due to its more uniform heat distribution. This heat source operated on a power input of about 3,000 W.

3.2.5 Temperature Sensing Capabilities

The final change made to the extant filament winding platform was the addition of temperature sensing capabilities. Due to the rotational nature of the system, standard thermocouple attachment methods were not feasible. A system that utilized a slip ring to bypass the rotational movement of the mandrel was implemented. This hollow slip ring (6-channel, ID = 12.7 mm) mounted directly on the center shaft of the mandrel, allowed thermocouples wires to pass through for temperature measurement during winding (Figure 3-3).

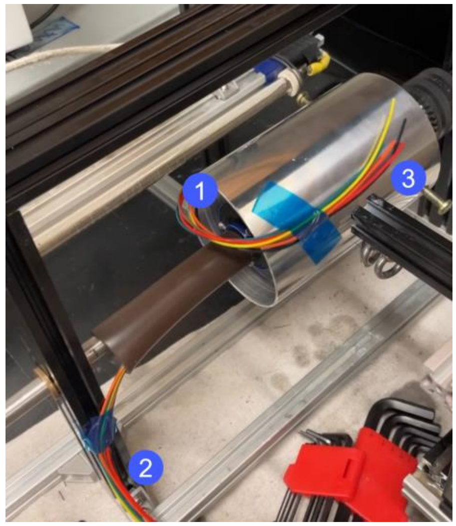

Figure 3-3: The hollow slip ring system where 1) is the hollow slip ring, 2) is the wires leading into the thermocouples, and 3) is the wires leading to the thermocouples.

The final state of the platform with improvements is shown in Figure 3-4.

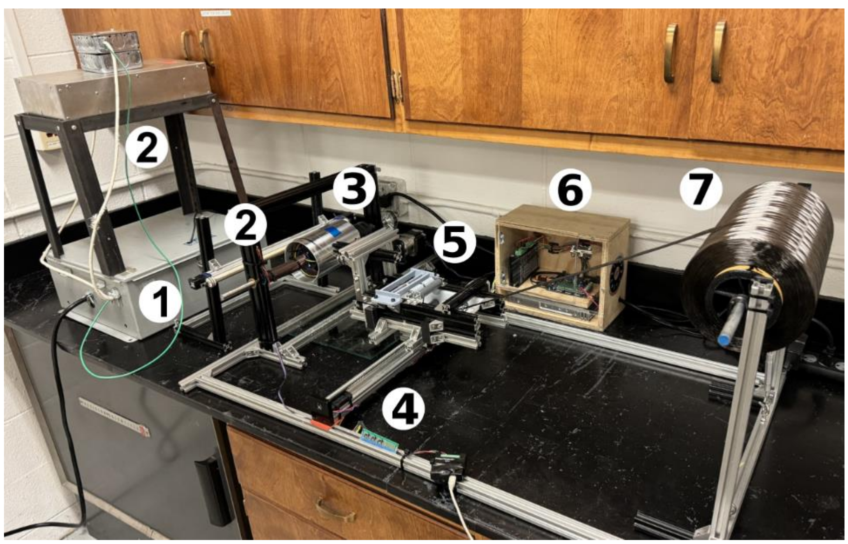

Figure 3-4: Final state of the filament winding machine where 1) is the electrical control box for the IR heat sources, 2) shows both IR heat sources, 3) is the polished aluminum mandrel with slipring and thermocouple, 4) is the user interface with buttons, 5) is the resin bath system, 6) is the electrical control box for the filament winding machine, and 7) is the continuous carbon fiber tow.

3.3 Experimentation

With an improved system capable of repeatedly producing filament wound parts, the next steps were to conduct studies to better understand the system. The first experiments were preliminary trial and error experiments to help refine the filament winding setup. Experiments were run to optimize the fiber volume fraction (V_f) of the manufactured samples. Next, experiments were conducted to analyze the thermal profile of dry carbon fiber with varying IR heating parameters. These experiments led to further studies helping to determine the thermal profile of catalyzed resin. Finally, trial and error experimentation was performed to optimize a mechanical sample manufacturing process.

3.3.1 Materials

Throughout the experimentation, various material systems were used for the purposes highlighted in more detail within each experimental section. These resin systems are outlined in Table 3-2.

Table 3-2: Basic outline of different combinations of resin and catalyst systems used.

Matrix System Overview	
Resin	*Catalyst System*
Proxima pDCPD Resin	**Standard:** Inhibitor: TBP Catalyst: GC2 Solvent: PCH
Proxima pDCPD Resin	**All-in-one:** Proxima CT722
10% Sigma pDCPD-90% Proxima pDCPD Resin	**Standard:** Inhibitor: TBP Catalyst: GC2 Solvent: PCH
10% Sigma pDCPD-90% Proxima pDCPD Resin	**All-in-one:** Proxima CT722

The mixing procedure for the standard resin system is outlined in Table 3-3. When using the all-in one catalyst system provided by the manufacturer, the solution of resin and liquid catalyst is mixed by hand until homogenous.

Table 3-3: Outlined mixing procedure for all standard resin applications.

	Standard Resin Mixing Procedure
1	Weigh out GC2 in mg using a small plastic vial.
2	Pipette PCH solvent into a different plastic vial.
3	Micro syringe pipette TBP inhibitor into PCH.
4	Tap PCH/ TBP plastic vial for 1 minute.
5	Pipette PCH/ TBP into GC2 vial.
6	Sonicate PCH/ TBP plastic vial for 10-20 minutes.
7	Weigh out Proxima pDCPD resin.
8	Pipette GC2/ PCH/ TBP solution into resin mixture.
9	Mix solution by hand until homogenous.

For the standard resin system, the components are weighed out with respect to the amount of resin used. For all experiments utilizing the standard resin mixture, 100 ppm of GC2, with respect to pDCPD, and 1 molar equivalent of TBP, with respect to GC2, are dissolved within 54 μL/g resin of PCH by sonication. This solution is then mixed with the respective amount of pDCPD resin. The mixture proportions were derived from work done by Ziaee et al [10]. For the all-in-one liquid catalyst solution, the mixing ratio is 50:1 resin to catalyst by weight. These procedures were used for all specimens within this work.

The reinforcement materials used are outlined in Table 3-4. Similar to the resin systems, the applications of each fiber are highlighted in more details within each experimental section.

Table 3-4: List of reinforcements used over the course of the research.

Reinforcement System Overview
Zoltek PX35 Continuous Tow 50k
Zoltek PX35 Continuous Tow 20k
Hyosung H2550 Continuous Tow 24k

3.3.2 Preliminary Trial and Error Experiments

The objective of the first set of experiments was to identify what factors led to the manufacturing of high-quality, filament-wound composite parts. During these experiments, IR heating was tested, part programming was debugged, doctor blading was introduced, microscopy was conducted, and the size of tow used for winding was evaluated.

<u>Initial 45° Fiber Angle Windings</u>

The very first step in this research was to determine if IR heating was compatible with this resin system. Three simple 45° wind angle parts were programmed around the small-diameter, aluminum mandrel (OD = 30 mm) discussed earlier. To program these parts, parameters were first adjusted using a dry fiber wind (no resin is added to the resin bath at this point). The purpose of this step is to debug coding and to weigh out dry fiber prior to a wet resin wind. These three parts were programmed using the parameters seen in Table 3-5.

Table 3-5: Important experimental parameters for 45° windings.

45° Winding Parameters	
Resin Bath Linear Speed (mm/s)	30.6
Part Length (mm)	132.6
Headstock Rotational Speed during Wind (RPM)	4.9
Headstock Rotational Speed during Cure (RPM)	4.9
Number of Layers	3
Total Part Thickness (mm)	4.06
Materials	Proxima, Standard, 50k fiber
IR Bulb Input Power (Watts)	1000
IR Bulb Distance from Mandrel (mm)	25
Cure Visual Onset (minutes)	1
Mandrel	30 mm OD Aluminum

Three different samples were manufactured using these parameters. The standard catalyst system was used at this point because it is well established through the work done by Goli et al [58]. During the first wind, not enough resin was used, and the part had to be scrapped. During the second wind, everything went smoothly, and the IR bulb was used effectively to cure the part. Cure was observed quickly at around the one-minute mark. The second part produced was very resin rich and led to the implementation of manual doctor blading after the wind to reduce excess resin content. The third part manufactured was doctor bladed and it appeared to help reduce excess resin content. Seen below in Figure 3-5 are the three steps of the filament winding process used to manufacture these parts.

Figure 3-5: First part wound using the redesigned filament winder machine where A) is the dry fiber test run, B) is the wet wound part after the IR bulb is powered on, and C) is the cured part.

After the parts were removed and weighed, V_f was calculated Equation 9 where ρ_m is the density of matrix, w_f is the weight of fibers, ρ_f is the density of fibers, and w_m is the weight of matrix [59].

$$V_f = \left[\frac{\rho_m w_f}{\rho_m w_f + \rho_f w_m}\right] \quad (9)$$

For this specific resin system and the carbon fibers used, the values of each variable are tabulated in Table 3-6. The weight values are measured using dry fiber before winding and total part weight after winding.

Table 3-6: Values for volume fiber fraction calculation [60], [61].

$\boldsymbol{\rho_m}$	1.03 g/ml
w_f	48.79 g
ρ_f	1.81 g/ml
w_m	38.5 g

Based on Equation 9 and the associated values of each variable, the V_f is calculated to be approximately 42%. This method of calculating V_f applies to all calculations from this point forward. According to the work done by Mertiny et al. [62], the filament winding process is capable of achieving V_f up to 70%. Due to its large effect on composite mechanical properties, it is desirable to seek an increase from the current value of 42%.

In addition to calculating V_f, an attempt was made to measure the temperature of the part during the winding process to ensure that cure was initiated properly. To do so, an infrared laser thermometer was aimed at the composite part during the winding. This process was not repeatable and was filled with uncertainty. Recorded data values were inconsistent, but never exceeded 120°C. While this process was uncertain, it shed light on the temperatures during the curing process and led to the implementation of more advanced temperature measurement methods.

Large Diameter Hoop Windings

With several successful parts demonstrated with the IR heating system, the next step was to test the capabilities of the system by attempting to manufacture larger composite parts. Part programs were created for the large diameter ABS mandrel. To ease the programming task and for more consistency, it was decided to move from helical windings to hoop windings. The programming parameters are tabulated in Table 3-7.

Table 3-7: Winding parameters associated with the large diameter hoop windings.

Large Diameter Hoop Winding Parameters	
Resin Bath Linear Speed (mm/s)	12.2
Part Length (mm)	132.6
Headstock Rotational Speed during Wind (RPM)	19
Headstock Rotational Speed during Cure (RPM)	19
Number of Layers	3-11
Total Part Thickness (mm)	2.5-6.1
Materials	Proxima, CT722, 50k fiber
IR Bulb Input Power (Watts)	1000
IR Bulb Distance from Mandrel (mm)	22
Cure Visual Onset (minutes)	1.5
Mandrel	90 mm OD High Temp ABS

The Proxima CT722 was implemented at this stage for ease of manufacturing and to test the compatibility of the liquid catalyst system with the IR heat source. To begin the experiment, several small 3-layer, 2.5-mm thick parts were wound. Everything went smoothly so the manufacturing was scaled to an 11-layer, 6.1-mm part. Both parts can be seen below in Figure 3-6.

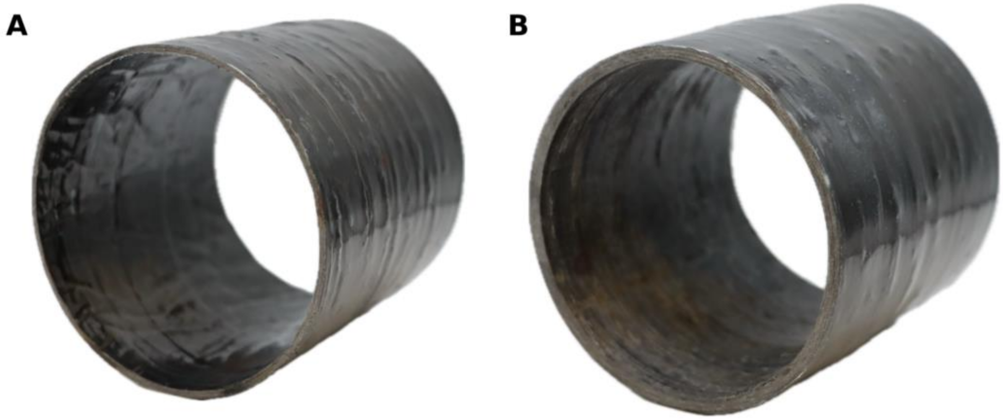

Figure 3-6: Filament wound composite structures where A) is the 2.5 mm thick part and B) is the 6.1 mm thick part.

The thicker part wound successfully, but several observations were noted throughout the wind. First, it was observed that the resin appeared to be too viscous for winding and as a result, air bubbles were trapped within the resin bath. These air bubbles had the potential to lead to non-uniform resin distribution and potential voids within the parts. Second, it was observed that there was too much excess resin on the part throughout the winding process, potentially leading to resin non-uniformity throughout the part. Across calculations from three different manufactured parts, V_f remained very consistent at approximately 42%.

To better understand resin distribution within the manufactured parts, digital microscopy was performed as seen in Figure 3-7. As seen in the cross sectional view, a large number of voids (black) are present within the structure and resin (dark grey) distribution is non-uniform. No calculations were performed to quantify void content at this time due to the undesirably high volume of voids present.

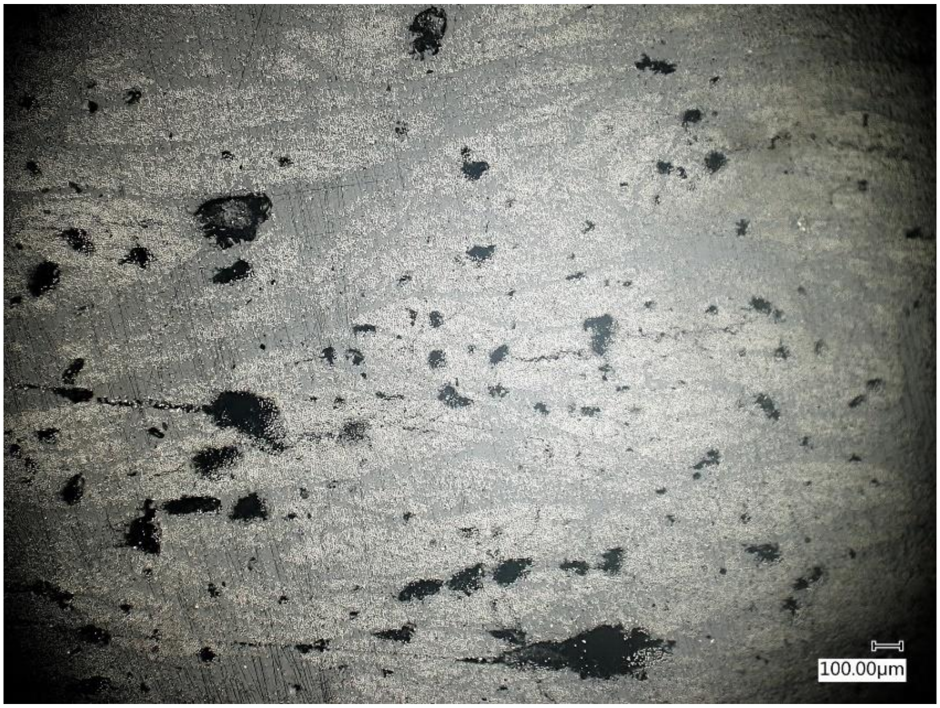

Figure 3-7: Cross-sectional micrograph of the 6.1 mm thick composite part.

<u>Fiber Comparison</u>

At this point in the research, it was uncertain why the V_f numbers were consistently low. One prediction was that the 50k tow lacked a binding agent to keep the fibers together. As a result, the 50k would be more difficult to process than tow with a binding agent and would result in a lower V_f. To test this, the same 11-layer part wound previously was programmed using the 20k tow. All the parameters remained the same except for the resin bath speed so that there were no gaps in between fibers. After the winding of the 20k part, V_f was calculated to be 49%. While the driving factor as to why the 50k tow produces a lower V_f still remains unknown, it was established that tow size makes a difference in the end result for this filament winding system. Because of the end goal of this research being on manufacturing large composite structures, it is still advantageous to continue research using the 50k tow, despite the lower V_f.

3.3.3 Volume Fiber Fraction Optimization

<u>Sample Manufacturing</u>

With preliminary trial and error testing out of the way to ensure that the system operated effectively and that the IR heat source was compatible, the next step in the research was to optimize the V_f achievable with the 50k tow. In an attempt to increase the V_f beyond 42%, two variables were changed. First, the resin viscosity was tuned. By mixing in small amounts of Sigma pDCPD (pDCPD resin with a lower viscosity than Proxima DCPD), the resin viscosity could be closely controlled. Second, a new wiper system was introduced to assist in removing excess resin from the tow (Figure 3-8). Both high viscosity and excess resin were observed in previous winds. The programming parameters as seen in Table 3-8 were used to compare parts for V_f optimization.

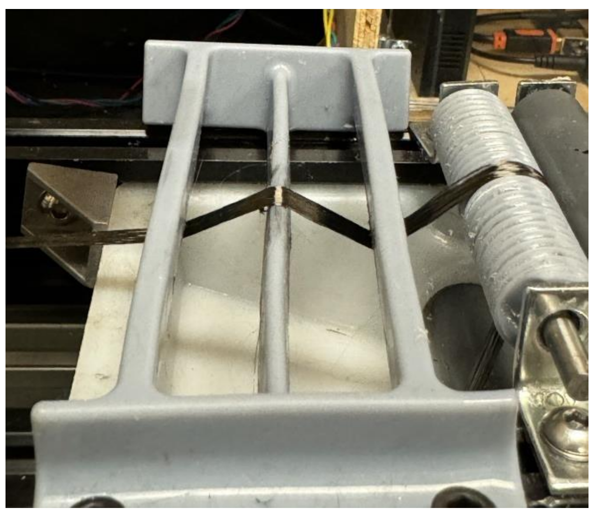

Figure 3-8: New wiper system that helped to remove excess resin from impregnated tow.

Table 3-8: Important parameters for V_f optimization studies.

Constant Processing Parameters	
Resin Bath Linear Speed (mm/s)	1.2
Part Length (mm)	61.2
Headstock Rotational Speed during Wind (RPM)	8.7

Headstock Rotational Speed during Cure (RPM)	3.8
Number of Layers	5
Total Part Thickness (mm)	3
Materials	Proxima, Sigma, CT722, 50k fibers
IR Bulb Input Power (Watts)	1000
IR Bulb Distance from Mandrel (mm)	25
Mandrel	115 mm OD Non-Polished Aluminum

The goal of this study was to attempt to increase the V_f to an acceptable range of 50-55%. Four different tests were run using the constant parameters listed above. First, a control group part containing Proxima pDCPD was manufactured. The new wiper system was not implemented. The purpose of this test was to try and replicate the processing conditions used up to this point in the research. After the wind, the V_f was calculated to be approximately 43% which aligned well with previous results.

After winding a baseline part, the viscosity was decreased by using the 10% Sigma pDCPD-90% Proxima pDCPD resin system. Everything else was kept constant throughout the wind and a slight increase in V_f at 44% was observed. While this was promising, it still was not within the desired range. However, the manufacturing process went better as the excess resin decreased and no air bubbles were observed in the resin bath.

The next part that was manufactured utilized the wiper system. In this system, the resin impregnated tow is separated using a roller with ridges and then the tow is passed through a series of wipers to remove excess resin. By adding this step, the resin content on the part itself was reduced and excess resin was not prevalent. This part was manufactured using the Proxima pDCPD resin system. When the V_f was calculated after the part was manufactured, the value was 51%. Not only did this modification result in fiber volume fractions within the acceptable range, but it also reduced the resin consumption by 33%. The wiper system returned excess resin to the resin bath, instead of it going to waste.

With promising results showcased with the wiper system, the final experiment was run to test the effect of decreasing both the resin viscosity and the implementation of the new wiper system. This test used the 10% Sigma pDCPD-90% Proxima pDCPD resin system and the wiper at the same time. After cure, the V_f was calculated to be 48%. While initially this value does not make logical sense, it could potentially be attributed to the wiper system working more effectively when the resin has a higher viscosity.

<u>Digital Microscopy</u>

After testing the effect of the four different parameters, digital microscopy was performed to analyze the quality of produced parts. The cross-section of each part manufactured can be seen below in Figure 3-9.

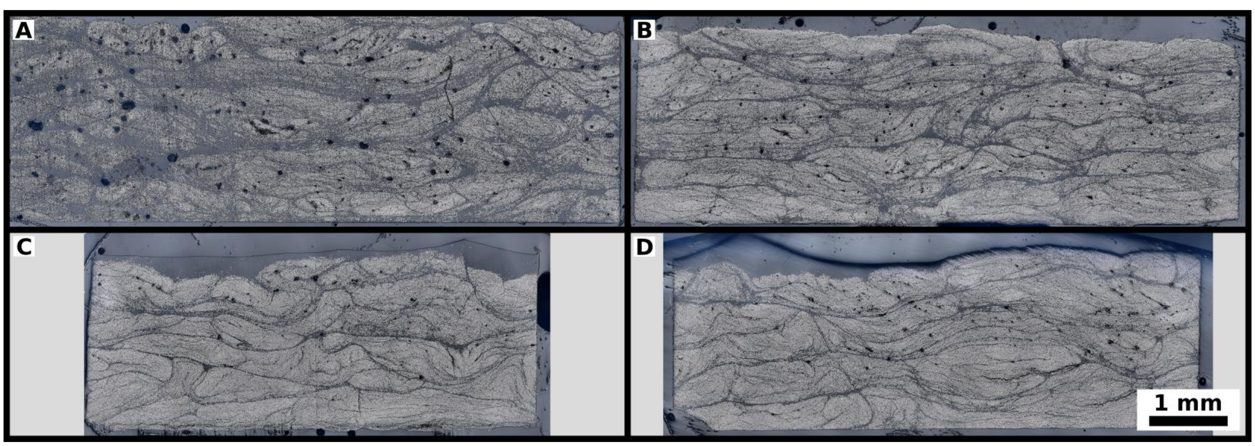

Figure 3-9: Cross-sectional micrographs from the parts made in the V_f optimization study. A) control group wind, B) reduced viscosity wind, C) addition of the wiper system, and D) reduced viscosity and wiper system wind.

Upon analysis of the micrographs, the following conclusions can be drawn. While there are voids present in all of the samples, they are less prominent in the wiper samples, especially the bottom layers. Additionally, it can be seen visually that the fiber content is higher in the wiper samples. Interestingly enough, both of the wiper samples contain excess resin on the outside of the part meaning that with better doctor blading methods, the V_f could be potentially further improved.

<u>Degree of Cure Measurements</u>

The composite samples appeared to be fully cured based solely on visual observations. DSC experiments were run to quantitively determine the degree of cure. A composite part was manufactured using the same parameters as the Proxima wiper part manufactured during the study. Two samples were taken from the part and a ramp test from 5°C to 250°C was applied using the DSC machine. Results can be seen below in Figure 3-10 where the averaged degree of cure (DOC) is 88%, represented by downward exotherms.

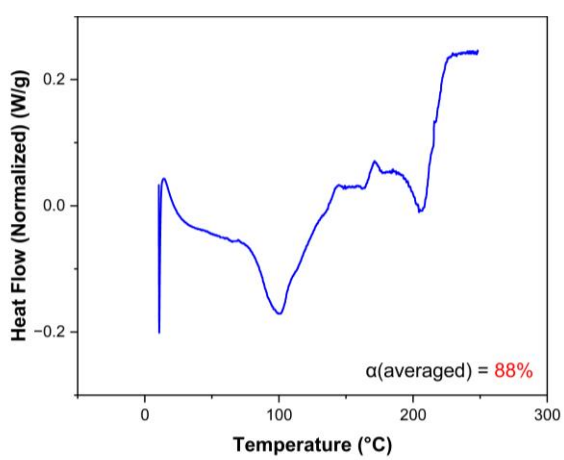

Figure 3-10: Heat flow of one of the samples used to determine average DOC.

A degree of cure of 88% is less than desirable and led to a shift in research effort to better understand the thermal profile of the composite part during the cure cycle.

3.3.4 Dry Fiber Thermal Profiling

To obtain a baseline for temperature profile and to understand the effects of IR heater parameters, a series of dry fiber experiments were run with a thermocouple to determine fiber temperature throughout the course of the wind. The following variables were changed to determine the effect on the thermal profile of dry fibers: IR heat source distance, IR heat source power, mandrel rotational cure speed, and low-power IR heating during the winding process (pre-heating). First, a dry fiber part was wound using the parameters seen in Table 3-9.

Table 3-9: Manufacturing parameters for dry fiber thermal profile experimentation.

Constant Processing Parameters	
Resin Bath Linear Speed (mm/s)	1.2
Part Length (mm)	61.2
Headstock Rotational Speed during Wind (RPM)	8.7
Headstock Rotational Speed during Cure (RPM)	0.5-33.8
Number of Layers	5
Materials	50k fiber
IR Bulb Input Power (Watts)	1000 - 1500
IR Bulb Distance from Mandrel (mm)	25 - 50
Mandrel	100 mm OD Polished Aluminum

In Figure 3-11, two thermocouples were used to measure temperature throughout the simulated manufacturing process. One thermocouple was flush against the surface of the mandrel and the other was just underneath the outermost layer of carbon fiber. Both thermocouples were calibrated using ice water as a reference temperature.

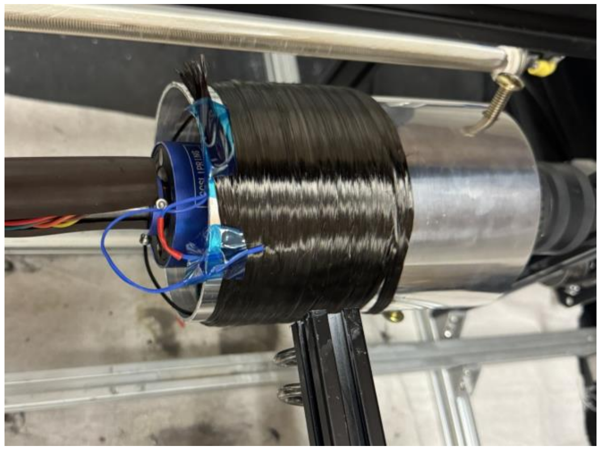

Figure 3-11: Dry fiber experimental setup with two thermocouples in inner and outer layers.

Control Group

To begin with, a control group cure cycle test was performed to better understand the processing conditions that were used to initiate cure up to this point in the research. The power input to the IR heat source was set at 1000 W, the IR heat source was 25 mm from the mandrel, and the rotational cure speed was set to 3.8 RPM. The thermal profile can be seen below in Figure 3-12. The oscillatory nature of the data is due to the thermocouple rotating with respect to the IR heat source as the mandrel rotates.

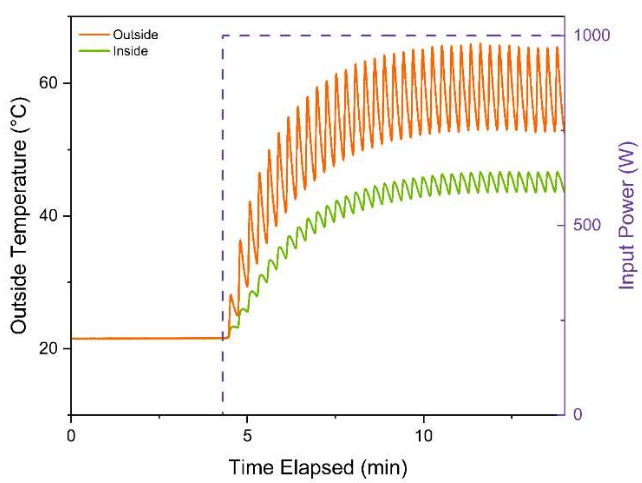

Figure 3-12: Control group temperature profile.

Effect of IR Heat Source Distance from Mandrel

With a baseline thermal profile established for the experiment, the IR heat source was moved away to 5 cm from the mandrel and the test was run with the same parameters as before. The comparison of outside temperatures between the two different distances from the mandrel is shown in Figure 3-13.

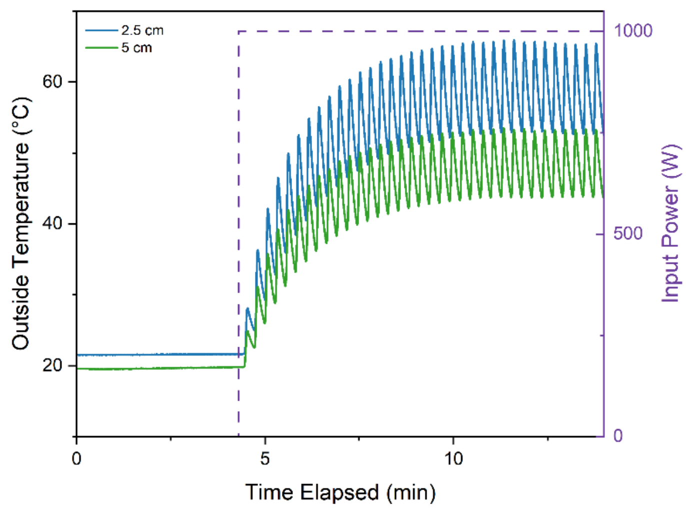

Figure 3-13: The effect of IR heat source distance from mandrel on outside fiber temperature.

Effect of Input Power to IR Heat Source

The next step in the experiment is to vary the input power to the IR heat source and test its effect on the thermal profile. The input power was changed to 1500 Watts and the test was run with the same parameters as the 5-cm wind. The comparison of outside temperatures between the two IR heat source input powers can be seen in Figure 3-14.

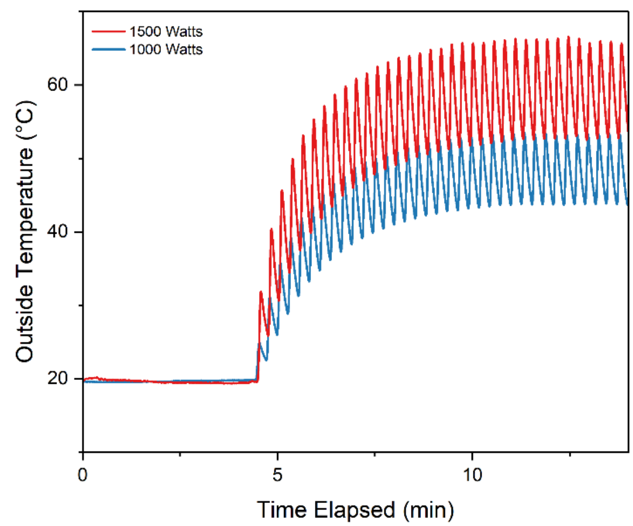

Figure 3-14: The effect of input power on outside fiber temperature.

<u>Effect of Rotational Cure Speed</u>

Next, the effect of rotational cure speed was evaluated. Three different speeds were programmed after the part winding. The three speeds tested were 0.5 RPM, 3.8 RPM, and 33.8 RPM. The rest of the parameters were the same with the exception of IR bulb distance from mandrel, which was fixed to 3 cm for the remainder of the experiments. Figure 3-15 shows the outside temperature comparison between the three different rotational speeds. Figure 3-16 shows the temperature gradients between the inside and outside thermocouple for the varying rotational speeds.

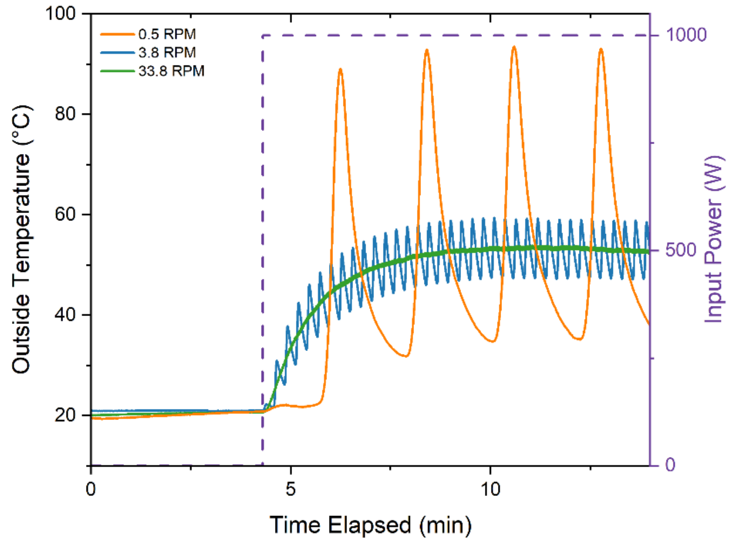

Figure 3-15: The effect of mandrel rotational speed on outside fiber temperature.

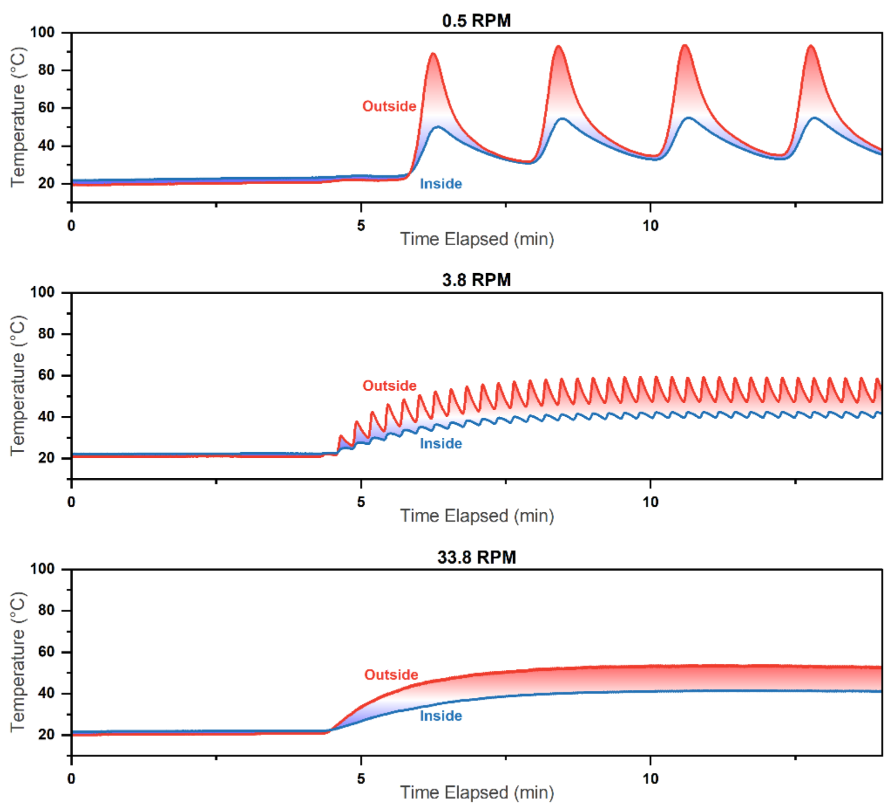

Figure 3-16: The effect of mandrel rotational speed on through thickness temperature gradients.

<u>Effects of Variable Power Cure Cycle</u>

The final test for the dry fiber experiment was to test the effect of a variable power cure cycle on the thermal profile of the dry fibers. One more test was run with the IR heat source at 3 cm from the mandrel and the rotational cure speed at 0.5 RPM. The variable cure cycle consisted of a preheat using 500 W input power during the winding, then increasing to 1000 W during the cure cycle. Figure 3-17 shows the comparison where purple curves represent the variable power cure cycle, and orange curves represent the standard cure cycle used to this point.

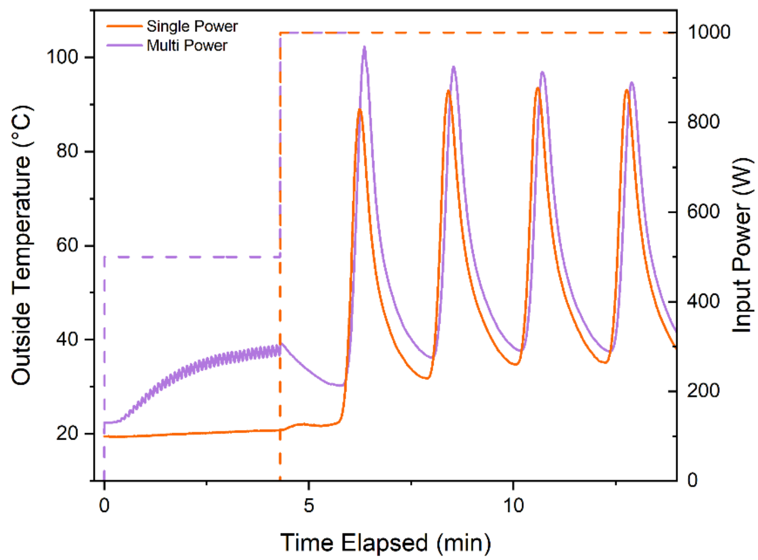

Figure 3-17: The comparison of temperature profile between a standard cure cycle and a variable cure cycle.

<u>Conclusions</u>

The low DOC (88%) of the parts that was measured previously is likely explained by the control group reaching a max temperature of only 65° C. There needs to be an effort to reach at least 80° C to properly initiate cure. In addition, there should be an effort to not let the inside temperature fall below 50° C to reduce temperature gradients within the part.

The following conclusions on processing parameters are drawn off the data collected in these experiments:

- The closer the part is to the IR bulb, the higher the peak temperature.
- The higher the input power to the IR bulb, the higher the peak temperature.

- The slower the part rotates during the cure cycle, the higher the peak temperature.
- The peak temperature appears to plateau after about 5 minutes of the IR bulb being powered on. This means the with the proper parameters, cure can likely be achieved after 5 minutes.
- A variable power cure cycle results in a higher peak temperature.
- The fastest cure time can be achieved with slower mandrel rotation speeds.
- A slow rotation speed might lead to temperature overshoot.

3.3.5 Catalyzed Resin Thermal Profile

Manufacturing with Rotating Cure Cycle

With an understanding of how processing parameters related to IR heating affect the temperature of dry fibers, the next step was to perform an experiment comparing the temperature profile of catalyzed resin with the previously established dry fiber temperature profiles. A part program was created using the parameters seen below in Table 3-10.

Table 3-10: Processing parameters for catalyzed resin experiments.

Constant Processing Parameters	
Resin Bath Linear Speed (mm/s)	1.2
Part Length (mm)	61.2
Headstock Rotational Speed during Wind (RPM)	8.7
Headstock Rotational Speed during Cure (RPM)	0.5
Number of Layers	5
Total Part Thickness (mm)	3
Materials	10% Sigma-90%Proxima, CT722, 50k fiber
IR Bulb Input Power (Watts)	1000
IR Bulb Distance from Mandrel (mm)	30
Mandrel	100 mm OD Polished Aluminum

The experiment was set up in the same fashion as the dry fiber experiments in terms of thermocouple placement. One thermocouple was placed against the mandrel surface and the other thermocouple was placed just underneath the last layer of carbon fibers. The experimental setup can be seen in Figure 3-18.

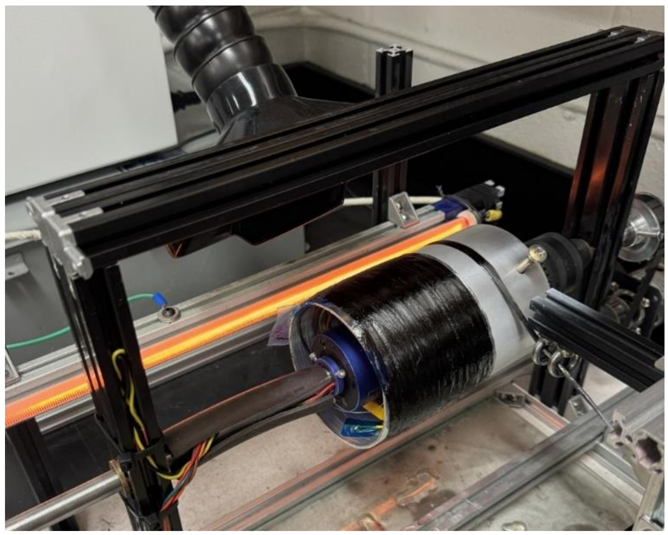

Figure 3-18: Experimental setup for the catalyzed resin experiments.

Parameters were the same as the dry fiber study. The temperature profiles comparing the outside and inside temperatures of the fiber can be seen in Figure 3-19 and Figure 3-20 respectively. In an attempt to locate exotherms, Figure 3-21 shows the peak-to-peak plot of both inside and outside temperature for the catalyzed resin and dry fiber windings.

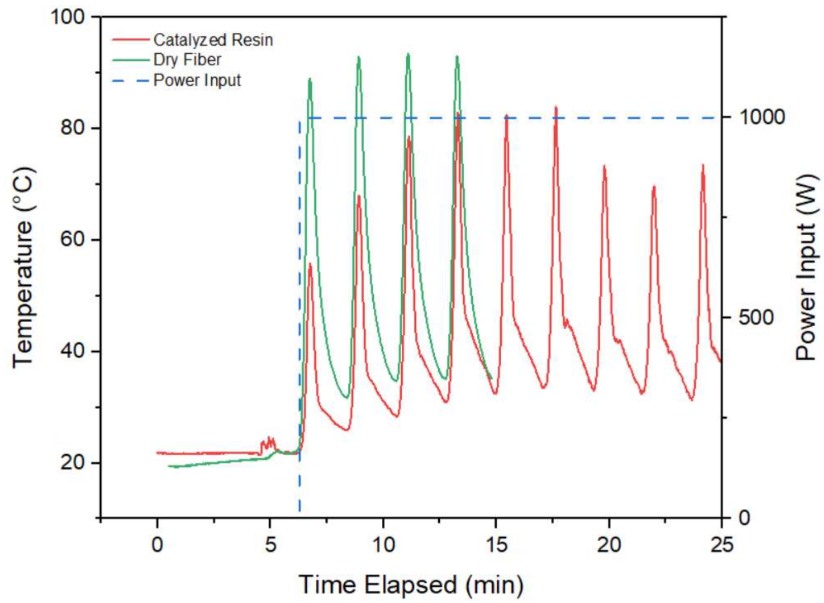

Figure 3-19: Outside temperature comparison between catalyzed resin and dry fiber winds.

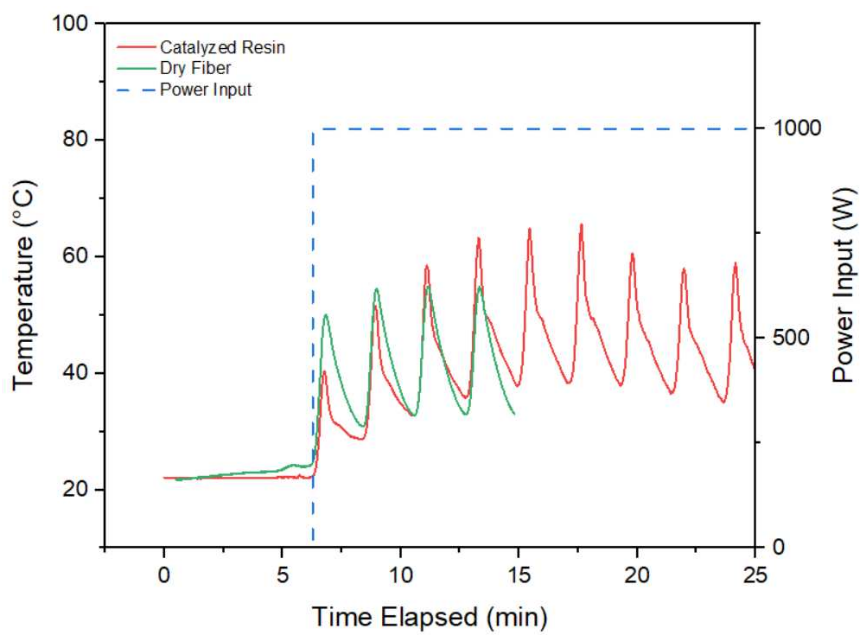

Figure 3-20: Inside temperature comparison between catalyzed resin and dry fiber winds.

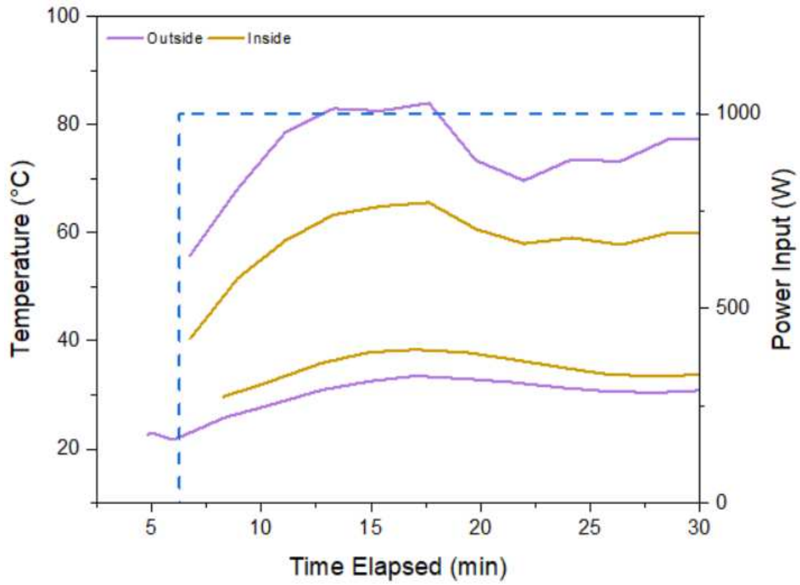

Figure 3-21: The combined inside and outside peak-to-peak temperatures for catalyzed resin winding.

<u>Conclusions</u>

The catalyzed resin thermal profile did not perform as expected. It was predicted that there should be temperature overshoot after the first peak over 80 °C due to front initiation. While it is slightly difficult to see, due to the oscillatory nature of the data, there did not appear to be a significant exotherm that would indicate frontal polymerization. The part appeared to be cured visually, but this was not indicated within the data collected. In an attempt to initiate cure later in the wind, the power input of the bulb was increased slightly with no exotherms observed as a result. During the curing process, the following observations were recorded:

- Catalyzed resin takes longer to heat up than dry fiber.
- Catalyzed resin cools off quicker on the outside of the part.
- Catalyzed resin does not appear to plateau like dry fiber does.
- Catalyzed resin shows an interesting slope change on the cool down phase of each cycle of mandrel rotation.

Due to the unexpected nature of the data collected during the catalyzed resin experiment, the study was duplicated, and the results were similar. Typically, front initiation is observed at around 80 °C, so it is interesting that no front was initiated at temperatures above 80 °C. As the results of these catalyzed resin experiments were not desirable, it was deemed necessary to evaluate the chemistry of the resin solution and ensure there were no issues with using the Proxima CT722 liquid catalyst for frontal polymerization.

3.3.6 Non-Rotating Cure Manufacturing

Duplicate Parameters

At this point, it was deemed necessary to narrow down factors contributing to the lack of frontal polymerization seen during the catalyzed resin experiments. The same process as previous catalyzed resin experiments was followed except there was no rotation involved for the first 15 minutes of cure. The purpose of this experiment was to evaluate if frontal polymerization would be initiated with no rotation of the mandrel during the cure cycle. The results of this experiment are seen below in Figure 3-22.

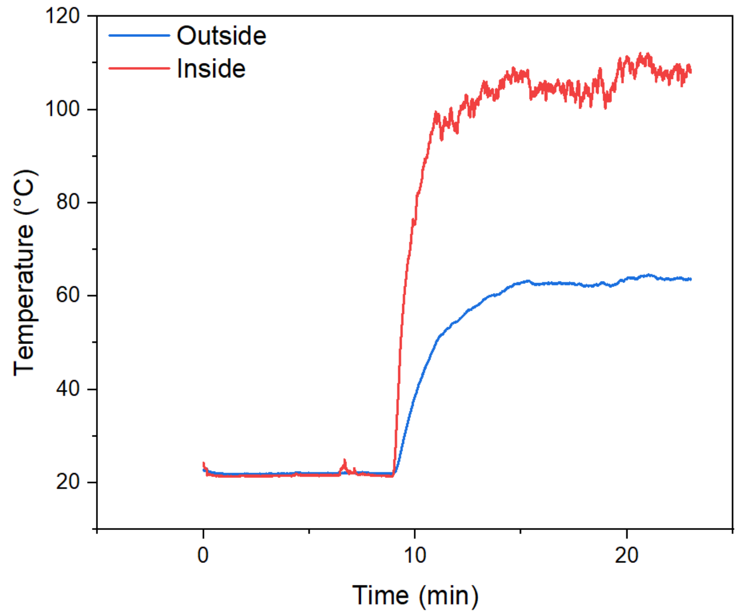

Figure 3-22: The temperature profile of a cure with no rotation.

Once again, there were no obvious exotherms observed during the cure cycle, despite temperatures reaching above 110 °C. This data contradicts previous knowledge of the resin system and once again raises the question of validity of the liquid catalyst system used.

Simple Front Initiation Experiment

To test the chemistry of the system, a simple experiment was conducted where the resin system was prepared and heated on a hot plate. The temperature of the heated plate was initially set to 80 °C but was raised incrementally due to no visual observation of frontal polymerization. This continued until the heated plate read 150 °C, 70 °C higher than expected for front initiation. At this point, a front was observed propagating throughout the resin. Because of the high temperature required for front initiation and the age of the liquid catalyst used in these studies (two years), it was determined that the issues were potentially due to an expired batch of liquid catalyst. As a result, a transition to the standard resin system was proposed for work done from this point forward.

3.3.7 Mechanical Sample Manufacturing

<u>No External Consolidation Pressure</u>

At this point, the research effort shifted to manufacturing specimens that could be easily used for mechanical test samples. Therefore, the paddle-shaped mandrel was implemented, allowing for the manufacturing of approximately 30 test coupons from a singular cycle of the manufacturing process. The success of these mechanical samples was reliant on resolving issues with the curing process seen during the catalyzed resin experiments conducted previously. In an attempt to mitigate these issues, a different approach was taken to ensure fully cured composite parts. Instead of using the all-in-one liquid catalyst system previously used, the standard resin system was implemented in hopes of properly initiating frontal polymerization. Additionally, the larger IR heat source was used for more input power into the manufactured specimens as well as a more uniform heat distribution over the composite part during the curing process. The parameters seen in Table 3-11were used to manufacture the samples.

Table 3-11: Processing parameters for the mechanical test samples.

Mechanical Test Samples Processing Parameters	
Resin Bath Linear Speed (mm/s)	0.4
Part Length (mm)	209
Headstock Rotational Speed Wind (RPM)	8.7
Headstock Rotational Speed Cure (RPM)	3.8
Number of Layers	17
Thickness	3.2
Materials	10% Sigma/90%Proxima, Standard, 24k fiber
IR Bulb Input Power (Watts)	3000
IR Bulb Distance from Mandrel (mm)	25.4 - 127
Mandrel	Paddle Shaped Aluminum Mandrel

The experimental setup can be seen in Figure 3-23, with the exception of the large IR heater, which is placed over the sample after the winding process.

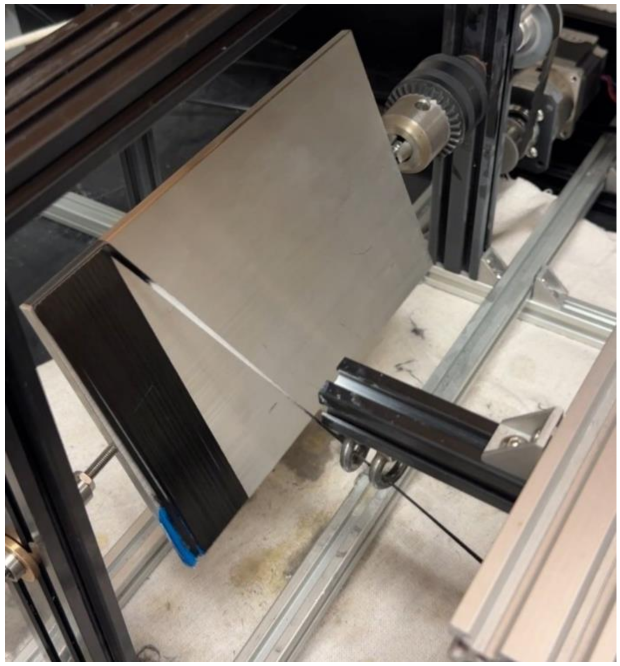

Figure 3-23: Experimental setup for the manufacturing of mechanical test samples.

The part was programmed using a dry fiber test wind as is customary for all parts manufactured. During the dry fiber wind, the continuous fiber tow did not have any gaps between fibers as seen in Figure 3-23. When resin was introduced into the system, consistent, small gaps were observed as seen in Figure 3-24. The tow aligned properly on the top of the part, but spacing did not remain consistent across the flat side of the mandrel.

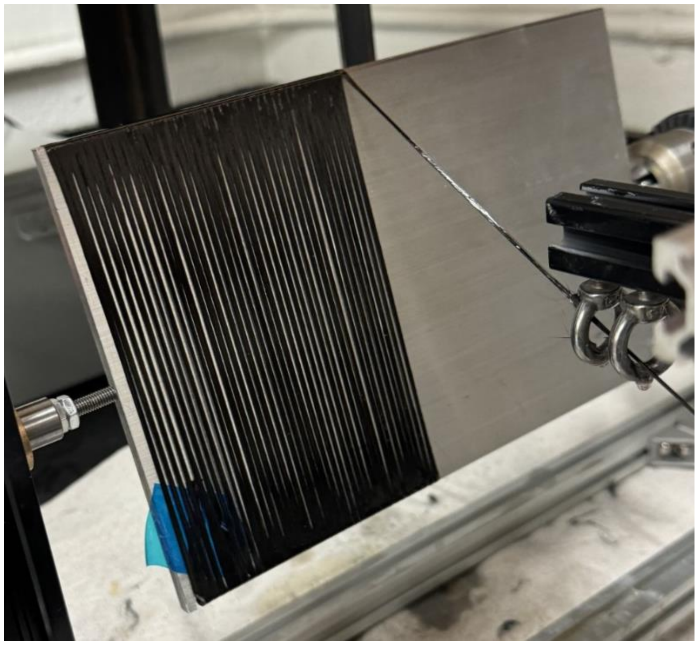

Figure 3-24: During the manufacturing of mechanical test samples, gaps can be observed between the lengths of tows.

Assuming this issue could be resolved with consolidation pressure, the part was finished and cured. After inspection of the cured part following removal from the mandrel, the gaps were still present as seen in Figure 3-25. Additionally, the long, flat sides of the part were over twice as thick as the top, shorter segments of the mandrel, also seen in Figure 3-25. This was likely due to surface tension of the wet resin during the winding changing the shape of the tow and the lack of consolidation pressure due to the unique geometry of the mandrel. The V_f calculated was the lowest seen thus far in the project at approximately 35%.

Figure 3-25: The first part manufactured where A) is the side profile and B) is a view of the interior of the part.

External Consolidation Pressure

To resolve this issue, glass plates were clamped to the part after winding and cure was initiated through the glass plates. This approach led to much higher consolidation pressure, ultimately resulting in no gaps between tows. During the curing process, a thermocouple was inserted into the part to verify cure and the results can be seen in Figure 3-26. The thermal profile shown indicates the initiation of frontal polymerization given by the exotherm seen at just over 80 °C. This is consistent with the expectation and helps to further prove that the issue previously encountered with cure initiation likely lies within the interaction of the liquid catalyst system and the IR heat source.

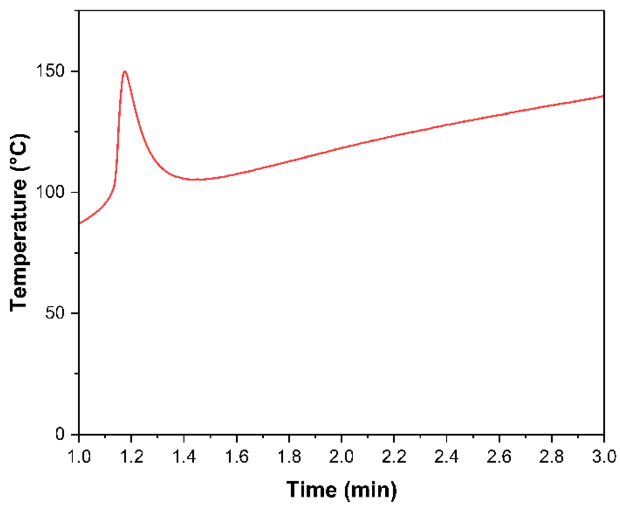

Figure 3-26: Temperature profile of the large, flat side of the mandrel during the curing process.

While the manufacturing of the mechanical test samples is an ongoing process, the indication of an exothermic peak at an expected temperature is promising for future work with manufacturing composite structures using this filament winding system and IR heat sources.

Chapter 4. CONCLUSIONS

4.1 Summary of Accomplishments

Within this thesis, the application of two different manufacturing methods for carbon fiber composites using a thermally responsive thermoset resin was investigated. The first approach involves the design, implementation, and evaluation of a mobile additive manufacturing system that was specifically developed for use with this resin system. This mobile platform allows for untethered manufacturing and repair in remote, potentially hazardous areas. The second approach involves the modification, implementation, and evaluation of a filament winding system specifically developed for use with this resin system. This system allows for rapid manufacturing of carbon fiber composites using a more traditional composite manufacturing approach.

In chapter one, the basics of composite materials, associated manufacturing processes, mobile additive manufacturing, and filament winding were outlined to provide relevant background information. A thorough literature review of previous work done in the fields was presented and research gaps were identified.

In chapter two, the design of a mobile additive manufacturing platform was thoroughly outlined. This work was presented in a chronological flow with five specific design iterations presented. At each stage of design, experiments were run to evaluate the quality of the platform. First, the mobile platform that was designed was validated to ensure that it fit the needs of the research. After this, the effects of micro stepping resolution were studied, and it was determined that 1/32 micro stepping provided the most accurate path trajectory. Next, the laser power was quantified and relationships between distance from substrate, laser spot size, and power density were determined. For the first time, an ink system was designed that showed shear-thinning behavior, high fiber alignment when printed, and a high degree of cure (99.4%) when a red laser is used to initiate cure. By increasing the laser power density, print speed could be increased. This ink system was used to bridge a gap of 60 cm with only about 3 cm of deflection. For the first time within the field of mobile additive manufacturing, high-strength, free form printing was demonstrated.

In chapter three, the improvement of a filament winding system was outlined and related experiments were thoroughly documented. First, the system was improved by creating a more rigid frame for the machine, increasing available torque for the system, incorporating a thermal stimulus, and adding temperature sensing capabilities. Once a solid, repeatable platform was designed, the fiber volume fraction was optimized to approximately 51% through a series of experiments. Microscopy and differential scanning calorimetry was performed to analyze the quality of printed samples. IR processing parameters were studied to establish the effect of IR heating on dry carbon fibers. A resin system was established that provided the optimal viscosity and pot life for manufacturing of filament wound parts. A mandrel system was designed to create flat test specimens for mechanical testing to determine the overall quality of the parts. For the first time, IR radiation was used to cure composites manufactured using filament winding within minutes.

4.2 Future Work

Building upon the work reported within this thesis, further design work and studies can be performed as follows.

4.2.1 Mobile Additive Manufacturing

- The control and movement of the platform could be further controlled with the addition of a closed-loop localization system.
- The degrees of freedom of the printing platform could be increased with the use of a robotic arm as opposed to a singular z-axis. This would allow for more geometrical freedom and printing capabilities.

4.2.2 Filament Winding

- Further characterization of thermal response using catalyzed resin could be conducted.
- Mechanical testing of wound parts using a three point bending approach.
- Investigation of continuous curing approach where the IR bulb is powered during the wind for fast manufacturing with low thermal spikes.
- Further microscopy to ensure that the wound parts contain low void content and uniform resin distribution.

REFERENCES

[1] Mallick, P. K., “Fiber-Reinforced Composites: Materials, Manufacturing, and Design,” CRC press, 2007.

[2] Schwartz, M. M., “Composite Materials Handbook,” *(No Title)*, 1984.

[3] Yourdkhani, M., “Overview of Processing Composites.”

[4] Bourban, P.-E., “Liquid Molding of Thermoplastic Composites,” *Comprehensive composite materials*, 2000, pp. 965–977.

[5] Van de Werken, N., Tekinalp, H., Khanbolouki, P., Ozcan, S., Williams, A., and Tehrani, M., “Additively Manufactured Carbon Fiber-Reinforced Composites: State of the Art and Perspective,” *Additive Manufacturing*, Vol. 31, 2020, p. 100962.

[6] Shi, B., Shang, Y., Zhang, P., Cuadros, A. P., Qu, J., Sun, B., Gu, B., Chou, T.-W., and Fu, K. K., “Dynamic Capillary-Driven Additive Manufacturing of Continuous Carbon Fiber Composite,” *Matter*, Vol. 2, No. 6, 2020, pp. 1594–1604.

[7] Li, Y., Xiao, Y., Yu, L., Ji, K., and Li, D., “A Review on the Tooling Technologies for Composites Manufacturing of Aerospace Structures: Materials, Structures and Processes,” *Composites Part A: Applied Science and Manufacturing*, Vol. 154, 2022, p. 106762.

[8] Yourdkhani, M., Dojan, C., Ziaee, M., and Radosevich, S., “Additive Manufacturing of Carbon Fiber-Reinforced Thermoset Composites via In-Situ Thermal Curing,” 2023.

[9] Cornfield, J., “Did Extended Tax Break Get Boeing to Build 777X Here?,” Seattle Weekly, Jul 18 2019. https://www.seattleweekly.com/news/did-extended-tax-break-get-boeing-to-build-777x-in-everett

[10] Ziaee, M., Johnson, J. W., and Yourdkhani, M., “3D Printing of Short-Carbon-Fiber-Reinforced Thermoset Polymer Composites via Frontal Polymerization,” *ACS Applied Materials & Interfaces*, Vol. 14, No. 14, 2022, pp. 16694–16702.

[11] Robertson, I. D., Yourdkhani, M., Centellas, P. J., Aw, J. E., Ivanoff, D. G., Goli, E., Lloyd, E. M., Dean, L. M., Sottos, N. R., and Geubelle, P. H., “Rapid Energy-Efficient Manufacturing of Polymers and Composites via Frontal Polymerization,” *Nature*, Vol. 557, No. 7704, 2018, pp. 223–227.

[12] Aw, J. E., Zhang, X., Nelson, A. Z., Dean, L. M., Yourdkhani, M., Ewoldt, R. H., Geubelle, P. H., and Sottos, N. R., “Self-Regulative Direct Ink Writing of Frontally Polymerizing Thermoset Polymers,” *Advanced Materials Technologies*, Vol. 7, No. 9, 2022, p. 2200230.

[13] Ziaee, M., Naseri, I., Johnson, J. W., Franklin, K. A., and Yourdkhani, M., “Frontal Polymerization and Three-Dimensional Printing of Thermoset Polymers with Tunable

Thermomechanical Properties," *ACS Applied Polymer Materials*, Vol. 5, No. 3, 2023, pp. 1715–1724.

[14] Chen, Z., Ziaee, M., Yourdkhani, M., and Zhang, X., "Multiphysics Modeling of Frontal Polymerization-Assisted Layer-by-Layer Additive Manufacturing of Thermoset Polymer Components," *Additive Manufacturing*, Vol. 59, 2022, p. 103182.

[15] NASERI, I., MASOUMIPOUR, A., and YOURDKHANI, M., "Rapid Manufacture of Thin Composites via Infrared-Assisted Frontal Polymerization," presented at the PROCEEDINGS OF THE AMERICAN SOCIETY FOR COMPOSITES-THIRTY-EIGHTH TECHNICAL CONFERENCE, 2023.

[16] Aw, J. E., "Simultaneous Three-Dimensional Printing and Frontal Polymerization of Dicyclopentadiene Resin," 2019.

[17] ASTM Committee F42 on Additive Manufacturing Technologies and ASTM Committee F42 on Additive Manufacturing Technologies. Subcommittee F42. 91 on Terminology, "Standard Terminology for Additive Manufacturing Technologies," Astm International, 2012.

[18] Lewis, J. A., "Direct Ink Writing of 3D Functional Materials," *Advanced Functional Materials*, Vol. 16, No. 17, 2006, pp. 2193–2204.

[19] Gibson, I., Rosen, D. W., Stucker, B., Khorasani, M., Rosen, D., Stucker, B., and Khorasani, M., "Additive Manufacturing Technologies," Springer, 2021.

[20] Guo, Z., Fei, F., Song, X., and Zhou, C., “Analytical Study and Experimental Verification of Shear-Thinning Ink Flow in Direct Ink Writing Process,” *Journal of manufacturing science and engineering*, Vol. 145, No. 7, 2023, p. 071001.

[21] Chirico Scheele, S., Hartmann, C., Siegrist, M., Binks, M., and Egan, P. F., “Consumer Assessment of 3D-Printed Food Shape, Taste, and Fidelity Using Chocolate and Marzipan Materials,” *3D printing and additive manufacturing*, 2021.

[22] Zhang, X., Li, M., Lim, J. H., Weng, Y., Tay, Y. W. D., Pham, H., and Pham, Q.-C., “Large-Scale 3D Printing by a Team of Mobile Robots,” *Automation in Construction*, Vol. 95, 2018, pp. 98–106.

[23] Sustarevas, J., Kanoulas, D., and Julier, S., “Autonomous Mobile 3D Printing of Large-Scale Trajectories,” 2022.

[24] Sauter, A., “TechBot: A Multimaterial Mobile 3D Printing Platform,” 2019.

[25] Xu, X., Wang, Z., and Feng, C., “Projector-Guided Non-Holonomic Mobile 3D Printing,” presented at the 2021 IEEE International Conference on Robotics and Automation (ICRA), 2021.

[26] Elagandula, S., Poudel, L., Zhou, W., and Sha, Z., “Enabling Multi-Robot Cooperative Additive Manufacturing: Centralized vs. Decentralized Approaches,” In *International Design Engineering Technical Conferences and Computers and Information in Engineering Conference*, Vol. 85376, 2021, pp. V002T02A042.

[27] Poudel, L., Blair, C., McPherson, J., Sha, Z., and Zhou, W., “A Heuristic Scaling Strategy for Multi-Robot Cooperative Three-Dimensional Printing,” *Journal of Computing and Information Science in Engineering*, Vol. 20, No. 4, 2020, p. 041002.

[28] Salih, J. E. M., Rizon, M., Yaacob, S., Adom, A. H., and Mamat, M. R., “Designing Omni-Directional Mobile Robot with Mecanum Wheel [J,” presented at the American Journal of Applied Science s, 2006.

[29] Marques, L. G., Williams, R. A., and Zhou, W., “A Mobile 3D Printer for Cooperative 3D Printing,” presented at the 2017 International Solid Freeform Fabrication Symposium, 2017.

[30] Kayser, M., Cai, L., Falcone, S., Bader, C., Inglessis, N., Darweesh, B., and Oxman, N., “Design of a Multi-Agent, Fiber Composite Digital Fabrication System,” *Science Robotics*, Vol. 3, No. 22, 2018, p. eaau5630.

[31] Zhang, K., Chermprayong, P., Xiao, F., Tzoumanikas, D., Dams, B., Kay, S., Kocer, B. B., Burns, A., Orr, L., and Choi, C., “Aerial Additive Manufacturing with Multiple Autonomous Robots,” *Nature*, Vol. 609, No. 7928, 2022, pp. 709–717.

[32] Barnett, E., and Gosselin, C., “Large-Scale 3D Printing with a Cable-Suspended Robot,” *Additive Manufacturing*, Vol. 7, 2015, pp. 27–44.

[33] Sustarevas, J., Butters, D., Hammid, M., Dwyer, G., Stuart-Smith, R., and Pawar, V. M., "MAP-A Mobile Agile Printer Robot for on-Site Construction," presented at the 2018 IEEE/RSJ International Conference on Intelligent Robots and Systems (IROS), 2018.

[34] Lachmayer, L., Recker, T., and Raatz, A., "Contour Tracking Control for Mobile Robots Applicable to Large-Scale Assembly and Additive Manufacturing in Construction," *Procedia CIRP*, Vol. 106, 2022, pp. 108–113.

[35] Lakhal, O., Chettibi, T., Belarouci, A., Dherbomez, G., and Merzouki, R., "Robotized Additive Manufacturing of Funicular Architectural Geometries Based on Building Materials," *IEEE/ASME Transactions on Mechatronics*, Vol. 25, No. 5, 2020, pp. 2387–2397.

[36] Peters, S. T., "Composite Filament Winding," ASM International, 2011.

[37] Shen, F. C., "A Filament-Wound Structure Technology Overview," *Materials Chemistry and Physics*, Vol. 42, No. 2, 1995, pp. 96–100.

[38] Abdalla, F., Mutasher, S., Khalid, Y., Sapuan, S., Hamouda, A., Sahari, B., and Hamdan, M., "Design and Fabrication of Low Cost Filament Winding Machine," *Materials & design*, Vol. 28, No. 1, 2007, pp. 234–239.

[39] Quanjin, M., Rejab, M., Sahat, I., Amiruddin, M., Bachtiar, D., Siregar, J., and Ibrahim, M., "Design of Portable 3-Axis Filament Winding Machine with Inexpensive Control

System," *Journal of Mechanical Engineering and Sciences*, Vol. 12, No. 1, 2018, pp. 3479–3493.

[40] Prado, M., Dörstelmann, M., Solly, J., Menges, A., and Knippers, J., "Elytra Filament Pavilion: Robotic Filament Winding for Structural Composite Building Systems," presented at the Fabricate 2017: rethinking design and construction, 2017.

[41] Arrabiyeh, P. A., May, D., Eckrich, M., and Dlugaj, A. M., "An Overview on Current Manufacturing Technologies: Processing Continuous Rovings Impregnated with Thermoset Resin," *Polymer Composites*, Vol. 42, No. 11, 2021, pp. 5630–5655.

[42] Teng, H., "The Continuous Curing Process for Thick Filament Wound Composite Structures," University of Illinois at Urbana-Champaign, 1993.

[43] Romagna, J. H., "Neue Strategien in Der Faserwickeltechnik," 1997.

[44] Cohen, D., "Influence of Filament Winding Parameters on Composite Vessel Quality and Strength," *Composites Part A: Applied Science and Manufacturing*, Vol. 28, No. 12, 1997, pp. 1035–1047.

[45] Lee, S.-Y., and Springer, G. S., "Effects of Cure on the Mechanical Properties of Composites," *Journal of Composite Materials*, Vol. 22, No. 1, 1988, pp. 15–29.

[46] Mazumdar, S., and Hoa, S., "Analytical Models for Low Cost Manufacturing of Composite Components by Filament Winding, Part I: Direct Kinematics," *Journal of composite materials*, Vol. 29, No. 11, 1995, pp. 1515–1541.

[47] Zhao, L., Mantell, S. C., Cohen, D., and McPeak, R., "Finite Element Modeling of the Filament Winding Process," *Composite Structures*, Vol. 52, Nos. 3–4, 2001, pp. 499–510.

[48] Andrianov, A., Tomita, E. K., Veras, C. A. G., and Telles, B., "A Low-Cost Filament Winding Technology for University Laboratories and Startups," *Polymers*, Vol. 14, No. 5, 2022, p. 1066.

[49] Abliz, D., Duan, Y., Steuernagel, L., Xie, L., Li, D., and Ziegmann, G., "Curing Methods for Advanced Polymer Composites-a Review," *Polymers and Polymer Composites*, Vol. 21, No. 6, 2013, pp. 341–348.

[50] Burwasser, J. T., and Springer, G. S., "Electrothermal Curing of Filament Wound Composite Cylinders," *Journal of composite materials*, Vol. 22, No. 1, 1988, pp. 81–100.

[51] Kim, C., Teng, H., Tucker, C. L., and White, S. R., "The Continuous Cuing Process for Thermoset Polymer Composites. Part 1: Modeling and Demonstration," *Journal of Composite materials*, Vol. 29, No. 9, 1995, pp. 1222–1253.

[52] Nakouzi, S., Pancrace, J., Schmidt, F., Le Maoult, Y., and Berthet, F., "Simulations of an Infrared Composite Curing Process," *Advanced Engineering Materials*, Vol. 13, No. 7, 2011, pp. 604–608.

[53] "High Torque Hybrid Stepping Motor Specifications," Changzhou Songyang Machinery & Electronics New Technic Institute, Jun 29 2010.

[54] Sonawane, N., "An Experimental Method to Calculate Coefficient of Friction in Mecanum Wheel Rollers and Cost Analysis Using DFMA Techniques," 2015.

[55] "Low Power 650 Nm Laser," Banggood, Feb 08 2024. https://usa.banggood.com/Focusable-200-250mW-650nm-Laser-Module-Red-Dot-Laser-Generator-Diode-Replacement-Mini-DIY-Engraver-p-955966.html?imageAb=2&utm_design=41&utm_source=emarsys&utm_medium=Shipoutinform171129&utm_campaign=trigger-logistics&utm_content=Winna&sc_src=email_2671705&sc_eh=f1bb4a14d307c1121&sc_llid=12369604&sc_lid=104858042&sc_uid=8aduMjGyps&akmClientCountry=America&a=1665775374.6123&akmClientCountry=America&cur_warehouse=CN

[56] "Asbury Store," Asbury Carbons. https://www.asburystore.com/SearchResults.asp?Cat=1835

[57] Kondo, H., "Prusa I3 MK3S+ Build Volume: How Big Is It Really?," All 3DP, Aug 12 2023. https://all3dp.com/2/prusa-i3-mk3s-build-volume-how-big-is-it-actually/

[58] Goli, E., Parikh, N., Yourdkhani, M., Hibbard, N., Moore, J., Sottos, N., and Geubelle, P., "Frontal Polymerization of Unidirectional Carbon-Fiber-Reinforced Composites," *Composites Part A: Applied Science and Manufacturing*, Vol. 130, 2020, p. 105689.

[59] El Messiry, M., “Theoretical Analysis of Natural Fiber Volume Fraction of Reinforced Composites,” *Alexandria Engineering Journal*, Vol. 52, No. 3, 2013, pp. 301–306.

[60] “Materia Proxima HPR 2124 Polydicyclopentadiene Thermoset Resin,” MatWeb. https://www.matweb.com/search/datasheet.aspx?matguid=08524773cd02411d99ac9a079699b436&ckck=1

[61] “Continuous Tow,” Zoltek. https://zoltek.com/products/px35/continuous-tow/

[62] Mertiny, P., and Ellyin, F., “Influence of the Filament Winding Tension on Physical and Mechanical Properties of Reinforced Composites,” *Composites Part A: Applied Science and Manufacturing*, Vol. 33, No. 12, 2002, pp. 1615–1622.

APPENDICES

Appendix A: Mobile Printing Ink Formulations by Experiment

This appendix contains ink formulations for each set of experiments for clarity unless otherwise specified within the text. The experiments are organized by section number.

Table A 1 The ink formulation used in experiments in section 2.2.3

Ink Formulation	
Component	*wt%*
Peanut butter	100

Table A 2 The ink formulation used in experiments in section 2.3.3.

Ink Formulation	
Component	*wt%*
Peanut butter	99.5
VXC 72R carbon black	0.5

Table A 3 The ink formulation used in experiments in section 2.4.3.

Ink Formulation	
Component	*wt%*
Materia Proxima® HPR 2102 polydicyclopentadiene (pDCPD) resin	
Grubbs second generation catalyst (GC2)	89.1
Phenyl cyclohexane (PCH) solvent	
Tributyl phosphite (TBP) inhibitor	
TS-530 fumed silica (FS)	10.4
Carbon black (CB)	0.4

Table A 4 The ink formulation used in experiments in section 2.6.2

Ink Formulation	
Component	*wt%*
Materia Proxima® HPR 2102 polydicyclopentadiene (pDCPD) resin	81.4
Grubbs second generation catalyst (GC2)	
Phenyl cyclohexane (PCH) solvent	
Tributyl phosphite (TBP) inhibitor	
Cabot TS-530 fumed silica (FS)	11.1
Cabot VXC 72R carbon black (CB)	0.4
Zoltek PX35 milled fiber (MF)	7.1